JOURNAL OF

MECHANICAL ENGINEERING

An International Journal

Vol 13 (2)	December 2016	ISSN 1823-5514

Journal of Mechanical Engineering *Vol 13(2), 1-15, 2016*

Numerical Investigation of Thermal Losses from Air Filled Annulus of a Parabolic Trough Solar Collector

Alhassan Salami Tijani
Muhammad Jaafar Bin Jamarei
Faculty of Mechanical Engineering
Universiti Teknologi MARA, Shah Alam
Selangor, Darul Ehsan Malaysia

ABSTRACT

Solar energy has the potential to meet the growing need for global energy consumption. In recent times there is large number of solar energy systems developed, one of such widely used technology is parabolic trough collector (PTC). The PTC technology is one of the successful technologies because it is the most mature and one of the least expensive. PTC receivers with air filled annuli are used mainly for high temperature applications such as food processing industry. This is due to the fact that they are less costly but on the other hand they have high heat loss as compared to vacuum receivers. One of the techniques that can be adopted in order to enhance the thermal performance of the PTC has been discussed in this work. An insulation fiberglass with high heat resistant was inserted into the portion of the receiver annulus that does not receive concentrated sunlight. This study focuses on the calculation of conduction and convection heat losses of the half insulated annulus part only. The performance of the proposed concept was then compared to conventional receiver with air filled annulus. The effect of wind speed and mass flow rate of the working fluid was also considered. The reason for using mass flow rate and wind speed as manipulated variable is because both parameters affect the thermal loss of the system. The results shown that the heat loss from the half insulated is smaller compared to the heat loss from air annulus receiver by 70% depending on the wind speed of the location. Therefore, the proposed receiver is expected to be most suitable replacement for receivers with air annulus.

Keywords: *Solar, Parabolic Trough Collector, Heat Loss, Heat Transfer*

ISSN 1823- 5514

Received for review: 2015-02-03
Accepted for publication: 2016-10-10
Published: 2016-12-19

Introduction

Sustainable renewable energy is derived from natural resources that are continously being replenished, one of such example is the solar energy that is derived directly from the sun [1]. In recent times solar thermal energy has been predicted to be clean energy of tomorrow. Solar energy has been the main agenda of energy development in many developed countries such as Germany and USA and it is a potential source of energy for developing countries such as Malaysia. It is however expected that, through the application of renewable energy technologies, the global renewable energy consumption wouls reach 318 exajoules by the year 2050 [1]. One of the advantages of solar energy is that, it is clean and can be supplied without any environment pollution [2,3]. Fossil energy also could be saved if every house uses more solar energy as their primary heat sources [3]. Parabolic trough collector, solar power tower and parabolic dish collector are three basic principal types of solar energy collector that are available for high temperature application [1]. Parabolic trough collector (PTC) technology is a type of concentrated solar power (CSP) conversion [4]. During the past decades, CSP technology has been important option for harnessing solar energy [5]. PTC are the most mature solar energy and able to generate heat at temperatures up to 400 °C [7,8].

There are several successful commercial PTC for CSP plants that have been tested in a temperature range of 300-400 °C [8]. The use of PTC in the electric generation system has been associated with numerous losses including optical, thermal and geometry losses [9]. The PTC collectors available today uses expensive receivers due to the effort put in place to maintain vacuum in their annuli. Vacuum annuli has the tendency to reduce convection losses. Basically, the receiver of a parabolic trough collector consists of outer transparent enclosure, typically made of glass and inner absorber tube, made of steel (see Figure 1 for details). Al-Ansary and Zeitoun [10] proposed a technique by fitting a heat resistant thermal insulation material into the portion of the receiver annulus that does not receive concentrated sunlight. The result shows that heat loss from the proposed receiver can be smaller than that from a receiver with an air filled annulus as much as 25% when fiberglass is used. In recent study Tijani and Roslan [9] presented a detailed model of heat loss in parabolic trough receivers. Hachicha et al. [11] presented a numerical study based on Large-Eddy Simulations (LES) models for the simulation of the fluid flow and heat transfer around a parabolic trough solar collector and its receiver tube is performed. The aim of this manuscript is to numerically analyse the thermal losses associated with PTC. The effect of changes in environmental conditions (such as wind speed) on heat loss was evaluated. This research was focused on the heat losses that occur at the insulation part which doesn’t receive concentrated sunlight. The thermal losses models were simulated using ANSYS fluent solver.

Description of Parabolic Trough Collector (PTC) Module

Parabolic Trough Collectors (PTCs) are linear focus concentrating solar devices suitable for working in high temperature application of 150-400 °C temperature range. A PTC is made up of a parabolic trough shaped mirror that reflects direct solar radiation, concentrating it onto a receiver tube located in onto a receiver tube located in the focal line of the parabola [11]. The energy from sunlight which falls on the surface of the mirror parallel to its plane of symmetry is focused along the focal line. The concentrated radiation heats the fluid that circulates through the receiver absorber tube, thus transforming the solar radiation into thermal energy in the form of the sensible heat of the fluid.

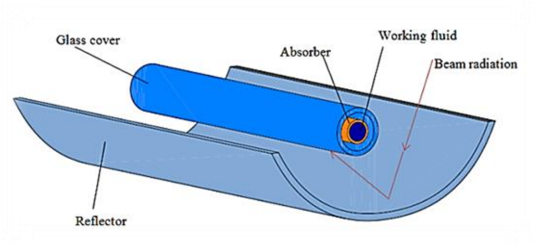

Figure 1: Schematic representation of a parabolic trough collector

Table 1: LS-2 PTC geometry [9]

Item	**Value**
Collector aperture area	39 m^2
Collector aperture width	5 m
Collector aperture length	7.8 m
Glass envelope outer diameter	0.115 m
Glass envelope inner diameter	0.109 m
Absorber tube outer diameter	0.07 m
Absorber tube inner diameter	0.065 m

The heat transfer fluid flows at the receiver of a parabolic trough collector consist of an inner absorber tube made of steel and an outer transparent enclosure made of glass. The objective of using the transparent enclosure is to minimize heat loss by convection to the surrounding due to the interaction between the hot absorber tube surface and the ambient air. The outer glass tube is attached to the steel pipe by means of flexible metal differential expansion joints which compensate for the different thermal expansion of glass and steel when the receiver tube is working at nominal temperature. A schematic representation of a single parabolic trough collector module and its technical specifications are given in Figure 1 and Table 1 respectively.

Losses in Parabolic trough collector

There are three main types of losses associated with parabolic trough collectors [11]:

a) Optical losses
b) Thermal losses from the absorber pipe to the ambient
c) Geometrical losses

For this project, we focused on the heat losses from a half insulated air-filled annulus of the receiver of a parabolic trough collector focusing on thermal losses from the absorber pipe to the inner glass cover.

A summary of a model of the thermal losses from the collector can be developed using a combination of the collector thermal loss from radiation, conduction and convection, as listed in Figure 2.

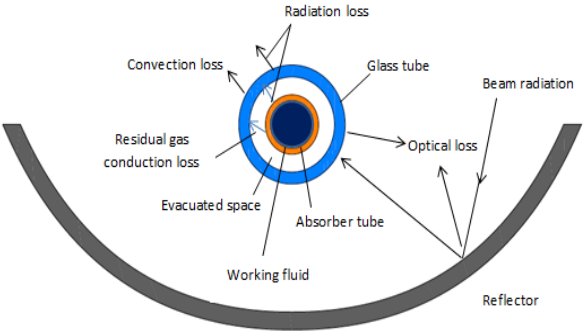

Figure 2: Modes of heat loss from an evacuated tubular absorber

1. Thermal loss from the absorber tube outer wall to the evacuated glass tube (surrounding the absorber) occurs by radiation and residual gas conduction. Due to the high vacuum in the absorber element ($10^{-4}\,mmHg$) convection is normally negligible, however it can be significant if the pressure is allowed to increase.
2. Heat loss from the absorber tube to the ambient also occurs via the vacuum bellows and supports. Heat loss from the glass cover tube occurs by radiation to the sky and by convection.

Description of Half Insulated Air Filled Annulus

The physical model of the investigated problem is illustrated schematically in Figure 3. Thermal insulation is used to fill half of the annulus while the other half is filled with air. Hot water fluid flows inside the tube, transferring heat to the surroundings. The flow is assumed to be steady and laminar flow of about 200 Reynolds number was simulated. From the heat transfer mechanism, the inner absorber tube is expected to have a higher temperature than the outer absorber tube; this is due to the convection effect on the outer surface of the absorber tube. During the same period, conduction and radiation heat transfer will take place within the half insulated annulus. A heat resistant insulating material fiberglass is chosen as the insulator. For efficiency improvement and less energy loss half insulated air filed annulus was proposed. The hypothesis is that only the half insulated air filed annulus is exposed to the direct irradiation where as the top part is insulated with fibre glass so as to resist heat loss by convection.

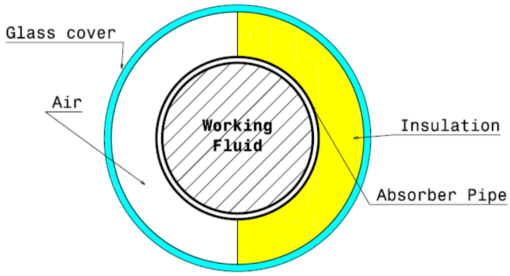

Figure 3: Half insulated-half stationary air filled annulus of PT

Thermal Analysis of Receiver

Convection Heat Transfer between the Heat Transfer Fluid (HTF) and the Receiver Pipe

Based on the Newton's law, the convection heat transfer from the inner surface of the receiver pipe to the HTF is given by $hA(T_s\text{-}T_\infty)$ [12].

$$q_{f-pi,conv} = h_f \pi D_{pi} \, (T_{pi}\text{-}T_f) \tag{1}$$

Where,

h_f= HTF convection heat transfer coefficient $(W/m^2 - °C)$

D_{pi}= Diameter of inner pipe (m)
T_{pi}= Pipe inner temperature (°C)
T_f= Fluid temperature (°C)

Conduction Heat Transfer through the Receiver Pipe Wall

The Fourier's Law of conduction through hollow cylinder is used to determined conduction heat transfer through the receiver pipe. The equation given [13] :

$$q_{pi-po,cond} = \frac{2\pi k_{pipe}(T_{pi}-T_{po})}{\ln(\frac{D_{po}}{D_{pi}})} \quad (2)$$

Where,

k = Thermal conductivity of the pipe W/m-K.

In the equation thermal conductivity is constant and depends on the receiver pipe material type. If steel is used, the thermal conductivity is 16.27 W/m-K.

Convection Heat Transfer from Receiver to Glass Envelope

Air in annulus: The convection heat transfer equation between the receiver pipe and glass envelope when there is air in annulus are [14]:

$$q_{po-gi,conv} = \frac{2\pi k_{eff}}{\ln(\frac{D_{gi}}{D_{po}})}(T_{gi} - T_{po}) \quad (3)$$

Where,

k_{eff}= effective thermal conductivity (W/m-K)

Radiation Heat Transfer

The radiation heat transfer equation between the receiver pipe and glass envelope ($q_{po-gi,rad}$) are [6] :

$$q_{po-gi,rad} = \frac{\sigma\pi D_{po}\left(T_{po}^4 - T_{gi}^4\right)}{\left(\frac{1}{\varepsilon_{po}}+\left(\frac{\left(1-\varepsilon_{gi}\right)D_{po}}{\varepsilon_{gi}D_{gi}}\right)\right)} \quad (4)$$

Where,

ε_{po}= Emissivity for pipe outer
ε_{gi}= Emissivity for pipe inner

Fluid Dynamics

The partial differential equations governing the fluid flow and heat transfer in the enclosure include the continuity, the Navier-Stokes and the energy equations. The assumptions that need to be considered are the flow is steady and laminar, long enclosure, flow in the gap is two dimensional and the fluid is assumed to be Newtonian. The continuity equation may be written as shown by Al-Ansary et. al [10]:

$$\frac{\partial u}{\partial x} + \frac{\partial v}{\partial y} + \frac{\partial w}{\partial z} = 0 \tag{5}$$

The momentum equations in x, y and z directions can be written as:

$$\rho u\frac{\partial u}{\partial x} + \rho v\frac{\partial u}{\partial y} + \rho\frac{\partial w}{\partial z} = -\rho g_x - \frac{\partial P}{\partial x} + \mu\left[\frac{\partial^2 u}{\partial x^2} + \frac{\partial^2 u}{\partial y^2} + \frac{\partial^2 u}{\partial z^2}\right] \tag{6}$$

$$\rho u\frac{\partial v}{\partial x} + \rho v\frac{\partial v}{\partial y} + \rho\frac{\partial w}{\partial z} = -\rho g_y - \frac{\partial P}{\partial y} + \mu\left[\frac{\partial^2 v}{\partial x^2} + \frac{\partial^2 v}{\partial y^2} + \frac{\partial^2 v}{\partial z^2}\right] \tag{7}$$

$$\rho u\frac{\partial w}{\partial x} + \rho v\frac{\partial w}{\partial y} + \rho\frac{\partial w}{\partial z} = -\rho g_z - \frac{\partial P}{\partial z} + \mu\left[\frac{\partial^2 w}{\partial x^2} + \frac{\partial^2 w}{\partial y^2} + \frac{\partial^2 w}{\partial z^2}\right] \tag{8}$$

The energy equations for the air in the gap and the insulation can be written as:

$$\rho C_p u\frac{\partial T}{\partial x} + \rho C_p v\frac{\partial T}{\partial y} + \rho C_p w\frac{\partial T}{\partial z} = k\left[\frac{\partial^2 T}{\partial x^2} + \frac{\partial^2 T}{\partial y^2} + \frac{\partial^2 T}{\partial z^2}\right] \tag{9}$$

$$\frac{\partial^2 u}{\partial x^2} + \frac{\partial^2 T}{\partial y^2} + \frac{\partial^2 T}{\partial z^2} = 0 \tag{10}$$

For natural convection, the change in density is responsible for inducing the flow. The fluid density is estimated using the ideal gas equation of state, which is provided as an input to the problem. The reference pressure is assumed equal to the standard atmospheric pressure. The properties of air are assumed temperature dependent. The boundary conditions for the current problem are:

- No slip condition along the interface between air and the inner and outer cylindrical surfaces.
- The convection coefficient at the outer surface is h_0 and the ouside ambient temperature is T_0.

- The convection coefficient at the inner surface is h_i and the inside bulk fluid temperature is T_i.

Simulation Model of the PTC

In order to design the geometry model of the PTC, CATIA software was used. The parameters of the PTC geometry are similar to LS-2 PTC (refer to Figure1 and Table 1). After the PTC has been modeled in CATIA, the model is then exported to ANSYS fluent solver for meshing. Meshing is a process of dividing or discretizing the model domain into a finite number of smaller elements. After the meshing process was completed, the domains are defined as fluid or solid according to their respective condition. Figure 4 shows isometric view of half insulated annulus. The material of half insulated annulus is made from fiber.

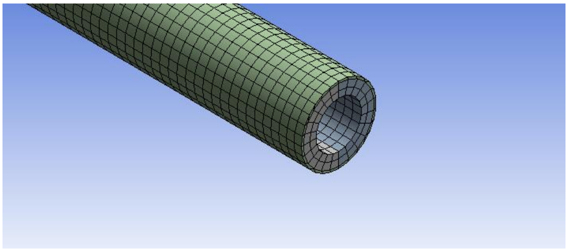

Figure 4: Isometric view of meshed half insulated annulus

Materials which make up the receiver are created or taken from FLUENT library. The thermal properties of the materials are defined as Table 2 below:

Table 2: Materials properties

Material	**Properties**			
	ρ (kg/m^3)	**C_p (J/kg-K)**	**k (W/m-K)**	**μ (kg/m-s)**
Water-liquid	998.2	4182	0.6	0.001003
Air	1.225	1006.43	0.0242	1.7894e-05
Pyrex	2225	835	1.4	
Steel	8030	502.48	16.27	
Fiberglass	48	843	0.037492	

Result and Discussion

In this study the total heat loss due to convection and radiation for air annuli was conducted. It can be observed from Table 3 that the total heat loss for the combination of convection and radiation ranges between 34.90 W/m to 75.14 W/m. The heat loss for half insulated annulus was lower compared to that fully air annulus (see Table 4).

Table 3: Total heat loss for fully air annulus

Heat loss by convection (W/m)	**Heat loss by radiation (W/m)**	**Total Heat Loss (W/m)**
18.20	16.70	34.90
26.91	17.43	44.35
33.62	17.77	51.39
39.28	17.97	57.24
44.26	18.11	62.37
48.77	18.21	66.98
52.92	18.29	71.21
56.78	18.35	75.14

Table 4: Total heat loss for a half insulated

Heat loss by conduction (W/m)	**Heat loss by radiation (W/m)**	**Σ Heat Loss (W/m)**
3.80	15.78	19.57
4.03	16.70	20.73
4.14	17.13	21.27
4.20	17.40	21.60
4.25	17.58	21.83
4.29	17.72	22.01
4.31	17.83	22.14
4.34	17.92	22.25

The generated data are represented in graphical form to assist in observation, analysis and discussion purpose. The trends and patterns resulting from the simulation are then validated with previously done research study by other researcher to ensure justification of the simulation data. Figure 7 shows the temperature distribution of half insulated annulus and fully insulted annulus. For a half insulated annulus the temperature distribution is highest (315 K) at the bottom part of the absorber tube, where as the lower part has a lower temperature distribution, this shows that much of the heat is trapped at the bottom part of the absorber and this can easily be transfered to the working fluid. The presence of insulation material reduces heat transfer to due to convection and conduction to the surrounding. When compared to the fully air annulus, it can be observed that the temperature distribution is not concentrated at the bottom part of the absorber where it is most needed, instead it is extends to the top part of the absober. This phenomenon is due to the convection heat transfer initiated by the air trapped in the annulus. This concludes that the top part of the absorber is susceptible to more heat losses due to convection to the surrounding. This explanation has been justified by the results obtain in Table 3 and Table 4. The result is also similar to that found in the literature [10].

Wind speed, m/s	**Temperature contours for half insulated annulus**	**Temperature (K)**	**Temperature contours for fully air annulus**
0.5	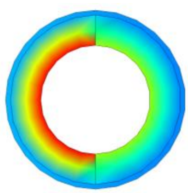	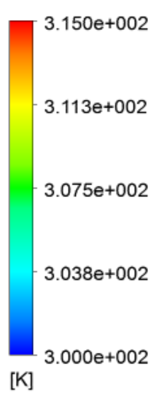	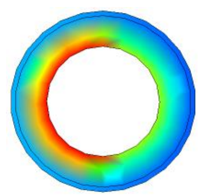
1.0	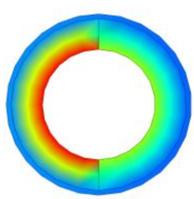		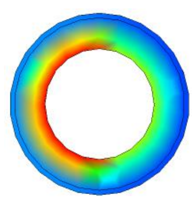
1.5	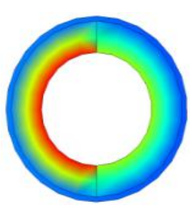		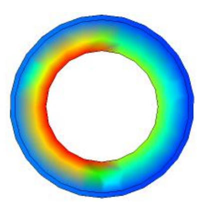

Wind speed, m/s	**Temperature contours for half insulated annulus**	**Temperature (K)**	**Temperature contours for fully air annulus**
2.0	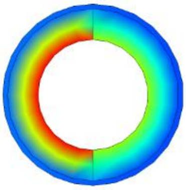		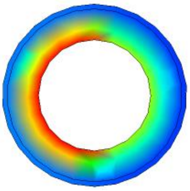
2.5	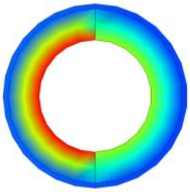		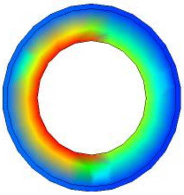
3.0	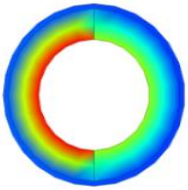		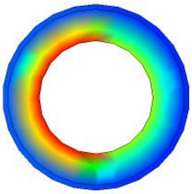
3.5	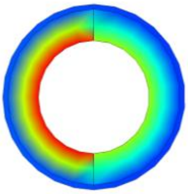		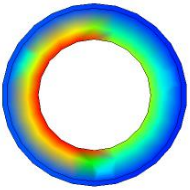
4.0	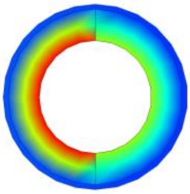		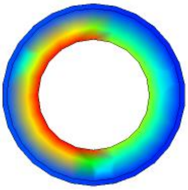

Figure 5: Isothermal zones in half insulated annulus and fully air annulus

Based on Figure 5, it can be observed that the heat loss for half insulated annulus is less compared to the transfer of heat loss for fully air annulus. With increasing of wind speed from 0.5 m/s to 4.0 m/s, the transfer of heat loss also will increase. The heat loss transfer for fully air annulus is kept increasing when the wind speed is increases, this is due to the value of convection which depends on the wind speed.

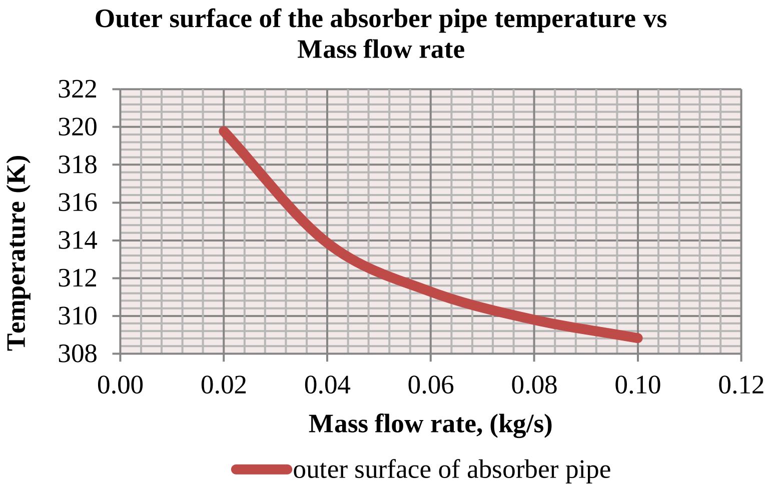

Figure 6: Effect of mass flow rate of HTF on temperature of outer surface of the absorber pipe.

It can be observed from Figure 6 that the outer surface of pipe temperature is inversely proportional to the mass flow rate of air.Iincreasing mass flow rate has resulted in an increase of outer sureface pipe temperature. It means that mass flow rate has a significant influence on the insulated material and glass envelope temperature which eventually affect the thermal losses of the system.

Figure 7 shows that the total heat loss is directly proportional to wind speed velocity for both half insulated annulus and fully air annulus. The drastic heat loss for fully air annulus was observed due to fact that the convective heat transfer coefficient is directly proportional to the value of wind speed. While for half insulated material have only experience small change in total loss because of the thermal conductivity value is constant and not affected by the value of wind speed. The highest total heat loss 170.52 W/m was observed for fully air annulus with mass flow rate of 0.02 kg/s and wind speed of 4 m/s. While the lowest total heat loss 19.57 W/m was observed for half insulated with mass flow rate 0.1 kg/s and wind speed of 0.5 m/s.

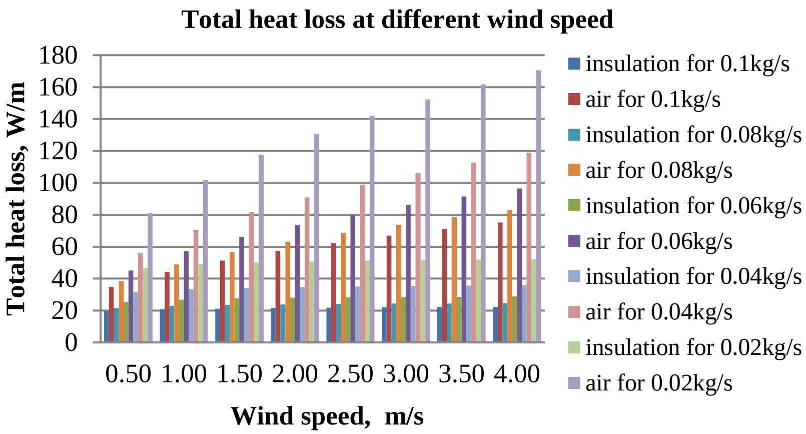

Figure 7: Effect of total heat loss at different mass flow rate and different wind speed

From Figure 8 it can be observed that the percentage of heat loss for half insulated air annulus is directly increase when wind speed also increase. The higher value of mass flow rate and wind speed the higher the percentage decrease compare to air filled annulus. The highest percentage value is 70.38 %. The highest percentage decrease value is at wind speed 4 m/s and mass flow rate 0.1 kg/s. This happen because at strong wind speed the convection heat loss at air annulus is very high. The lowest percentage is when mass flow rate 0.1 kg/s and wind speed 0.5 m/s. The lowest percentage value is 42.66 %.

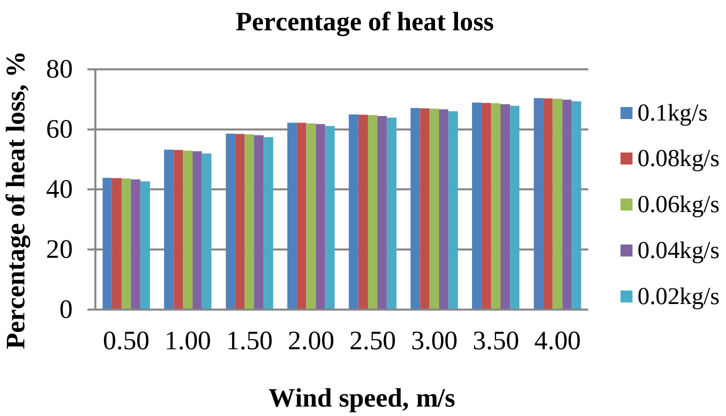

Figure 8: Percentage of heat loss for half insulated compare to fully air annulus

Conclusion

This reasearch manuscript examines the possiblity to reduce thermal losses associated with the system by means of insulation material and to evaluate the effect of wind speed on heat loss. The percentage of heat loss for half insulated annulus can achieve up to 70% depending on the mass flow rate and wind speed. The numerical simulation of the model has been developed using ANSYS FLUENT solver which give the resulting temperature of outward glass envelope as compared to the temperature of the pipe absorber. The thermal loss has been numerically calculated from the resulting glass envelope temperature and pipe absorber. The model was stimulated with different mass flow rate and wind speed to observe the different thermal heat loss behavior.

References

[1] S. A. Kalogirou, "Solar thermal collectors and applications," *Progress in Energy and Combustion Science*, vol. 30, pp. 231-295, 2004.

[2] J. Liu, F. Wang, L. Zhang, X. Fang, and Z. Zhang, “Thermodynamic properties and thermal stability of ionic liquid-based nanofluids containing graphene as advanced heat transfer fluids for medium-to-high-temperature applications,” Renew. Energy, vol. 63, pp. 519–523, Mar. 2014.

[3] S. Hirasawa, R. Tsubota, T. Kawanami, and K. Shirai, “Reduction of heat loss from solar thermal collector by diminishing natural convection

with high-porosity porous medium," Sol. Energy, vol. 97, pp. 305–313, Nov. 2013.

[4] N. B. Desai and S. Bandyopadhyay, "Optimization of concentrating solar thermal power plant based on parabolic trough collector," J. Clean. Prod., vol. 89, pp. 262–271, Nov. 2014.

[5] C. Sharma, A. K. Sharma, S. C. Mullick, and T. C. Kandpal, "Assessment of solar thermal power generation potential in India," Renew. Sustain. Energy Rev., vol. 42, pp. 902–912, Feb. 2015.

[6] S. A. Kalogirou, "A detailed thermal model of a parabolic trough collector receiver," Energy, vol. 48, no. 1, pp. 298–306, Dec. 2012.

[7] M. Natarajan, Y. R. Sekhar, T. Srinivas, and P. Gupta, "Numerical Simulation of heat transfer characteristics in the absober tube of parabolic trough collector with internal flow obstruction ," vol. 9, no. 5, pp. 674–681, 2014.

[8] İ. H. Yılmaz and M. S. Söylemez, "Thermo-mathematical modeling of parabolic trough collector," Energy Convers. Manag., vol. 88, pp. 768–784, Dec. 2014.

[9] A. S. Tijani and A. M. S. Bin Roslan, "Simulation Analysis of Thermal Losses of Parabolic trough Solar Collector in Malaysia Using Computational Fluid Dynamics," Procedia Technol., vol. 15, pp. 842–849, 2014.

[10] H. Al-Ansary and O. Zeitoun, "Numerical study of conduction and convection heat losses from a half-insulated air-filled annulus of the receiver of a parabolic trough collector," Sol. Energy, vol. 85, no. 11, pp. 3036–3045, Nov. 2011.

[11] A.A. Hachicha, I. Rodr´ıguez, A. Oliva, Wind speed effect on the flow field and heat transfer around a parabolic trough solar collector, Applied Energy 2014;110:316–37.

[12] Gnielnski V., "New equation for heat and mass transfer in turbulent pipe and channel flow," Int. Chem. Eng., no. 562(2):359–63, 1976.

[13] Cengel YA, Heat Transfer and Mass Transfer, 3rd Edition. McGraw Hill Book Company, 2006.

[14] Marshal N., "Gas Encyclopedia." Elsevier, 1976.

Flow Visualization in a Ranque-Hilsch Vortex Tube

Yusman Istihat[*], *Muhamad Hujwiri Sabri*
Faculty of Engineering, Universiti Selangor (UNISEL)
45600 Bestari Jaya, Selangor Darul Ehsan, Malaysia
[*]*yusman@unisel.edu.my*

Wirachman Wisnoe[*], *Khairil Muhaimin Abd Rahman*
Faculty of Mechanical Engineering, Universiti Teknologi MARA (UiTM)
40450 Shah Alam, Selangor Darul Ehsan, Malaysia
[*]*wira_wisnoe@salam.uitm.edu.my*

ABSTRACT

This paper presents the results of flow visualization in a Ranque-Hilsch vortex tube (RHVT). The RHVT has been newly designed and locally fabricated. Dimensional analysis and similarity was carried out by taking comparison between real model (Blue Model) of RHVT and prototype (Clear Prototype) using acrylic. The research objective is to visualize flow patterns inside the tube and water is chosen as the flowing fluid. Several methods of visualization were adapted in this exercise especially for observing the particles movement throughout the process. Still pictures and videos were recorded and formation of vortex was studied. It is observed that the flow pattern of circulation was presented and visible. The existence of two swirling flows can be seen and documented. The frames of pictures show a flow pattern of forward and backward flows obtained from the vortex tube.

Keywords: *Flow Visualization, Flow Pattern, Ranque-Hilsch Effect, Dimensional Analysis, Frame Frequency.*

Nomenclature

Lpm	Liter per minute	CFD	Computational Fluid Dynamics
d	diameter	h	height of conical valve
ρ	density	r	radius
F_ω	centrifugal force	D_o	outer diameter
g	gravitational acceleration	D_i	inner diameter
μ	fluid viscosity	fps	frame per seconds

ISSN 1823- 5514

Received for review: 2015-12-07
Accepted for publication: 2016-11-10
Published: 2016-12-19

Q	volume flow rate	ABS	Acrylonitrile Butadiene Styrene
v	velocity	t	thickness
ω	vortex angular velocity	V	volume
f	swirling frequency	L	tube length

Introduction

The vortex tube is a thermos-fluidic device which can produce different pressures and temperatures at each exit. The device was invented by Georges J. Ranque in 1933 and its capability was improved by Hilsch in 1947. Most researchers are interested to study the energy/temperature separation inside the tube. Numerical and CFD approach was often used in explaining the phenomena. Till today, the physical behaviour of the flow is not fully covered due to uniqueness of experimental results. Regarding the radial static temperature gradient, Scheller & Brown [1] found that it is inversely proportional to the vortex tube's radius but some researchers found in different manner. Figure 1 illustrates the flow pattern inside the vortex tube.

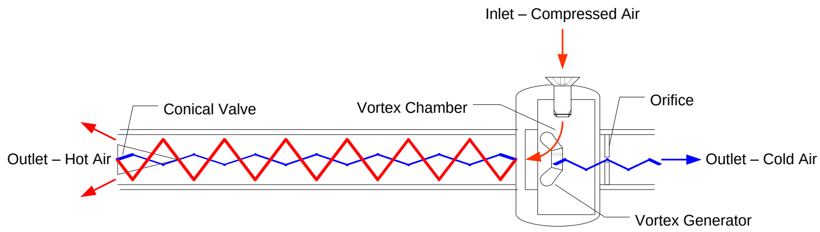

Figure 1: Flow pattern in vortex tube

In the study of Ranque-Hilsch effect, flow pattern knowledge is part of paramount importance especially when dealing with unique phenomena. Flow pattern in Computational Fluid Dynamics (CFD) will give exact colour scheme visualisations which interprets Ranque-Hilsh effect in acceptable manner. Complicated flow pattern due to high swirl effect makes the interpretation more challenging and to simplify the issue, flow visualisation should be introduced. In this approach, it is significance that the flow will be projected as laminar flow in order to get basic trend of swirling in RHVT. Y. Xeu et al. [2] have contributed a research on flow visualisation to understand the flow behaviour. They revealed a multi-circulation region which is dominant in generating heat by viscous friction. Aydin and Baki [3] studied the optimum geometry for energy separation and came out with flow visualization. Meanwhile, Arbuzov et al. [4] used the method of Hilbert chromatic filtering and obtain the formation of vortex flow in double helix profile.

The main objective of this paper is to present flow visualization of RHVT using water. The ultimate goal is to obtain flow pattern observation during short time interval and study the formation of vortex generation in Ranque-Hilsch vortex tube.

The principal work of RHVT was initiated by compressed air that flows through the inlet and passes out through the hot and cold exits. Swirling generator located at the inlet chamber stimulate a swirling flow inside the tube. This swirling flow distributes temperatures along the tube [5]. The compressed air is injected tangentially to the inlet and causes a rotational speed of air near the interior wall. The moving air at this region is released to the hot exit and produce hot air. Conical valve transmits the moving air in the central part to opposite direction and pass through the orifice; expansion occurred and the moving air is discharged as cold air to the cold exit.

The performance of RHVT is influenced by many factors such as supply pressure, conical valve shape, swirl generator, etc. Variation on these parameters will change the mass cold fraction that affects the isentropic efficiency of RHVT [6]. M. Kurosaka [7] used uniflow arrangement of RHVT in acoustic streaming study. He demonstrated through analysis and experiment that the acoustic streaming affects the temperature separation. Y. Xue et al. [8] studied the flow structure in a counter flow vortex tube by measuring velocity distribution and presented velocity fluctuation in time domain. Chang-Soo and Chang-Hyun [9] observed that the vortex tube has two distinct kinds of frequency: low and high frequency periodic fluctuations. Y. Istihat and W. Wisnoe [10] confirmed the presence of two bands of frequencies in the vortex tube. The analysis was done using Wavelet transform. Hazwan and Katanoda [11] studied the flow visualization of flow pattern discharged at the cold exist of RHVT. They found that a negative (suction) and positive pressure region exist at a certain pressure and cold fraction area, and observed a reverse flow in the negative pressure region.

Experimental Apparatus and Setup

To explain the Ranque-Hilsch effect in a vortex tube, a good understanding of the flow behaviour inside the tube is required. Flow visualization techniques have been used to investigate the flow field within the vortex tube, such as dyes and smoke injection. With the injection of dyes or smoke, all subsequent investigations concentrated on tracking the flow trail on the wall near the ends of the tube, and used a clear tube as the main part of the device for tracking the visual elements.

Figure 2 below shows the drawing of RHVT. Main parts of body were made from acrylic and conical valve was made from aluminium. Standard size of acrylics were used meanwhile a conical shape was manufactured using lathe machine.

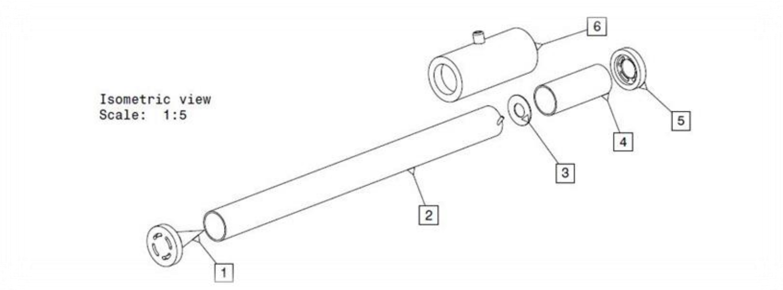

Figure 2: Exploded view of Clear Prototype RHVT

Table 1: Detailed dimension for Clear Prototype

No.	Parts	Quantity	Dimensions (mm)
1	Conical Valve	1	h = 110.12, r =18.79
2	Long Tube	1	D_o = 60, D_i = 54, L = 750
3	Orifice	1	D_o = 60, D_i = 27, t = 17
4	Cold End Tube	1	D_o = 60, D_i = 54, L = 150
5	Web Cap (Outlet)	2	D_o = 54, 4 holes
6	Vortex Chamber	1	D_o = 90, D_i = 84

Table 1 above illustrates the detail dimension of Clear Prototype in this study. The drawing was scaled from a real model (Blue Model) of RHVT which is tested for the Ranque-Hilsch effect.

Dimensional Analysis and Similarity

There are three necessary conditions for completing similarity between a model (Blue Model) and prototype (Clear Prototype). First condition is geometric similarity, the model must be the same shape as the prototype, but may be scaled by some constant scale factor. Second condition is kinematic similarity, which means that the velocity at any point in the model flow must be proportional by a constant scale factor to the velocity at the corresponding point in the prototype flow. The velocity at corresponding point has to be scale in magnitude and must point in the same direction. The third and most restrictive similarity condition is that of dynamic similarity. It is achieved when all the forces in the model flow, scale by a constant factor to corresponding forces in the prototype flow.

List of parameters influencing the angular velocity (ω) of vortex in the vortex tube.

a. Inlet diameter (d)
b. Fluid density ($\rho = m/V$)
c. Centrifugal force (F_ω)
d. Gravitational acceleration (g)
e. Fluid viscosity (μ)
f. Volume flow rate ($Q = Av$)
g. Velocity (v)
h. Vortex angular velocity (ω)
i. Swirling frequency (f)

Using Buckingham Π theorem:-

$$\emptyset(\Pi_1, \Pi_2, \Pi_{3\ldots}, \Pi_{n-m}) = 0$$

n = 9 (number of variables)
m = 3 (3 fundamental dimensions: M, L, T only. The effect of temperature θ is not in this study)
n-m = 6 (limit the parameter that are both controllable and measureable in the lab)

Statement of vortex angular velocity can be seen through equation (1) to (12)

$$\emptyset(\Pi_1, \Pi_2, \Pi_3, \Pi_4, \Pi_5, \Pi_6) = 0 \tag{1}$$

Take ρ, v and d as a primary variable. The Π terms are;

$$\Pi_1 = \rho^{a_1} v^{b_1} d^{c_1}, F_\omega \tag{2}$$
$$\Pi_2 = \rho^{a_2} v^{b_2} d^{c_2}, g \tag{3}$$
$$\Pi_3 = \rho^{a_3} v^{b_3} d^{c_3}, \mu \tag{4}$$
$$\Pi_4 = \rho^{a_4} v^{b_4} d^{c_4}, Q \tag{5}$$
$$\Pi_5 = \rho^{a_5} v^{b_5} d^{c_5}, \omega \tag{6}$$
$$\Pi_6 = \rho^{a_6} v^{b_6} d^{c_6}, f \tag{7}$$

Example of analysis for

$$\Pi_1 = \rho^{a_1} v^{b_1} d^{c_1}, F_\omega$$

a. MLT system

$$[MLT]^0 = [ML^{-3}]^{a_1} [LT^{-1}]^{b_1} [L]^{c_1} [MLT^{-2}]$$

b. Homogeneity left and right

$$\begin{aligned} &M \to 0 = a_1 + 1 && \to a_1 = -1 \\ &L \to 0 = -3a_1 + b_1 + c_1 + 1 && \to c_1 = -4 - b_1 \\ &T \to 0 = -b_1 - 2 && \to b_1 = -2, so\ c_1 = -2 \end{aligned}$$

c. Final form of Π_1

$$(\Pi_1 = \rho^{-1} v^{-2} d^{-2} F_P)$$

$$\left(\Pi_1 = \frac{F_\omega}{\rho v^2 d^2}\right)$$

With the same approach, all equations can be written as

$$\begin{aligned} \Pi_1 &= \frac{F_\omega}{\rho v^2 d^2} \\ \Pi_2 &= \frac{gd}{v^2} \to Richardson\ Number, Ri \\ \Pi_3 &= \frac{\mu}{\rho v d} \to 1/Reynolds\ Number, Re \\ \Pi_4 &= \frac{Q}{v d^2} \\ \Pi_5 &= \frac{\omega d}{v} \\ \Pi_6 &= \frac{fd}{v} \to Strouhal\ Number, St \end{aligned}$$

Finally,

$$\emptyset(\Pi_1, \Pi_2, \Pi_3, \Pi_4, \Pi_5, \Pi_6) = 0$$

$$\emptyset\left(\frac{F_\omega}{\rho v^2 d^2}, \frac{gd}{v^2}, \frac{\mu}{\rho v d}, \frac{Q}{v d^2}, \frac{\omega d}{v}, \frac{fd}{v}\right) = 0 \tag{8}$$

$$\Pi_5 = \emptyset_5\left(\frac{F_\omega}{\rho v^2 d^2}, \frac{gd}{v^2}, \frac{\mu}{\rho v d}, \frac{Q}{vd^2}, \frac{fd}{v}\right) \tag{9}$$

$$\frac{\omega d}{v} = \emptyset_5\left(\frac{F_\omega}{\rho v^2 d^2}, \frac{gd}{v^2}, \frac{\mu}{\rho v d}, \frac{Q}{vd^2}, \frac{fd}{v}\right) \tag{10}$$

$$\omega = \frac{v}{d}\emptyset_5\left(\frac{F_\omega}{\rho v^2 d^2}, \frac{gd}{v^2}, \frac{\mu}{\rho v d}, \frac{Q}{vd^2}, \frac{fd}{v}\right) \tag{11}$$

The final expression for vortex angular velocity was given by

$$\omega = \frac{v}{d}\emptyset_5\left(\frac{F_\omega}{\rho v^2 d^2}, Ri, \frac{1}{Re}, \frac{Q}{vd^2}, St\right) \tag{12}$$

The vortex angular velocity (ω) is equal to some coefficient times *v/d*, where the coefficient is a function of other five dimensionless numbers consist of Richardson, Reynolds, Strouhal and other dimensional numbers.

Parameter Setting for Experiment

For parameter setting, a model of vortex tube (Blue Model) has been used to figure up similarity with the prototype (Clear Prototype). This similarity analysis will provide required velocity from Reynolds number study. All the comparison data was extracted from Blue Model experiments [12]. Figure 3 below shows the RHVT model for air which is fabricated using thermoplastic resin ABS (Acrylonitrile Butadiene Styrene) pipe. Figure 4 below shows experimental setup for Blue Model conducted at UiTM Shah Alam and Clear Prototype at UNISEL Bestari Jaya.

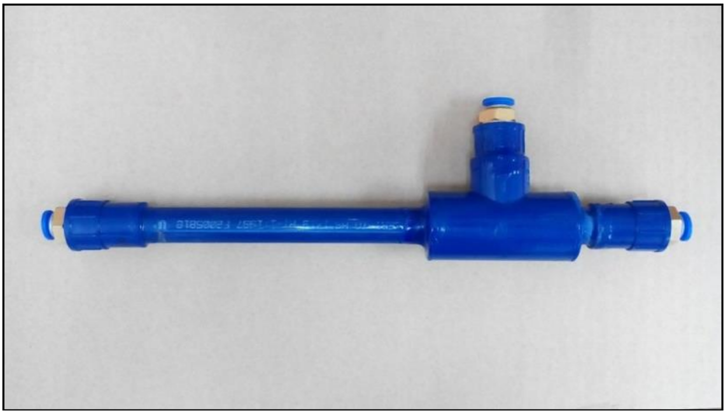

Figure 3: Fabricated Blue Model of RHVT using air as working fluid

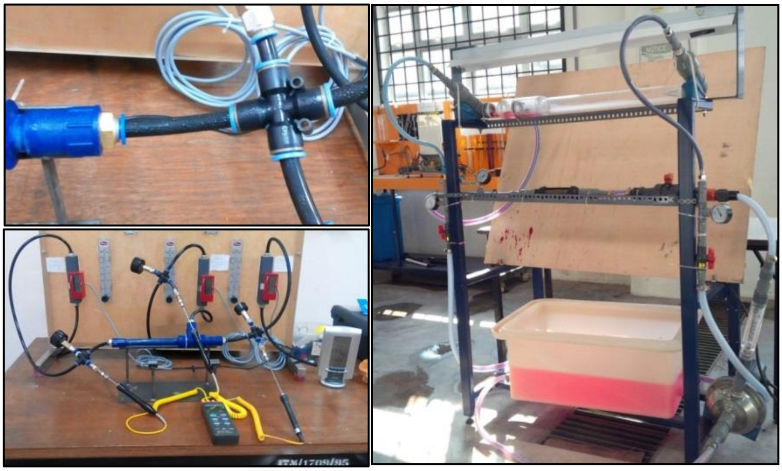

Figure 4: Experimental setup for Blue Model and Clear Prototype

From experimental data [13], velocity for Blue Model is 1157 m/s so the value was divided by two inlets, hence 578.5 m/s will be taken as the velocity value in the experiment. From this value, the dynamic similarity analysis was carried out:

$$(Re\ )_{model} = (Re\ )_{prototype} \tag{13}$$

$$\left(Re = \frac{\rho v D}{\mu}\right)_{model} = \left(Re = \frac{\rho v D}{\mu}\right)_{prototype}$$

$$\frac{(1.18667)(578.5)(1.78 \times 10^{-3})}{1.84516 \times 10^{-5}} = \frac{(1000)(v)(6 \times 10^{-3})}{0.891 \times 10^{-3}}$$

$$66{,}224.59 = \frac{(1000)(v)(6 \times 10^{-3})}{0.891 \times 10^{-3}}$$

$$v = 9.83\ m/s$$

Table 2: Input parameters for experiment

No	Blue Model	Clear Prototype	
	***v* (m/s)**	***v* (m/s)**	***Q* (Lpm)**
1	578.5	9.83	33.32
2	809.88	13.77	46.67
3	1080.84	18.38	62.28
4	1329.20	22.60	76.62
5	1521.09	25.86	87.66

Table 2 above shows the flow rate values for both Blue Model and Clear Prototype. Nevertheless, the parameters are too extreme for such experiment using water. The volume flow rate is scaled down to accommodate the pump power and other devices.

Although a centrifugal pump has a capability of delivering 80 Lpm flow rate but the maximum flow rate that the existing system can carry is up to 28 Lpm only. New parameters setting for the volume flow rate were set to 10, 15, 20, 25 and maximum 28 Lpm. All the visualization results were captured from these inputs.

Setup

Though numerical studies using computer simulations can stimulate research activity among researchers but the practice of experiment using actual test rig still cannot be replaced. Results obtained from the experiments are more viable compared to the simulations [14]. The visualization experiments were conducted to realize the existence of vortex phenomena in the tube. Flow visualization experiment using dye injection technique [15] also referred. The research findings mention about vortical motions. The motions can be classified into transverse and longitudinal vortices. The axis of a transverse vortex lies perpendicular to the flow direction while longitudinal vortices have their axes parallel to the main flow direction. The longitudinal vortex flow may swirl around the primary flow and exhibits three dimensional characteristics. In general, longitudinal vortices are more effective than transverse vortices from the heat transfer perspective.

The current experiment was conducted based on interpretation how to visualize the flow pattern inside the tube. A number of techniques were adapted in the experiments specifically to extract the forward and backward flow. Some phenomena were recorded in still picture and a series of movement flows' video was documented as segregated frame. The usage of bubble and dye gave significant result therefore forward and backward flow was investigated.

In order to create a controlled and nearly axisymmetric vortex flow, an enclosed tube was used. The vortex was created in the vortex chamber. Two inlets with 30° incidence angle each were created on the tube wall which direct fluid flow towards cone sides. Upon reaching a stationary cone, the fluid was swirled towards the center and picks up azimuthal velocity due to the conservation of angular momentum. Finally the fluid was drawn towards the cone at the end and formed a vortex line on the central axis of the tube.

Figure 5 below shows the schematic diagram meanwhile Figure 6 represents the experimental setup of flow visualization experiment. The experiment was conducted at ambient room temperature, 29.4 °C with relative humidity of 72%. Temperature of water was recorded as 29°C. The centrifugal pump provided 80 Lpm of water to the system and the flow went through valve, flow meter and pressure gauge. Dye and bubbles were injected at injection port hence the visualizing aids simultaneously fill the Ranque-Hilsch vortex tube at one inlet. The flow was recorded by camera with the assistance of pendaflour lamp. Two discharge outlets (forward and backward flows) released the flow from the Ranque-Hilsch vortex tube and selected parameters were read by two instruments which was pressure gauge and flow meter. Finally, the discharge flow passed a valve and was collected to the water tank.

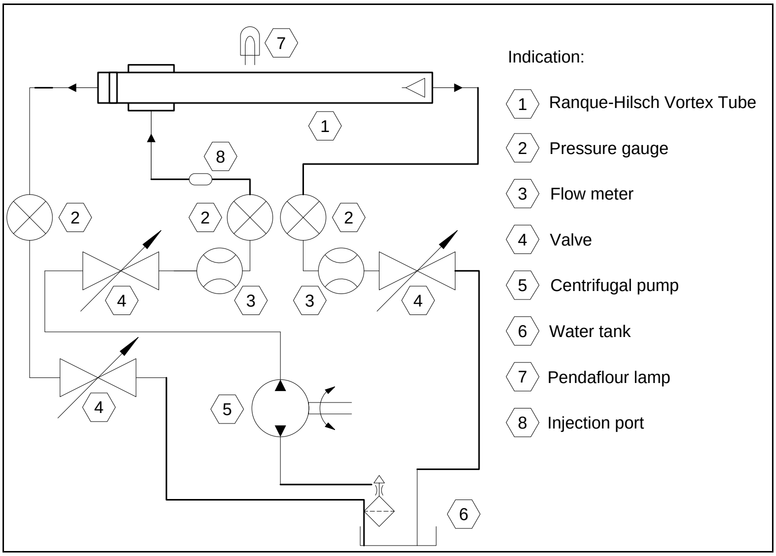

Figure 5: Schematic diagram

Figure 6: Experimental setup of flow visualization experiment

Visualization Results

Visualization of air bubbles

Still photos and video images are recorded and analysed from the flow visualization experiment. The 61 seconds video illustrates the phenomena of RHVT. The video has 1296 frames of pictures which correspond to frame frequency of 21.2 fps. Figure 7 below shows four images representing frames no. 1, 20, 40 and 60.

Three zones are labelled in the figure; Zone 1 (vortex chamber and cold exit), Zone 2 (tube) and Zone 3 (conical valve and hot exit). At first stage, water is pumped to the system continuously until the vortex tube is fully occupied with water. The process is done repeatedly and remaining water is halved when the pump is turning off. This situation creates bubbles in the system as soon as water is injected through the inlet. Referring to Zone 1, it is observed that a vortex is generated at the two inlets at 30^o incidence angle. From observation, bubbles fill entire vortex chamber and creates forced vortex through the tube. Zone 2 shows flow movement of vortex in the whole tube. The projected vortex clearly occupied the tube from the beginning process at (a). Rotation of two vortex layers inside the tube was clearly seen (b). Turbulence fills three-quarter of the tube's space and the effect of conical valve is taking place (c). Tube is fully occupied by water and a suction of back flow can be seen at (d). Video observation for this zone clearly shows rotation of vortex inside the tube. The swirling is nearby internal wall to hot exit and going back to opposite direction (cold exit) in core side. Zone 3 is positioned as conical valve and central of reversal flow. Videos give clear picture of conical valve which serve to redirect the reverse flow [16], [17].

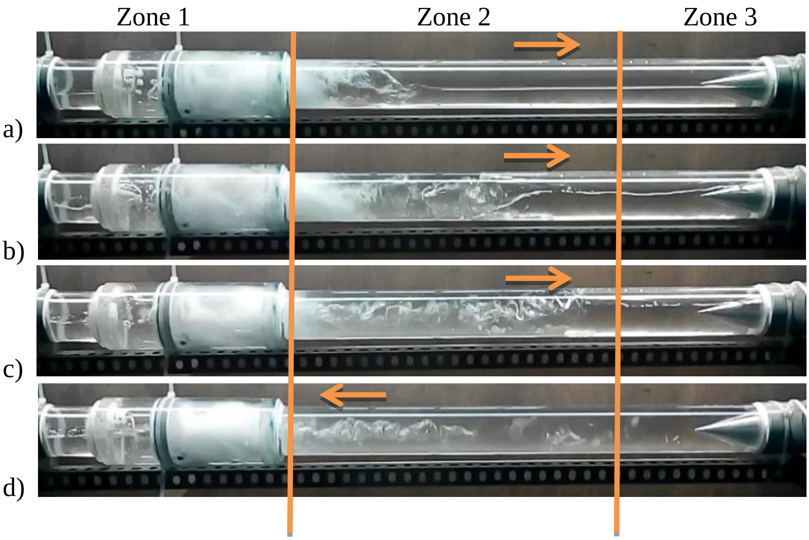

Figure 7: Flow visualization experiment using water at four different instants

Figure 8, 9 and 10 show the flow visualization at Zone 1, 2 and 3 respectively. From the figures, a particle of air bubbles movement can be seen obviously. The captured figures were adapted from 31 seconds video consists of 641 frames which correspond to 21.37 fps [18]. Figure 8 below consists of four pictures showing fluctuation of bubbles in the vortex generator. With high revolution of injected water through the inlet, viscous flow in the peripheral side will move the helical flow to the right side where the conical valve is located. The existing bubbles occur only at the core side of the chamber whereby the revolution at the core side is lesser compared to the peripheral. A line of bubbles is discharged to the left side and it is visible just after the flow passed the orifice. The slow movement of bubbles in this region have a close relation with reverse flow at cold exit [11].

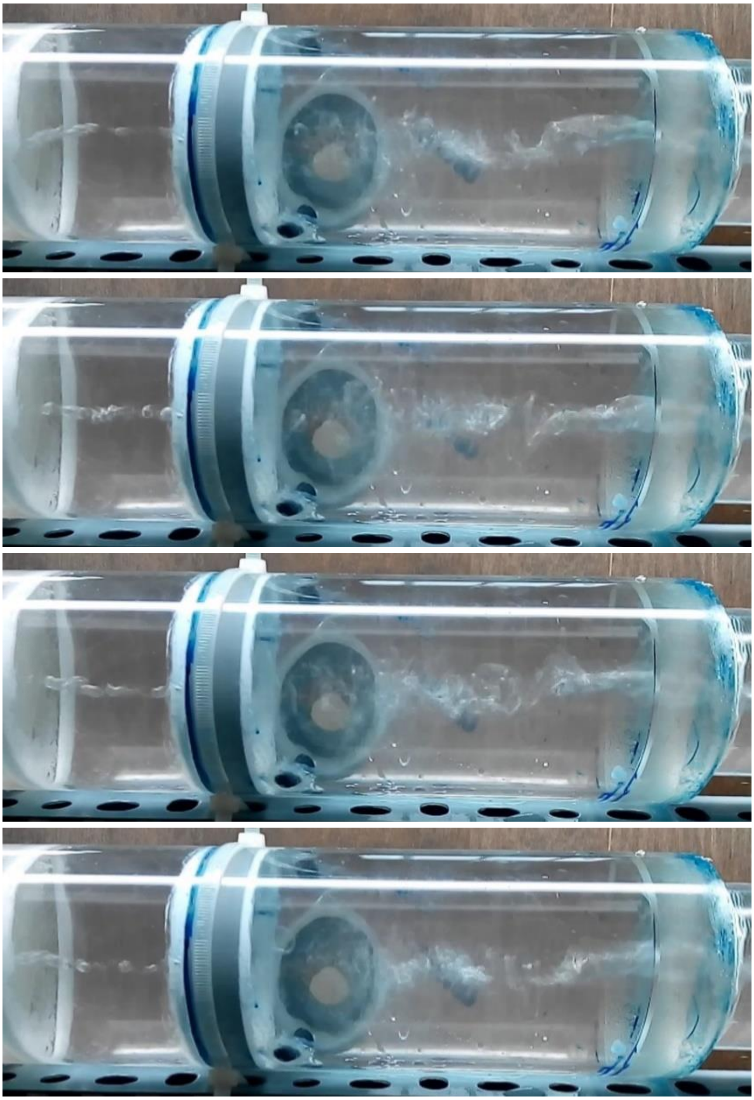

Figure 8: Flow visualization at Zone 1

Figure 9 below shows eight pictures of rotating bubbles inside the tube. The elongation of bubbles can be seen clearly. This phenomenon is a result of discharge flow in the core side of vortex tube. A helical shape of bubble represents the flow pattern of back flow in the system.

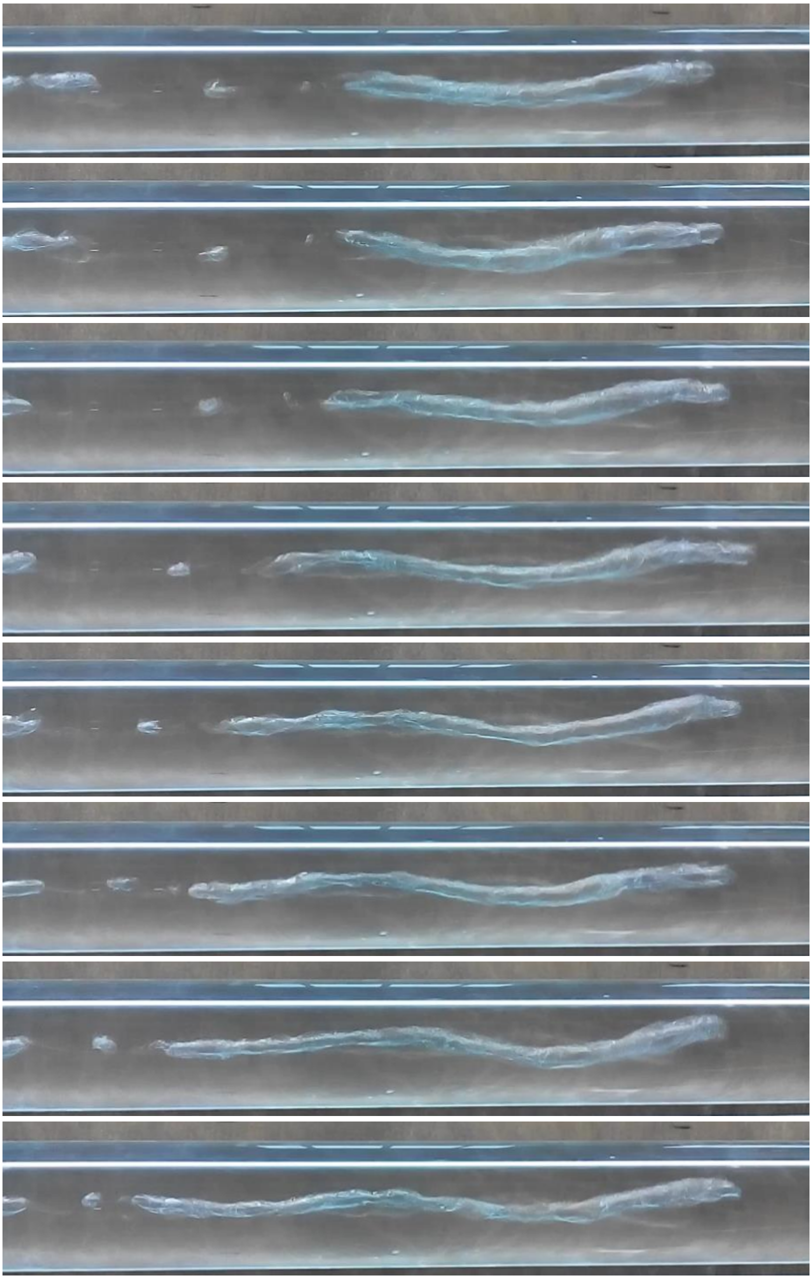

Figure 9: Flow visualization at Zone 2

Figure 10 below consists of seven pictures showing rotational bubbles at the tip of conical valve. A formation of tornado-like bubbles exhibits a high speed rotation flow. Vortex is generated from the con’s tip, moves through core side, elongates and splits into small bubbles. The flow continuously moves to the vortex chamber, passes through orifice and discharges at cold exit.

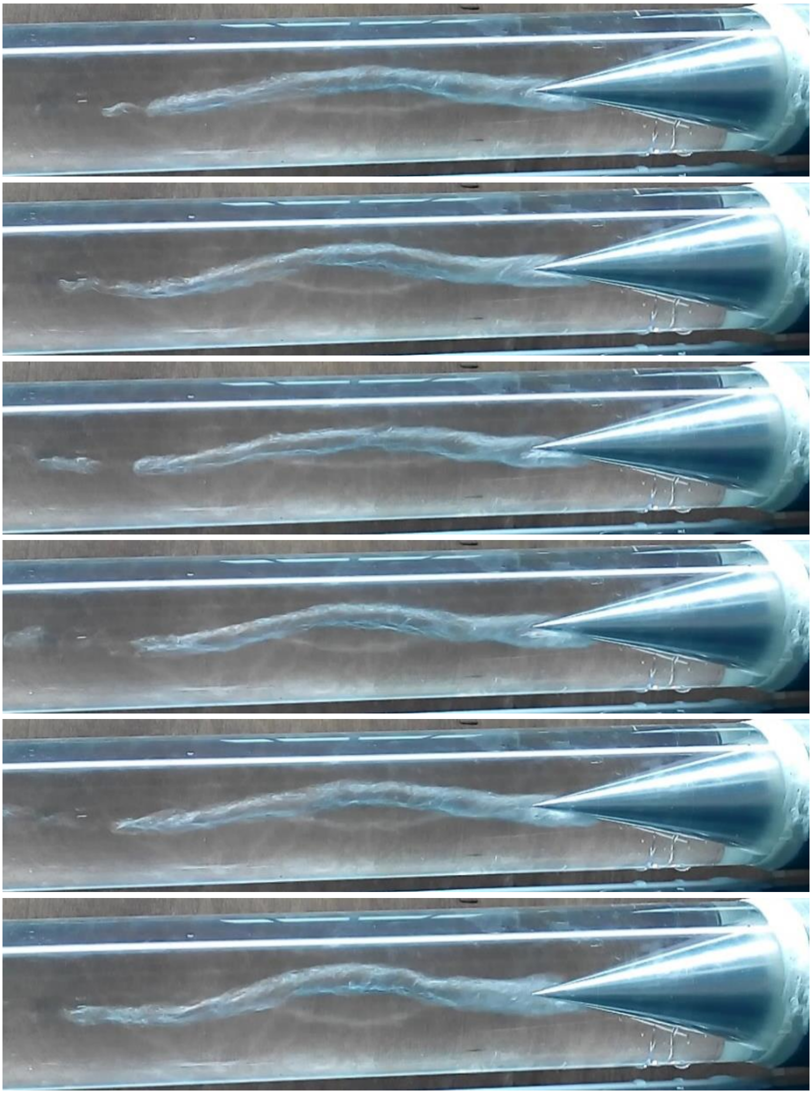

Figure 10: Flow visualization at Zone 3

Visualization using Syrup

Figure 11 below shows several still pictures using syrup. No circulation can be seen except at cold exit. The higher intensity of dye shows water movement from vortex chamber to conical valve. Once tube is fully occupied with dye, all parts are filled with an even tone colour of syrup. Some dyes are discharged at hot exit behind conical valve. Internal core side of flow is seen drawing to hot exit near vortex chamber’s inlet.

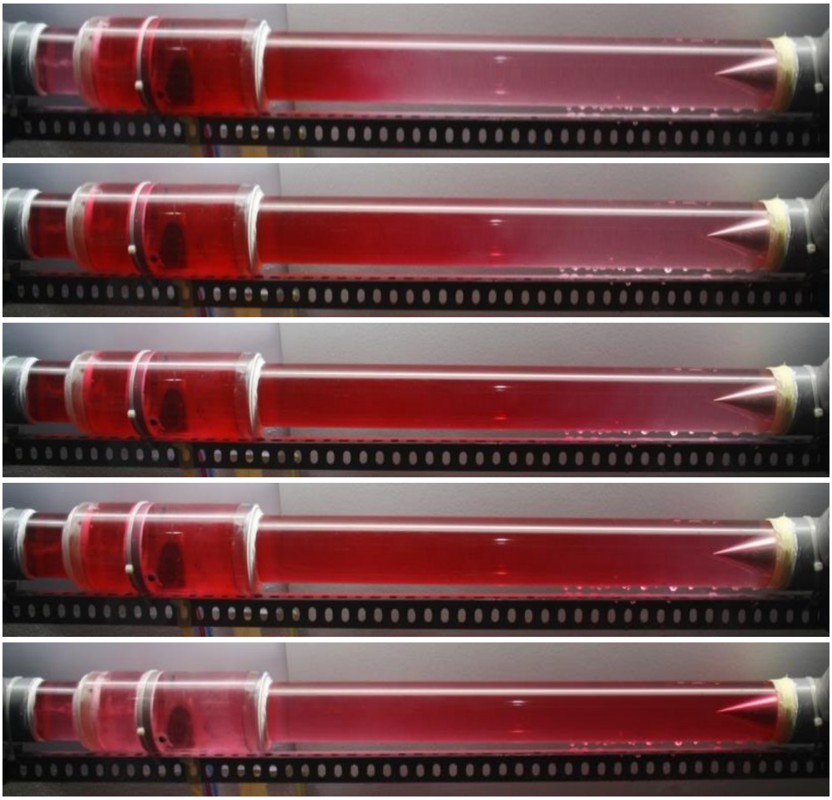

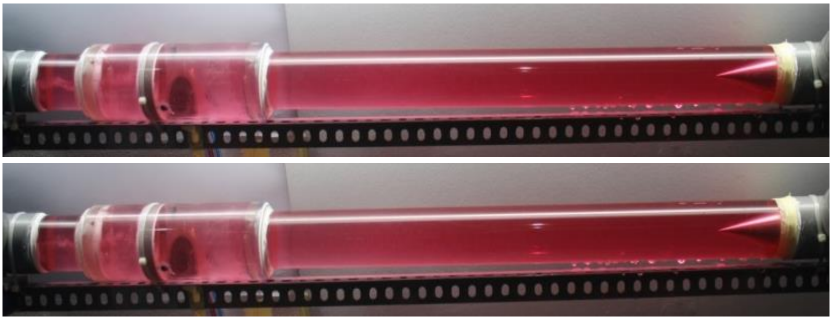

Figure 11: Flow visualization using syrup

Visualization using Bubbles and Syrup

Figure 12 below shows still pictures using bubbles and syrup. This figure gives clear evident in observing flow pattern inside the tube. Circulations of bubbles are apparent and move faster from vortex chamber to conical valve. Back flow return is observed when the circulation touched conical valve. At this point, flow is significantly moved through internal side of the vortex tube. This clearly shows the existence of two flows which is parallel to each other but moved in different direction. Y. Xeu et al [2] showed a multi-circulation region at the same zone and heat was generated by viscous friction.

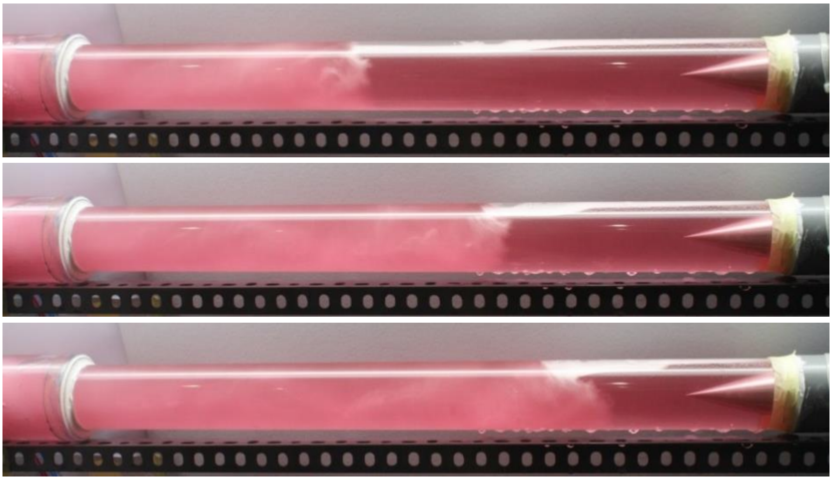

Figure 12: Flow visualization using syrup and bubble

Conclusion

This paper shows the result of flow pattern from flow visualization study. Visualization was conducted using water as the medium. Visualization using bubbles gives interesting result where particles of bubbles can be seen clearly, however the bubbles are a result of unconfined space of filled water. The bubbles are not injected from injection port as in figure 13. Visualization using dye gives fair result but the evident of swirling flow at cold exit is recorded. Experiment using bubbles and syrup contributes to a variety of flow patterns inside vortex tube.

Figure 13: Injection port

The two factors that determine the flow patterns in confined vortex are superimposed axial flow near the peripheral wall and the net flow of fluid which is radially inward or outward with respect to the centreline of the vortex.

Recommendation

It was observed that the bubbles exist in the experiment was not genuinely came from the injection port. It was a result of water pumping at source inlet during the exercise. One alternative method to create bubbles is by using insertion hot wire to the tube. Arrangement of the system should be justified properly and prevention of leakage should be taking into consideration.

Acknowledgment

Authors would like to thank the Business, Research, Industrial Linkages & Consultancy (BRIC), Universiti Selangor (UNISEL), Shah Alam for providing fund and support for this research under Geran Penyelidikan Bestari (No. Projek/No. Vot : GPB-UNISEL14/SG-0001). Special thanks to the Malaysian Ministry of Higher Education (MOHE), the Research

Management Institute (RMI) and the Faculty of Mechanical Engineering, Universiti Teknologi MARA (UiTM) for providing fund and support for this research under Fundamental Research Grant Scheme (FRGS) 600-RMI/ST/FRGS 5/3 (74/2014) and also to Makmal Bendalir, Universiti Selangor (UNISEL), Bestari Jaya and Makmal Termodinamik, Fakulti Kejuruteraan, Universiti Teknologi MARA (UiTM) for providing facilities and tools.

References

[1] S. Eiamsa-ard and P. Promvonge, "Review of Ranque–Hilsch effects in vortex tubes," Renewable and Sustainable Energy Reviews 12, 1822–1842 (2007).

[2] Y. Xue, M. Arjomandi and R. Kelso, "Visualization of the flow structure in a vortex tube," Experimental Thermal and Fluid Sciences 35, 1514-1521 (2011).

[3] O. Aydin and M. Baki, "An experimental study on the design parameters of a counterflow vortex tube," Energy-Oxford 31, 2427-2436 (2006).

[4] V. A. Arbuzov, Y. N. Dubnishchev, A. V. Lebedev, M. K. Pravdina and N. I. Yavorskii, "Observation of large-scale hydrodynamic structures in a vortex tube and the Ranque effect," Institute of Thermal Physics, Siberian Branch of The Russian Academy of Sciences, Novosibirsk 23, 84-90 (1997).

[5] W. Wisnoe, E. S., Shukri, R. Zailani, M. H. Che Mi and M. F. Zakaria, "Numerical investigation of temperature distribution in a diffuser equipped with helical tape," Applied Mechanics and Materials 393, 793-798 (2013).

[6] N. Ismail, W. Wisnoe, and M. F. Remeli, "Experimental investigation on the effect of orifice diameter and inlet pressure to the Ranque-Hilsch vortex tube performance," Applied Mechanics and Materials 465-466, 515-519 (2014).

[7] M. Kurosaka, "Acoustic streaming in swirling flow and the Ranque-Hilsch (vortex-tube) effect," Journal of Fluid Mechanics 124, 139-172 (1982).

[8] Y. Xue, M. Arjomandi and R. Kelso, "Experimental study of the flow structure in a counter flow Ranque–Hilsch vortex tube," International Journal of Heat and Mass Transfer 55, 5853-5860 (2012).

[9] K. Chang-Soo and S. Chang-Hyun, "Dynamic characteristrics of an unsteady flow through a vortex tube," Journal of Mechanical Science and Technology (KSME Int. J.) 20 (12), 2209-2217 (2006).

[10] Y. Istihat and W. Wisnoe, "Wavelet transform of acoustic signal from a Ranque-Hilsch vortex tube," 7th International Conference on Cooling

& Heating Technologies (ICCHT 2014) IOP Conf. Series: Materials Science and Engineering 88, 012005 (2015)

[11] M. Hazwan and H. Katanoda, "Measurement of reverse flow generated at cold exit of vortex tube," World Academy of Science, Engineering and Technology, International Journal of Mathematical, Computational, Physical, Electrical and Computer Engineering 8 (6), 939–942 (2014).

[12] Z. Kadir, "Numerical Study and Fabrication of Ranque-Hilsch Vortex Tube for Flow Visualization," Universiti Selangor, Bachelor Thesis (2015).

[13] M. H. Sabri, "The Visualization Technique for Flow Observation in a Ranque-Hilsch Vortex Tube," Universiti Selangor, Bachelor Thesis (2015)

[14] Y. Istihat, M. Z. Nuawi, A. R. Bahari and W. M. F. W. Mahmood, "Development of Ultrasonic Test Rig System for Fuel Injector," International Review of Mechanical Engineering (I.RE.M.E.), Vol. 6, N. 3 ISSN 1970 - 8734 March 2012. pp. 625-629 (2012)

[15] C. C Wang, J. Lo, Y. T Lin and M. S Liu, "Flow Visualization of Wave-Type Vortex Generators Having Inline Fin-Tube Arrangement," International Journal of Heat and Mass Transfer 45 pp. 1933–1944 (2002)

[16] Y. Istihat, "Vortex Formation in the Whole Body Parts of RHVT – 21.2 fps". Retrieved from http://bit.ly/1YfLOlj (2015, April 01)

[17] Y. Istihat, "Vortex Formation at Chamber and Conical Valve in RHVT – 22.93 fps". Retrieved from http://bit.ly/1tcc6Zo (2015, April 01)

[18] Y. Istihat, "Vortex Formation at Conical Valve, Tube and Chamber in RHVT - 21.37 fps". Retrieved from http://bit.ly/1TXcxOh (2015, April 01)

Journal of Mechanical Engineering *Vol 13(2), 39-59, 2016*

Buckling Analysis of Symmetrically-Laminated Plates using Refined Theory including Curvature Effects

Mokhtar Bouazza
Department of Civil Engineering, University of Bechar, Bechar 08000, Algeria.
Laboratory of Materials and Hydrology (LMH), University of Sidi Bel Abbes, Sidi Bel Abbes 2200, Algeria.

Abdelaziz Lairedj
Department of mechanical Engineering, University of Bechar, Bechar 08000, Algeria.

Noureddine Benseddiqd
Mechanics Laboratory of Lille, CNRS UMR 8107, University of Lille 1, 59655 Villeneuve d'Ascq, France

ABSTRACT

A refined theory is successfully extended in this study for critical buckling loads of rectangular, symmetrically-laminated plates, including curvature effects. The theory accounts for a quadratic variation of the transverse shear strains across the thickness, and satisfies the zero traction boundary conditions on the top and bottom surfaces of the plate and avoids the need of shear correction factors. The numerical results are presented for critical buckling loads for orthotropic laminates subjected to biaxial inplane loading. Using the Navier solution method, the differential equations have been solved analytically and the critical buckling loads presented in closed-form solutions. The significant effects of curvature terms on buckling loads are studied, with various loading conditions and thickness-side ratio. Some exact buckling solutions for simplified cases with and without the inclusion of curvature terms are obtained and compared with results available elsewhere in literature.

Keywords: *Buckling, Symmetrically-laminated, Refined Theory (RT), Curvature Effects.*

ISSN 1823- 5514

Received for review: 2015-12-12
Accepted for publication: 2016-10-17
Published: 2016-12-19

Nomenclature

x, y, z	Directions of Cartesian coordinate system
u, v, w	In-plane displacements
w_b and w_s	Bending and shear components of transverse displacement, respectively
a, b	Plate length and width, respectively
h	Plate thickness
E_1 and E_2	Young's moduli along and transverse to the fibre, respectively
G_{12} , G_{23} and G_{13}	In-plane and transverse shear moduli
v_{12} and v_{21}	Poisson's ratios along and transverse to the fibre, respectively
k	Number of layers
Q_{ij}	Plane stress reduced elastic constants in the material axes of the plate
$\overline{Q}_{ij}$	Transformed material constants
$A_{ij}, A_{ij}^s, D_{ij}, D_{ij}^s, H_{ij}^s$	Plate stiffness
M_i^b, M_i^s, Q_j $(i=x,y,xy \ \& \ j=xz, yz)$	Resultants moments, shear forces, respectively
$\sigma_x^0, \sigma_y^0, \tau_{xy}^0$	In-plane stresses
$\varepsilon_x^{Nl}, \varepsilon_y^{Nl}, \gamma_{xy}^{Nl}$	Second order strain
U	Strain energy of the plate
V	Potential energy of the plate
V_1	In-plane force terms
V_2	Curvature terms
N	Force per unit length
ξ	Load parameter
$\overline{N}$	Critical buckling factor
N_{cr}	Critical buckling Load
L_{ij}	Linear operators
c_c	Scalar indicator of curvature terms
m, n	Number of half waves in the x- and y-directions, respectively

Introduction

The advancement of technology in the search of structural materials with high specific strength and stiffness properties has resulted in the application of laminated composites in aerospace and transportation industries. The increasingly wider application to other fields of engineering has necessitated the evolution of adequate analytical tools for the better understanding of the structural behaviour and efficient utilization of the materials.

Recently, Khalili et al [1] studied the buckling analysis of the sandwich plates for the general cases of the problem and the analytical exact solutions using a simple and fast computational code. Moita et al. [2], finite element model is presented for buckling and geometrically nonlinear analysis of multilayer sandwich structures and shells, with a soft core sandwiched between stiff elastic layers. Ruocco [3] examined the influence of the nonlinear Green–Lagrange strain tensor terms on the buckling of orthotropic, moderately thick plates by the Mindlin hypotheses. Raju et al [4] studied the buckling and postbuckling of variable angle tow composite plates under in-plane shear loading. Kazemi [5] proposed a new method for calculating the critical buckling load has been developed based on the polar representation of tensors. This method can help to analyze the influence of anisotropy on the buckling behavior of simply supported rectangular laminated plates subjected to biaxial compression, thus avoiding the complexities associated with the Cartesian formulation. Chalak et al [6] proposed a new plate model is proposed for the stability analysis of laminated sandwich plate having a soft compressible core based on higher-order zig-zag theory. Kumar et al [7] presented the design of a graded fiber-reinforced composite lamina and graded laminates with an objective of reduced inter-laminar stress-discontinuity in composite laminates. Thai et al [8] presented the novel numerical approach using a NURBS-based isogeometric approach associated with third-order shear deformation theory (TSDT) is formulated for static, free vibration, and buckling analysis of laminated composite plate structures. Rachchhet al. [9] studied the Effect of red mud filler on mechanical and buckling characteristics of coir fibre reinforced polymer composite. Bohlooly and Mirzavand [10] studied Buckling and postbuckling behavior of symmetric laminated composite plates with surface mounted and embedded piezoelectric actuators subjected to mechanical, thermal, electrical, and combined loads. Venkatachari et. al. [11] examined buckling characteristics of curvilinear fibre composite laminates exposed to hygrothermal environment. The formulation is based on the transverse shear deformation theory and it accounts for the lamina material properties at elevated moisture concentrations and thermal gradients. Kumar et. Al. [12] proposed a new lamination scheme is through the design of a graded orthotropic fiber-reinforced composite ply for achieving continuous variations of material properties along the thickness direction of laminated composite plates.

In the past three decades, researches on laminated plates have received great attention, and a variety of plate theories has been introduced based on considering the transverse shear deformation effect. The classical plate theory (CPT), which neglects the transverse shear deformation effect, provides reasonable results for thin plate [13-15].The Reissner [16] and Mindlin [17] theories are known as the first-order shear deformation plate theory (FSDT), and account for the transverse shear effect by the way of linear variation of in-plane displacements through the thickness. There are many two dimensional theories that have been proposed to account for the shear deformation of moderately deep structures and highly anisotropic composites. Reddy [18] proposed a parabolic shear deformation plate theory. Touratier [19] proposed a trigonometric shear deformation plate theory where the transverse strain distribution is given as a sine function. Soldatos [20] proposed a hyperbolic shear deformation plate theory. Aydogdu [21] presented a new shear deformation theory for laminated composite plates. Therefore, Lee et al. [22] proposed a higher-order shear deformable theory using the similar approach of representing transverse displacement using two components. Recently, Shimpi [23] has developed a new refined plate theory which is simple to use and extended by Shimpi and Patel [24,25] for orthotropic plates.

To the best of authors' knowledge, there are no research works for mechanical buckling analysis of laminated plates based on new refined theory including curvature effects. In this work, the effect of curvature terms on the buckling analysis of symmetrically-laminated rectangular plates subjected to biaxial inplane loading has been investigated using the refined theory and Navier solution. The formulation theory accounts for the shear deformation effects without requiring a shear correction factor. Number of unknown functions involved is only two, as against three in case of simple shear deformation theories of Mindlin and Reissner and common higher-order shear deformation theories. Governing equations have been developed for determining critical buckling loads of rectangular, symmetrically-laminated plates, including transverse shear deformation and curvature effects. Using the Navier solution method, the differential equations have been solved analytically and the critical buckling loads presented in closed-form solutions. The sensitivity of critical buckling loads to the effects of curvature terms and other factors has been examined. The analysis is validated by comparing results with those in the literature. The basic equations of plane problem and the general solution for mechanical buckling of laminated plate including curvature effects are given in Section 2. The numerical examples are given in Section 3 and a summary is given in Section 4.

Theoretical Formulation

Buckling of symmetric, anisotropic laminates plates

The displacement field, which accounts for parabolic variation of transverse shear stress through the thickness, and satisfies the zero traction boundary conditions on the top and bottom faces of the plate, is assumed as follows [22,23]:

$$
\begin{aligned}
u(x,y,z) &= -z\frac{\partial w_b}{\partial x} + \left[\frac{1}{4}z - \frac{5}{3}z\left(\frac{z}{h}\right)^2\right]\frac{\partial w_s(x,y)}{\partial x} \\
v(x,y,z) &= -z\frac{\partial w_b}{\partial y} + \left[\frac{1}{4}z - \frac{5}{3}z\left(\frac{z}{h}\right)^2\right]\frac{\partial w_s(x,y)}{\partial y} \\
w(x,y,z) &= w_b(x,y) + w_s(x,y)
\end{aligned}
\tag{1}
$$

where w_b and w_s are the bending and shear components of transverse displacement, respectively; and h is the plate thickness. The kinematic relations can be obtained as follows:

$$
\begin{aligned}
&\{\varepsilon\} = \{k^b\}z + \{k^s\}f(z) \\
&\begin{Bmatrix}\gamma_{yz} \\ \gamma_{xz}\end{Bmatrix} = \begin{Bmatrix}\gamma_{yz}^s \\ \gamma_{xz}^s\end{Bmatrix} g(z)
\end{aligned}
\tag{2}
$$

where

$$
\begin{aligned}
&\{\varepsilon\} = \{\varepsilon_x, \varepsilon_y, \gamma_{xy}\}^T \\
&\{k^b\} = \{k_x^b, k_y^b, k_{xy}^b\}^T = \left\{-\frac{\partial^2 w_b}{\partial x^2}, -\frac{\partial^2 w_b}{\partial y^2}, -2\frac{\partial^2 w_b}{\partial x \partial y}\right\}^T \\
&\{k^s\} = \{k_x^s, k_y^s, k_{xy}^s\}^T = \left\{-\frac{\partial^2 w_s}{\partial x^2}, -\frac{\partial^2 w_s}{\partial y^2}, -2\frac{\partial^2 w_s}{\partial x \partial y}\right\}^T \\
&\gamma_{xz}^s = \frac{\partial w_s}{\partial x}, \gamma_{yz}^s = \frac{\partial w_s}{\partial y} \\
&f(z) = -\frac{1}{4}z + \frac{5}{3}z\left(\frac{z}{h}\right)^2, \; f'(z) = \frac{df(z)}{dz}, \; g(z) = 1 - f'(z),
\end{aligned}
\tag{3}
$$

Constitutive equations

Under the assumption that each layer possesses a plane of elastic symmetry parallel to the x–y plane, the constitutive equations for a layer can be written as

$$\begin{Bmatrix} \sigma_x \\ \sigma_y \\ \sigma_{xy} \\ \sigma_{yz} \\ \sigma_{xz} \end{Bmatrix} = \begin{bmatrix} Q_{11} & Q_{12} & 0 & 0 & 0 \\ Q_{12} & Q_{22} & 0 & 0 & 0 \\ 0 & 0 & Q_{66} & 0 & 0 \\ 0 & 0 & 0 & Q_{44} & 0 \\ 0 & 0 & 0 & 0 & Q_{55} \end{bmatrix} \begin{Bmatrix} \varepsilon_x \\ \varepsilon_y \\ \gamma_{xy} \\ \gamma_{yz} \\ \gamma_{xz} \end{Bmatrix} \tag{4}$$

where

$$Q_{11} = \frac{E_1}{1-\nu_{12}\nu_{21}}, Q_{12} = \frac{\nu_{12}E_2}{1-\nu_{12}\nu_{21}}, Q_{22} = \frac{E_2}{1-\nu_{12}\nu_{21}}$$
$$Q_{66} = G_{12}, Q_{44} = G_{23}\ , \ Q_{55} = G_{13} \tag{5}$$

Transforming the above equations of an arbitrary k layer in local coordinate system into the global coordinate system, the laminate constitutive equations can be expressed as

$$\begin{Bmatrix} \sigma_x \\ \sigma_y \\ \sigma_{xy} \\ \sigma_{yz} \\ \sigma_{xz} \end{Bmatrix}^{(k)} = \begin{bmatrix} \overline{Q}_{11} & \overline{Q}_{12} & \overline{Q}_{16} & 0 & 0 \\ \overline{Q}_{12} & \overline{Q}_{22} & \overline{Q}_{26} & 0 & 0 \\ \overline{Q}_{16} & \overline{Q}_{26} & \overline{Q}_{66} & 0 & 0 \\ 0 & 0 & 0 & \overline{Q}_{44} & \overline{Q}_{45} \\ 0 & 0 & 0 & \overline{Q}_{45} & Q_{55} \end{bmatrix}^{(k)} \begin{Bmatrix} \varepsilon_x \\ \varepsilon_y \\ \gamma_{xy} \\ \gamma_{yz} \\ \gamma_{xz} \end{Bmatrix}^{(k)} \tag{6}$$

where usual notations for normal and shear stress components are adopted. The relationship of the global reduced stiffness matrix $\overline{Q}_{ij}$ can be referred to any standard texts such as [26, 27].

Governing equation

The strain energy of the plate is calculated by

$$2U = \int_V \sigma_{ij}\varepsilon_{ij}dV = \int_V \left(\sigma_x\varepsilon_x + \sigma_y\varepsilon_y + \sigma_{xy}\gamma_{xy} + \sigma_{yz}\gamma_{yz} + \sigma_{xz}\gamma_{xz}\right)dV \tag{7}$$

Substituting Eq. (2) into Eq. (7) and integrating through the thickness of the plate, the strain energy of the plate can be rewritten as

$$2U = \int_A \left[M_x^b \delta k_x^b + M_y^b \delta k_y^b + M_{xy}^b k_{xy}^b + M_x^s k_x^s + M_y^s k_y^s + M_{xy}^s k_{xy}^s + Q_{yz}\gamma_{yz}^s + Q_{xz}\gamma_{xz}^s\right]dxdy \tag{8}$$

where (M_x^b, M_y^b, M_{xy}^b), (M_x^s, M_y^s, M_{xy}^s) denote the total moment resultants and (Q_{xz}, Q_{yz}) are transverse shear stress resultants and they are defined as

$$
\begin{aligned}
(M_x^b, M_y^b, M_{xy}^b) &= \int_{-h/2}^{h/2} (\sigma_x, \sigma_y, \sigma_{xy}) z dz \\
(M_x^s, M_y^s, M_{xy}^s) &= \int_{-h/2}^{h/2} (\sigma_x, \sigma_y, \sigma_{xy}) f(z) dz \\
(Q_{xz}, Q_{yz}) &= \int_{-h/2}^{h/2} (\sigma_{xz}, \sigma_{yz}) g(z) dz
\end{aligned}
\tag{9}
$$

From Eq. (9), one can obtain the following equations:

$$
\begin{bmatrix} M_x^b \\ M_y^b \\ M_{xy}^b \end{bmatrix} = \begin{bmatrix} D_{11} & D_{12} & D_{16} \\ D_{12} & D_{22} & D_{26} \\ D_{16} & D_{26} & D_{66} \end{bmatrix} \begin{bmatrix} -\dfrac{\partial^2 w_b}{\partial x^2} \\ -\dfrac{\partial^2 w_b}{\partial y^2} \\ -2\dfrac{\partial^2 w_b}{\partial x \partial y} \end{bmatrix} + \begin{bmatrix} D_{11}^s & D_{12}^s & D_{16}^s \\ D_{12}^s & D_{22}^s & D_{26}^s \\ D_{16}^s & D_{26}^s & D_{66}^s \end{bmatrix} \begin{bmatrix} -\dfrac{\partial^2 w_s}{\partial x^2} \\ -\dfrac{\partial^2 w_s}{\partial y^2} \\ -2\dfrac{\partial^2 w_s}{\partial x \partial y} \end{bmatrix} \tag{10}
$$

$$
\begin{bmatrix} M_x^s \\ M_y^s \\ M_z^s \end{bmatrix} = \begin{bmatrix} D_{11}^s & D_{12}^s & D_{16}^s \\ D_{12}^s & D_{22}^s & D_{26}^s \\ D_{16}^s & D_{26}^s & D_{66}^s \end{bmatrix} \begin{bmatrix} -\dfrac{\partial^2 w_b}{\partial x^2} \\ -\dfrac{\partial^2 w_b}{\partial y^2} \\ -2\dfrac{\partial^2 w_b}{\partial x \partial y} \end{bmatrix} + \begin{bmatrix} H_{11}^s & H_{12}^s & H_{16}^s \\ H_{12}^s & H_{22}^s & H_{26}^s \\ H_{16}^s & H_{26}^s & H_{66}^s \end{bmatrix} \begin{bmatrix} -\dfrac{\partial^2 w_s}{\partial x^2} \\ -\dfrac{\partial^2 w_s}{\partial y^2} \\ -2\dfrac{\partial^2 w_s}{\partial x \partial y} \end{bmatrix} \tag{11}
$$

$$
\begin{bmatrix} Q_y \\ Q_x \end{bmatrix} = \begin{bmatrix} A_{44}^s & A_{45}^s \\ A_{45}^s & A_{55}^s \end{bmatrix} \begin{bmatrix} \partial w_s / \partial y \\ \partial w_s / \partial x \end{bmatrix} \tag{12}
$$

where,

$$
\begin{aligned}
(D_{ij}, D_{ij}^s, H_{ij}^s) &= \int_{-h/2}^{h/2} \overline{Q}_{ij} (z^2, zf(z), (f(z))^2) dz \quad (i, j = 1,2,6) \\
A_{ij}^s &= \int_{-h/2}^{h/2} \overline{Q}_{ij} (g(z))^2 dz \qquad (i, j = 4,5)
\end{aligned}
\tag{13}
$$

Substituting Eqs. (10) - (12) and (3) to Eq. (8), the strain energy per unit area, U, due to the buckling deformation is of the form

$$
\begin{aligned}
2U &= D_{11}\frac{\partial^4 w_b}{\partial x^4} + D_{22}\frac{\partial^4 w_b}{\partial y^4} + 2\left(D_{12}+2D_{66}\right)\frac{\partial^4 w_b}{\partial x^2\partial y^2} + 4D_{16}\frac{\partial^4 w_b}{\partial x^3\partial y} + 4D_{26}\frac{\partial^4 w_b}{\partial x\partial y^3} \\
&+ 2D_{11}^s\frac{\partial^2 w_b}{\partial x^2}\frac{\partial^2 w_s}{\partial x^2} + 2D_{22}^s\frac{\partial^2 w_b}{\partial y^2}\frac{\partial^2 w_s}{\partial y^2} + 2D_{12}^s\frac{\partial^2 w_b}{\partial x^2}\frac{\partial^2 w_s}{\partial y^2} + 2D_{12}^s\frac{\partial^2 w_b}{\partial y^2}\frac{\partial^2 w_s}{\partial x^2} \\
&+ 4D_{16}^s\frac{\partial^2 w_b}{\partial x^2}\frac{\partial^2 w_s}{\partial x\partial y} + 4D_{16}^s\frac{\partial^2 w_b}{\partial x\partial y}\frac{\partial^2 w_s}{\partial x^2} + 4D_{26}^s\frac{\partial^2 w_b}{\partial y^2}\frac{\partial^2 w_s}{\partial x\partial y} + 4D_{26}^s\frac{\partial^2 w_b}{\partial x\partial y}\frac{\partial^2 w_s}{\partial y^2} \\
&+ 8D_{66}^s\frac{\partial^2 w_b}{\partial x\partial y}\frac{\partial^2 w_s}{\partial x\partial y} H_{11}^s\frac{\partial^4 w_s}{\partial x^4} + H_{22}^s\frac{\partial^4 w_s}{\partial y^4} + 2\left(H_{12}^s+2H_{66}^s\right)\frac{\partial^4 w_s}{\partial x^2\partial y^2} + 4H_{16}^s\frac{\partial^4 w_s}{\partial x^3\partial y} \\
&+ 4H_{26}^s\frac{\partial^4 w_s}{\partial x\partial y^3} + A_{44}^s\frac{\partial^2 w_s}{\partial y^2} + A_{55}^s\frac{\partial^2 w_s}{\partial x^2} + 2A_{45}^s\frac{\partial^2 w_s}{\partial x\partial y}
\end{aligned} \tag{14}
$$

The potential energy of the applied in-plane stresses σ_x^0, σ_y^0 and τ_{xy}^0 arises from the action of the applied d stresses on the corresponding second order strain $\varepsilon_x^{Nl}, \varepsilon_y^{Nl}$ and γ_{xy}^{Nl}. Following the usual procedure [28, 29], after taking into account the displacement field given by Equation (1)

$$
\begin{aligned}
\varepsilon_x^{Nl} &= \frac{z^2}{2}\left[\frac{\partial^4 w_b}{\partial x^4} + \frac{\partial^4 w_b}{\partial x^2\partial y^2}\right] + zf(z)\left[\frac{\partial^2 w_b}{\partial x^2}\frac{\partial^2 w_s}{\partial x^2} + \frac{\partial w_b^2}{\partial x\partial y}\frac{\partial^2 w_s}{\partial x\partial y}\right] \\
&+ \frac{f(z)^2}{2}\left[\frac{\partial^4 w_s}{\partial x^4} + \frac{\partial^4 w_s}{\partial x^2\partial y^2}\right] + \frac{1}{2}\left(\frac{\partial^2 w_b}{\partial x^2} + \frac{\partial^2 w_s}{\partial x^2} + 2\frac{\partial w_b}{\partial x}\frac{\partial w_s}{\partial x}\right)
\end{aligned} \tag{15}
$$

$$
\begin{aligned}
\varepsilon_y^{Nl} &= \frac{z^2}{2}\left[\frac{\partial^4 w_b}{\partial y^4} + \frac{\partial^4 w_b}{\partial x^2\partial y^2}\right] + zf(z)\left[\frac{\partial^2 w_b}{\partial y^2}\frac{\partial^2 w_s}{\partial y^2} + \frac{\partial^2 w_b}{\partial x\partial y}\frac{\partial^2 w_s}{\partial x\partial y}\right] \\
&+ \frac{f(z)^2}{2}\left[\frac{\partial^4 w_s}{\partial y^4} + \frac{\partial^4 w_s}{\partial x^2\partial y^2}\right] + \frac{1}{2}\left(\frac{\partial^2 w_b}{\partial y^2} + \frac{\partial^2 w_s}{\partial y^2} + 2\frac{\partial w_b}{\partial y}\frac{\partial w_s}{\partial y}\right)
\end{aligned} \tag{16}
$$

$$
\begin{aligned}
\gamma_{xy}^{Nl} &= z^2\left[\frac{\partial^4 w_b}{\partial x^3\partial y} + \frac{\partial^4 w_b}{\partial x\partial y^3}\right] + zf(z)\left[\frac{\partial^2 w_b}{\partial x^2}\frac{\partial^2 w_s}{\partial x\partial y} + \frac{\partial^2 w_b}{\partial y^2}\frac{\partial^2 w_s}{\partial x\partial y} + \frac{\partial^2 w_s}{\partial x^2}\frac{\partial^2 w_b}{\partial x\partial y} + \frac{\partial^2 w_s}{\partial y^2}\frac{\partial^2 w_b}{\partial x\partial y}\right] \\
&+ f(z)^2\left[\frac{\partial^4 w_s}{\partial x^3\partial y} + \frac{\partial^4 w_s}{\partial x\partial y^3}\right] + \left(\frac{\partial^2 w_b}{\partial x\partial y} + \frac{\partial^2 w_s}{\partial x\partial y} + \frac{\partial w_b}{\partial x}\frac{\partial w_s}{\partial y} + \frac{\partial w_b}{\partial y}\frac{\partial w_s}{\partial x}\right)
\end{aligned} \tag{17}
$$

The potential energy of the plate fiat of volume is

$$
V = \int_{-h/2}^{h/2}\left(\sigma_x^0\varepsilon_x^{Nl} + \sigma_y^0\varepsilon_y^{Nl} + \tau_{xy}^0\gamma_{xy}^{Nl}\right)dz \tag{18}
$$

Denoting conventional inplane force terms by V_1 and "curvature" terms by V_2, then after combining Equations (15)-(17) and (18) we find that

$$V = V_1 + V_2 \tag{19}$$

where

$$2V_1 = N_x^0\left(\frac{\partial^2 w_b}{\partial x^2}+\frac{\partial^2 w_s}{\partial x^2}+2\frac{\partial w_b}{\partial x}\frac{\partial w_s}{\partial x}\right)+N_y^0\left(\frac{\partial^2 w_b}{\partial y^2}+\frac{\partial^2 w_s}{\partial y^2}+2\frac{\partial w_b}{\partial y}\frac{\partial w_s}{\partial y}\right) \tag{20}$$

$$+2N_{xy}^0\left(\frac{\partial^2 w_b}{\partial x\partial y}+\frac{\partial^2 w_s}{\partial x\partial y}+\frac{\partial w_b}{\partial x}\frac{\partial w_s}{\partial y}+\frac{\partial w_b}{\partial y}\frac{\partial w_s}{\partial x}\right)$$

$$2V_2 = \int_{-h/2}^{h/2}\left(\begin{array}{l}\left\{\sigma_x^0\left[\frac{\partial^4 w_b}{\partial x^4}+\frac{\partial^4 w_b}{\partial x^2\partial y^2}\right]+\sigma_y^0\left[\frac{\partial^4 w_b}{\partial y^4}+\frac{\partial^4 w_b}{\partial x^2\partial y^2}\right]+2\tau_{xy}^0\left[\frac{\partial^4 w_b}{\partial x^3\partial y}+\frac{\partial^4 w_b}{\partial x\partial y^3}\right]\right\}z^2 \\ \left\{\begin{array}{l}2\sigma_x^0\left[\frac{\partial^2 w_b}{\partial x^2}\frac{\partial^2 w_s}{\partial x^2}+\frac{\partial w_b^2}{\partial x\partial y}\frac{\partial^2 w_s}{\partial x\partial y}\right]+2\sigma_y^0\left[\frac{\partial^2 w_b}{\partial y^2}\frac{\partial^2 w_s}{\partial y^2}+\frac{\partial^2 w_b}{\partial x\partial y}\frac{\partial^2 w_s}{\partial x\partial y}\right] \\ 2\tau_{xy}^0\left[\frac{\partial^2 w_b}{\partial x^2}\frac{\partial^2 w_s}{\partial x\partial y}+\frac{\partial^2 w_b}{\partial y^2}\frac{\partial^2 w_s}{\partial x\partial y}+\frac{\partial^2 w_s}{\partial x^2}\frac{\partial^2 w_b}{\partial x\partial y}+\frac{\partial^2 w_s}{\partial y^2}\frac{\partial^2 w_b}{\partial x\partial y}\right]\end{array}\right\}zf(z) \\ \left\{\sigma_x^0\left[\frac{\partial^4 w_s}{\partial x^4}+\frac{\partial^4 w_s}{\partial x^2\partial y^2}\right]+\sigma_y^0\left[\frac{\partial^4 w_s}{\partial y^4}+\frac{\partial^4 w_s}{\partial x^2\partial y^2}\right]+2\tau_{xy}^0\left[\frac{\partial^4 w_s}{\partial x^3\partial y}+\frac{\partial^4 w_s}{\partial x\partial y^3}\right]\right\}f(z)^2\end{array}\right)dz \tag{21}$$

In addition

$$\left(N_x^0, N_y^0, N_{xy}^0\right)=\int_{-h/2}^{h/2}\left\{\sigma_x^0,\sigma_y^0,\tau_{xy}^0\right\}dz \tag{22}$$

In order to put the integral in Equation (21) in a useful form for heterogeneous plates, we utilize the constitutive relations for the inplane loading of a symmetrically-laminated plate [30, 31]

$$\begin{bmatrix} N_x^0 \\ N_y^0 \\ N_{xy}^0 \end{bmatrix}=\begin{bmatrix} A_{11} & A_{12} & A_{16} \\ A_{12} & A_{22} & A_{26} \\ A_{16} & A_{26} & A_{66} \end{bmatrix}\begin{bmatrix} \varepsilon_x^0 \\ \varepsilon_y^0 \\ \gamma_{xy}^0 \end{bmatrix} \tag{23}$$

where

$$A_{ij} = \int_{-h/2}^{h/2} \overline{Q}_{ij} dz \qquad (i, j = 1,2,6) \tag{24}$$

Equation (23) can now be written in the form

$$\varepsilon_{i,j}^{0} = A_{jk}^{*} N_{k}^{0} \qquad (j, k = 1,2,6) \tag{25}$$

where the repeated index denotes summation, and A_{jk}^{*} represents elements of the inverse matrix of A_{jk}. Denoting σ_x^0, σ_y^0 and τ_{xy}^0 by σ_1^0, σ_2^0 and σ_6^0, respectively, we can write the inplane ply constitutive relations in the form:

$$\sigma_i^0 = \overline{Q}_{ij}\, \varepsilon_j^0 \qquad (i, j = 1,2,6) \tag{26}$$

Thus,

$$\begin{aligned}
&\int_{-h/2}^{h/2} \sigma_i^0 z^2 dz = \int_{-h/2}^{h/2} \overline{Q}_{ij}\, \varepsilon_j^0 z^2 dz = D_{ij}\varepsilon_j^0 \\
&\int_{-h/2}^{h/2} \sigma_i^0 z f(z) dz = \int_{-h/2}^{h/2} \overline{Q}_{ij}\, \varepsilon_j^0 z f(z) dz = D_{ij}^s \varepsilon_j^0 \\
&\int_{-h/2}^{h/2} \sigma_i^0 f(z)^2 dz = \int_{-h/2}^{h/2} \overline{Q}_{ij}\, \varepsilon_j^0 f(z)^2 dz = H_{ij}^s \varepsilon_j^0
\end{aligned} \tag{27}$$

Combining Equations (25) and (27), we find that

$$\begin{aligned}
&\int_{-h/2}^{h/2} \sigma_x^0 z^2 dz = D_{ij} A_{jk}^* N_k^0 = F_{jk} N_k^0 \\
&\int_{-h/2}^{h/2} \sigma_{i,j}^0 z f(z) dz = D_{ij}^s A_{jk}^* N_k^0 = F_{jk}^s N_k^0 \\
&\int_{-h/2}^{h/2} \sigma_{i,j}^0 f(z)^2 dz = H_{ij}^s A_{jk}^* N_k^0 = F_{jk}^r N_k^0
\end{aligned} \tag{28}$$

where

$$\begin{aligned}
&F_{jk} = D_{ij} A_{jk}^* \\
&F_{jk}^s = D_{ij}^s A_{jk}^* \\
&F_{jk}^r = H_{ij}^s A_{jk}^*
\end{aligned} \tag{29}$$

Taking into account Equations (28) and (29), the "curvature" terms, Equation (21), are of the form

$$
\begin{aligned}
2V_2 \; &= \left(F_{11}N_x^0 + F_{12}N_y^0 + F_{16}N_{xy}^0\right)\left[\frac{\partial^4 w_b}{\partial x^4} + \frac{\partial^4 w_b}{\partial x^2 \partial y^2}\right] + \left(F_{12}N_x^0 + F_{22}N_y^0 + F_{26}N_{xy}^0\right)\left[\frac{\partial^4 w_b}{\partial y^4} + \frac{\partial^4 w_b}{\partial x^2 \partial y^2}\right] \\
&+ 2\left(F_{16}N_x^o + F_{26}N_y^0 + F_{66}N_{xy}^0\right)\left[\frac{\partial^4 w_b}{\partial x^3 \partial y} + \frac{\partial^4 w_b}{\partial x \partial y^3}\right] + 2\left(F_{11}^s N_x^0 + F_{12}^s N_y^0 + F_{16}^s N_{xy}^0\right)\left[\frac{\partial^2 w_b}{\partial x^2}\frac{\partial^2 w_s}{\partial x^2} + \frac{\partial w_b^2}{\partial x \partial y}\frac{\partial^2 w_s}{\partial x \partial y}\right] \\
&+ 2\left(F_{12}^s N_x^0 + F_{22}^s N_y^0 + F_{26}^s N_{xy}^0\right)\left[\frac{\partial^2 w_b}{\partial y^2}\frac{\partial^2 w_s}{\partial y^2} + \frac{\partial^2 w_b}{\partial x \partial y}\frac{\partial^2 w_s}{\partial x \partial y}\right] \\
&+ 4\left(F_{16}^s N_x^o + F_{26}^s N_y^0 + F_{66}^s N_{xy}^0\right)\left[\frac{\partial^2 w_b}{\partial x^2}\frac{\partial^2 w_s}{\partial x \partial y} + \frac{\partial^2 w_b}{\partial y^2}\frac{\partial^2 w_s}{\partial x \partial y} + \frac{\partial^2 w_s}{\partial x^2}\frac{\partial^2 w_b}{\partial x \partial y} + \frac{\partial^2 w_s}{\partial y^2}\frac{\partial^2 w_b}{\partial x \partial y}\right] \\
&\left(F_{11}^r N_x^0 + F_{12}^r N_y^0 + F_{16}^r N_{xy}^0\right)\left[\frac{\partial^4 w_s}{\partial x^4} + \frac{\partial^4 w_s}{\partial x^2 \partial y^2}\right] + \left(F_{12}^r N_x^0 + F_{22}^r N_y^0 + F_{26}^r N_{xy}^0\right)\left[\frac{\partial^4 w_s}{\partial y^4} + \frac{\partial^4 w_s}{\partial x^2 \partial y^2}\right] \\
&+ 2\left(F_{16}^r N_x^o + F_{26}^r N_y^0 + F_{66}^r N_{xy}^0\right)\left[\frac{\partial^4 w_s}{\partial x^3 \partial y} + \frac{\partial^4 w_s}{\partial x \partial y^3}\right]
\end{aligned}
\tag{30}
$$

Governing equations can be obtained by applying the variational relationship

$$
\delta U + \delta V_1 \; + \delta V_2 \; = 0 \tag{31}
$$

Substituting Equations (14), (20) and (30) into Equation (31), we obtain the following governing equations in operator form

$$
\begin{aligned}
L_{11} w_b + L_{12} w_s &= 0 \\
L_{12} w_b + L_{22} w_s &= 0
\end{aligned}
\tag{32}
$$

The linear operators L_{ij} are defined as follows:

$$
\begin{aligned}
L_{11} &= \left(D_{11} + F_{11}N_x^0 + F_{12}N_y^0 + F_{16}N_{xy}^0\right)\left(\;\right)_{,xxxx} + 2\left(2D_{16} + F_{16}N_x^0 + F_{26}N_y^0 + F_{66}N_{xy}^0\right)\left(\;\right)_{,xxxy} \\
&+ \left(2D_{12} + 4D_{66} + F_{11}N_x^0 + F_{12}N_y^0 + F_{16}N_{xy}^0 + F_{12}N_x^0 + F_{22}N_y^0 + F_{26}N_{xy}^0\right)\left(\;\right)_{,xxyy} \\
&+ \left(D_{22} + F_{12}N_x^0 + F_{22}N_y^0 + F_{26}N_{xy}^0\right)\left(\;\right)_{,yyyy} + 2\left(2D_{26} + F_{16}N_x^0 + F_{26}N_y^0 + F_{66}N_{xy}^0\right)\left(\;\right)_{,xyyy} \\
&+ N_x^0\left(\;\right)_{,xx} + 2N_{xy}^0\left(\;\right)_{,xy} + N_y^0\left(\;\right)_{,yy}
\end{aligned}
\tag{33}
$$

$$L_{12} = \left(D_{11}^s + F_{11}^s N_x^0 + F_{12}^s N_y^0 + F_{16}^s N_{xy}^0\right)(\ )_{,xxxx} + 2\left(2D_{16}^s + 2\left(F_{16}^s N_x^0 + F_{26}^s N_y^0 + F_{66}^s N_{xy}^0\right)\right)(\ )_{,xxxy}$$
$$+ \left(2D_{12}^s + 4D_{66}^s + F_{11}^s N_x^0 + F_{12}^s N_y^0 + F_{16}^s N_{xy}^0 + F_{12}^s N_x^0 + F_{22}^s N_y^0 + F_{26}^s N_{xy}^0\right)(\ )_{,xxyy}$$
$$+ \left(D_{22}^s + F_{12}^s N_x^0 + F_{22}^s N_y^0 + F_{26}^s N_{xy}^0\right)(\ )_{,yyyy} + 2\left(2D_{26}^s + 2\left(F_{16}^s N_x^0 + F_{26}^s N_y^0 + F_{66}^s N_{xy}^0\right)\right)(\ )_{,xyyy}$$
$$+ N_x^0(\ )_{,xx} + 2N_{xy}^0(\ )_{,xy} + N_y^0(\ )_{,yy}$$

$$L_{22} = \left(H_{11}^s + F_{11}^r N_x^0 + F_{12}^r N_y^0 + F_{16}^r N_{xy}^0\right)(\ )_{,xxxx} + \left(4H_{16}^s + 2\left(F_{16}^r N_x^0 + F_{26}^r N_y^0 + F_{66}^r N_{xy}^0\right)\right)(\ )_{,xxxy}$$
$$+ \left(2H_{12}^s + 4H_{66}^s + F_{11}^r N_x^0 + F_{12}^r N_y^0 + F_{16}^r N_{xy}^0 + F_{12}^r N_x^0 + F_{22}^r N_y^0 + F_{26}^r N_{xy}^0\right)(\ )_{,xxyy}$$
$$+ \left(H_{22}^s + F_{12}^r N_x^0 + F_{22}^r N_y^0 + F_{26}^r N_{xy}^0\right)(\ )_{,yyyy} + \left(4H_{26}^s + 2\left(F_{16}^r N_x^0 + F_{26}^r N_y^0 + F_{66}^r N_{xy}^0\right)\right)(\ )_{,xyyy}$$
$$+ A_{55}^s(\ )_{,xx} + A_{44}^s(\ )_{,yy} + 2A_{45}^s(\ )_{,xy} + N_x^0(\ )_{,xx} + 2N_{xy}^0(\ )_{,xy} + N_y^0(\ )_{,yy}$$

Exact solutions of mechanical buckling for symmetric cross-ply plates

Consider a rectangular plate with the length a, and width b which is subjected to in-plane loads. Therefore, the pre-buckling forces can be obtained using the equilibrium conditions as [32, 33]

$$N_x^0 = -N,\ \ N_y^0 = \xi N,\ \ N_{xy}^0 = 0 \qquad (N > 0) \tag{34}$$

Where N the force per unit length is, ξ is the load parameter which indicate the loading conditions. Negative value for ξ indicate that plate is subjected to biaxial compressive loads while positive values are used for tensile loads. Also, zero value for ξ show uniaxial loading in x directions, respectively.

The exact solutions of equations (32) and (33) for simply supported, symmetric cross-ply rectangular plates may be obtained by recognizing the following plate stiffness to have zero values

$$\begin{aligned} &A_{16} = A_{26} = D_{16} = D_{26} = D_{16}^s = D_{26}^s = 0 \\ &H_{16}^s = H_{26}^s = A_{45}^s = 0 \end{aligned} \tag{35}$$

By following the Navier solution procedure, the solutions to the problem are assumed to take the following forms

$$\begin{aligned} w_b(x,y) &= \sum_{m=1}^{\infty}\sum_{n=1}^{\infty} W_{b\,mn} \sin\lambda x \sin\mu y \\ w_s(x,y) &= \sum_{m=1}^{\infty}\sum_{n=1}^{\infty} W_{s\,mn} \sin\lambda x \sin\mu y \end{aligned} \tag{36}$$

where

$$\lambda = \frac{m\pi x}{a}, \mu = \frac{m\pi x}{a} \tag{37}$$

Substituting Equation (36) into Equation (32) for a symmetric cross-ply laminate, we obtain the following equations

$$\begin{aligned}
&\left[D_{11} - c_c N(F_{11} - \xi F_{12})\right]\left(w_b\right)_{,xxxx} + \left[2D_{12} + 4D_{66} - c_c N\left(\left(F_{11} + F_{12}\right) - \xi\left(F_{12} + F_{22}\right)\right)\right]\left(w_b\right)_{,xxyy} \\
&+ \left[D_{22} - c_c N(F_{12} - \xi F_{22})\right]\left(w_b\right)_{,yyyy} + \left[D_{11}^s - c_c N(F_{11}^s - \xi F_{12}^s)\right]\left(w_s\right)_{,xxxx} \\
&+ \left[2D_{12}^s + 4D_{66}^s - c_c N\left(\left(F_{11}^s + F_{12}^s\right) - \xi\left(F_{12}^s + F_{22}^s\right)\right)\right]\left(w_s\right)_{,xxyy} + \left[D_{22}^s - c_c N(F_{12}^s - \xi F_{22}^s)\right]\left(w_s\right)_{,yyyy} \\
&+ N_x^0\left(w_b\right)_{,xx} + N_y^0\left(w_b\right)_{,yy} + N_x^0\left(w_s\right)_{,xx} + N_y^0\left(w_s\right)_{,yy} = 0
\end{aligned} \tag{38}$$

$$\begin{aligned}
&\left[D_{11}^s - c_c N(F_{11}^s - \xi F_{12}^s)\right]\left(w_b\right)_{,xxxx} + \left[2D_{12}^s + 4D_{66}^s - c_c N\left(\left(F_{11}^s + F_{12}^s\right) - \xi\left(F_{12}^s + F_{22}^s\right)\right)\right]\left(w_b\right)_{,xxyy} \\
&+ \left[D_{22}^s - c_c N(F_{12}^s - \xi F_{22}^s)\right]\left(w_b\right)_{,yyyy} + \left[H_{11}^r - c_c N(F_{11}^r - \xi F_{12}^r)\right]\left(w_s\right)_{,xxxx} \\
&+ \left[2H_{12}^s + 4H_{66}^s - c_c N\left(\left(F_{11}^r + F_{12}^r\right) - \xi\left(F_{12}^r + F_{22}^r\right)\right)\right]\left(w_s\right)_{,xxyy} + \left[H_{22}^s - c_c N(F_{12}^r - \xi F_{22}^r)\right]\left(w_s\right)_{,yyyy} \\
&+ N_x^0\left(w_b\right)_{,xx} + N_y^0\left(w_b\right)_{,yy} + \left[A_{55}^s + N_x^0\right]\left(w_s\right)_{,xx} + \left[A_{44}^s + N_y^0\right]\left(w_s\right)_{,yy} = 0
\end{aligned} \tag{39}$$

where c_c takes on the value 1 when the "curvature" terms are included in the analysis and is 0 when these terms are neglected.

After substituting the Eq. (36) into Eqs. (38) and (39) we get a systems of two equations for finding the W_{bmn} and W_{smn}. By equaling the determinant of coefficient to zero we have:

$$\begin{bmatrix} \left(a_1 - N\left(c_c b_1 + c_1\right)\right) & \left(a_2 - N\left(c_c b_2 + c_1\right)\right) \\ \left(a_2 - N\left(c_c b_2 + c_1\right)\right) & \left(a_3 - N\left(c_c b_3 + c_1\right)\right) \end{bmatrix} \begin{bmatrix} W_{bmn} \\ W_{smn} \end{bmatrix} = \begin{bmatrix} 0 \\ 0 \end{bmatrix} \tag{40}$$

where

$$\begin{aligned}
a_1 &= D_{11}\frac{m^4\pi^4}{a^4} + D_{22}\frac{n^4\pi^4}{b^4} + \left(2D_{12} + 4D_{66}\right)\frac{m^2n^2\pi^4}{a^2b^2} \\
a_2 &= D_{11}^s\frac{m^4\pi^4}{a^4} + D_{22}^s\frac{n^4\pi^4}{b^4} + \left(2D_{12}^s + 4D_{66}^s\right)\frac{m^2n^2\pi^4}{a^2b^2} \\
a_3 &= H_{11}^s\frac{m^4\pi^4}{a^4} + H_{22}^s\frac{n^4\pi^4}{b^4} + \left(2H_{12}^s + 4H_{66}^s\right)\frac{m^2n^2\pi^4}{a^2b^2} + A_{55}^s\frac{m^2\pi^2}{a^2} + A_{44}^s\frac{n^2\pi^2}{b^2}
\end{aligned} \tag{41}$$

$$b_1 = \left(F_{11} - \xi F_{12}\right)\frac{m^4\pi^4}{a^4} + \left(\left(F_{11} + F_{12}\right) - \xi\left(F_{12} + F_{22}\right)\right)\frac{m^2n^2\pi^4}{a^2b^2} + \left(F_{12} - \xi F_{22}\right)\frac{n^4\pi^4}{b^4}$$

$$b_2 = \left(F_{11}^s - \xi F_{12}^s\right)\frac{m^4\pi^4}{a^4} + \left(\left(F_{11}^s + F_{12}^s\right) - \xi\left(F_{12}^s + F_{22}^s\right)\right)\frac{m^2n^2\pi^4}{a^2b^2} + \left(F_{12} - \xi F_{22}\right)\frac{n^4\pi^4}{b^4}$$

$$b_3 = (F_{11}^r - \xi F_{12}^r)\frac{m^4\pi^4}{a^4} + \left(\left(F_{11}^r + F_{12}^r\right) - \xi\left(F_{12}^r + F_{22}^r\right)\right)\frac{m^2n^2\pi^4}{a^2b^2} + \left(F_{12} - \xi F_{22}\right)\frac{n^4\pi^4}{b^4}$$

$$c_1 = \left(-\frac{m^2\pi^2}{a^2} + \xi\frac{n^2\pi^2}{b^2}\right)$$

Numerical Examples

Several examples are solved to demonstrate the accuracy and efficiency of the method. In the examples considered, symmetric cross-ply, angle-ply and quasi-isotropic thick rectangular laminates are considered and the following material properties are assumed [29]:

$$E_1/E_2 = 14, G_{12}/E_2 = 0.533, G_{23}/E_2 = 0.323, \nu_{12} = 0.3, \nu_{12} = 0.55$$

Two different cases have been considered in the numerical study: (1) without the effects of curvature terms and (2) with the effect of curvature terms. Note that Case 1 is the conventional consideration of thick plate buckling, which forms the basis of comparison for the case (2). Algorithm used to do the numerical analysis:

A general iterative procedure for obtaining the buckling load N, is as follows:

- The effects of curvature terms are ignored, thus, $c_c = 0$; c_1 and $a_i, i = 1-3$, are calculated. Substitute c_1 and a_i, into matrix in Equation (40). For nontrivial solution of the critical buckling load N_{cr}, the determinant of the matrix in Equation (40) must be equal to zero.
- The effects of curvature terms are included, thus, $c_c = 1$; c_1 and $a_i, b_i, i = 1-3$, are calculated. Substitute c_1 and a_i, b_i, into matrix in Equation (40). For nontrivial solution of the critical buckling load N_{cr}, the determinant of the matrix in Equation (40) must be equal to zero.

- Note that since m, n = 1, 2, . . . ,∞, there is an infinite number of buckling loads N. The critical buckling load N_{cr} is the minimum positive real solution with respect to m and n.

In order to verify the present code, the buckling problem of a simply isotropic square plate (ν = 0.30) under uniaxial compression is studied in Table 1. The numerical results are compared with analytic results of Reddy [34] and strain finite element formulation incorporating a third-order polynomial displacement model results of Nayak [35]. It shows that the present results are compared well with those of the previous works.

Table 1: Comparisons of critical buckling factor $\overline{N} = \overline{N}_{xx} a^2 / \pi^2 D$ for simply supported square isotropic plates under uniaxial compression.

Source	**a/h**				
	5	**10**	**20**	**50**	**100**
Nayak [35]	3.2656	3.7867	3.9445	3.9901	3.9939
Reddy [34]	3.2653	3.7865	3.9443	3.9909	3.9977
Present	3.2653	3.7866	3.9444	3.9910	3.9977

The results of critical buckling load of simply supported square cross-ply laminated composite plates [0°/90°/90°/0°] plate are presented in Tables 2 and 3 and Figs. 1 and 2. In Tables 2 and 3, the critical buckling factor $\left(N_{cr} a^2 / h^3 E_2\right)$ for simply supported square cross-ply laminated composite plates [0°/90°/90°/0°], under biaxial buckling and under in-plane combined tension and compression, respectively for different values of thickness-side ratio (a/h= 5, 10, 15, 20, 25,30). The material and geometry of the square plate considered here are [18]. These results are compared with the results found by Whitney [29] using first-order shear deformation theory. As seen a very good agreement has been achieved between them. Tables 2 and 3 also show that, the critical buckling factor increases with increase in the thickness-side ratio a/h. A comparison of Table 2 with Table 3 shows that the critical buckling load for the plate subjected to compression along x-direction and tension along y-direction, is greater than the corresponding values for the plate under biaxial compression. On the other hand, if the effect of curvature terms is included (Case 2), the buckling factors are always lower than those in Case 1. This appears to be academic, however, as the results in Tables 2 and 3show that the curvature terms have little practical effect on the critical buckling factor for the laminate geometries considered.

Table 2: Comparisons of critical buckling factor $\left(N_{cr}a^2/h^3E_2\right)$ for simply supported square cross-ply laminated composite plates [0°/90°/90°/0°], under biaxial buckling.

a/h	Source			
	FSDT [29] C_c=1	**Present C_c=1**	**FSDT[29] C_c=0**	**Present C_c=0**
5	3.5837	3.9629	3.6706	4.0417
10	5.7459	6.0188	5.8112	6.0853
15	6.5213	6.6801	6.5605	6.7201
20	6.8509	6.9500	6.8758	6.9752
25	7.0163	7.0830	7.0332	7.1000
30	7.1100	7.1576	7.1221	7.1697
CPT	--------	--------	7.3335	7.3335

Table 3: Comparisons of critical buckling factor $\left(N_{cr}a^2/h^3E_2\right)$ for simply supported square cross-ply laminated composite plates [0°/90°/90°/0°], under in-plane combined tension and compression.

a/h	Source			
	FSDT [29] C_c=1	**Present C_c=1**	**FSDT[29] C_c=0**	**Present C_c=0**
5	10.4425	11.5465	10.9050	11.7515
10	26.7192	28.2716	27.4733	28.9051
15	38.0402	39.3715	38.8042	40.1032
20	44.7934	45.8088	45.4372	46.4447
25	48.8479	49.6117	49.3608	50.1229
30	51.3908	51.9739	51.7962	52.8792
CPT	---------	---------	58.3586	58.3586

aMode (1,2)

It should be noted that the present theory involves only two independent variables as against three in the case of first-order shear deformation plate theory [29]. Also, the present theory does not required shear correction factors as in the case of first-order shear deformation plate theory. It can be concluded that the present theory is not only accurate but also efficient in predicting critical buckling load of laminated composite plates.

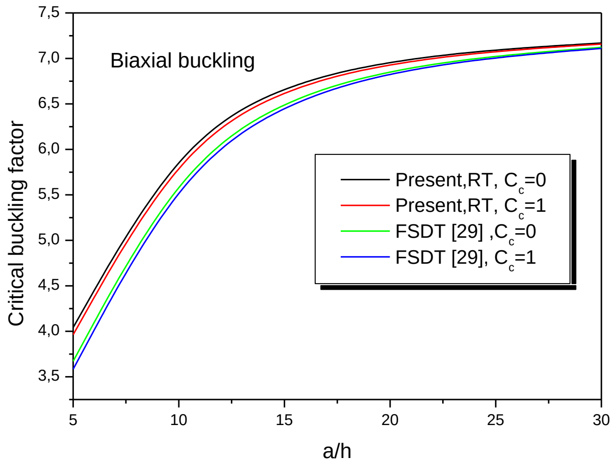

Figure 1: A comparison on buckling responses including curvature effects and effect of shear deformation of simply supported square cross-ply laminated composite plates [0°/90°]$_s$ subjected biaxial compression with those of reported in [29].

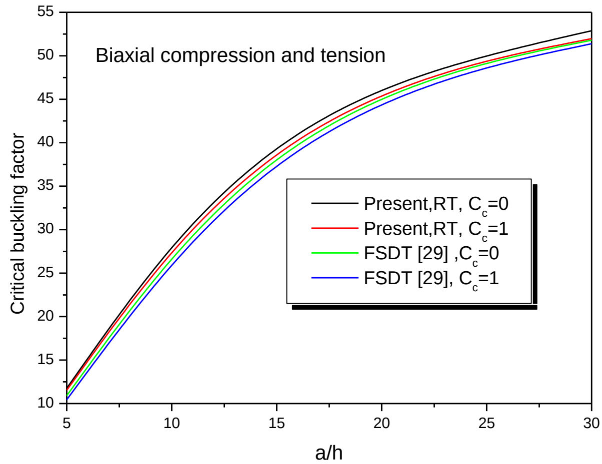

Figure 2: A comparison on buckling responses including curvature effects and effect of shear deformation of simply supported square cross-ply laminated composite plates [0°/90°]$_s$ subjected Biaxial compression and tension with those of reported in [29].

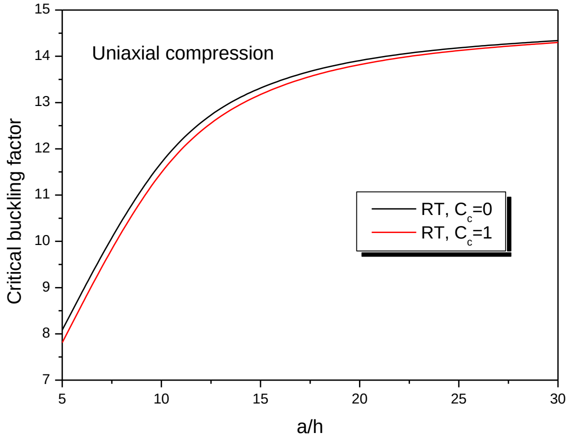

Figure 3: The effect of curvature terms on critical buckling factor of simply supported square plate under uniaxial compression.

Buckling factors are plotted against aspect ratio for plates under uniaxial compression in Figure 3. If only the effect of curvature terms (Case 2) is included, the buckling factors are always lower than those in Case 1.Comparing Figs 1,2 and 3, the responses are very similar, however, the nondimensional critical buckling load of plate under uniaxial compression is greater than that under biaxial compression and less than that under biaxial compression and tension. In addition, the inclusion of curvature terms decreases the buckling factor no matter what loading condition is applied.

Conclusions

In this work, buckling analysis of symmetrically-laminated rectangular plates is investigated. In order to consider the curvature effects, refined two-parameter theory and Navier solution method are used. The present theory has only two unknowns, but it accounts for a parabolic variation of transverse shear strains through the thickness of the plate, without using shear correction factor. Buckling of orthotropic laminates subjected to biaxial inplane loading is investigated. Based on the numerical and graphical results it is concluded that the theory is in good agreement with other higher-order shear deformation theories while predicting the critical buckling response of laminated composite plates. Also, it is observed that, the inclusion of curvature terms decreases the buckling factor no matter what loading condition is applied. In conclusion, it can be said that the proposed theory is accurate and efficient in predicting the buckling responses of symmetrically-laminated rectangular plates with allowance for the effects of higher-order strain terms (curvature terms).

References

[1] S. M. R. Khalili, M. M. Kheirikhah, and K. Malekzadeh Fard. Buckling Analysis of Composite Sandwich Plates with Flexible Core Using Improved High-Order Theory. Mechanics of Advanced Materials and Structures (2015) 22, 233–247

[2] J.S. Moita, A.L.Araújo, V.M.Franco Correia, C.M.Mota Soares, C.A. Mota Soares. Buckling and geometrically nonlinear analysis of sandwich structures. International Journal of Mechanical Sciences 92 (2015) 154–161.

[3] Eugenio Ruocco. Effects of nonlinear strain components on the buckling response of stiffened shear-deformable composite plates. Composites: Part B 69 (2015) 31–43.

[4] G. Raju, Z. Wu, Paul M. Weaver. Buckling and postbuckling of variable angle tow composite plates under in-plane shear loading. International Journal of Solids and Structures 58 (2015) 270–287.

[5] M. Kazemi. A new exact semi-analytical solution for buckling analysis of laminated plates under biaxial compression. Archive of Applied Mechanics (2015).

[6] H. D. Chalak, Anupam Chakrabarti, Abdul Hamid Sheikh, and Mohd. Ashraf Iqbal. Stability Analysis of Laminated Soft Core Sandwich Plates Using Higher Order Zig-Zag Plate Theory. Mechanics of Advanced Materials and Structures (2015) 22, 897–907.

[7] A. Kumar, S. Panda, S. Kumar, D. Chakraborty. Design and analysis of a smart graded fiber-reinforced composite laminated plate. Composite Structures 124 (2015) 176–195.

[8] Chien H. Thai, H. Nguyen-Xuan, S. P. A. Bordas, N. Nguyen-Thanh, and T. Rabczuk. Isogeometric Analysis of Laminated Composite Plates Using the Higher-Order Shear Deformation Theory. Mechanics of Advanced Materials and Structures (2015) 22, 451–469.

[9] Nikunj V. Rachchh, R. K. Misra, D. G. Roychowdhary. Effect of red mud filler on mechanical and buckling characteristics of coir fibre reinforced polymer composite. Iran Polym J (2015) 24:253–265.

[10] Bohlooly M, Mirzavand B .Closed form solutions for buckling and postbuckling analysis of imperfect laminated composite plates with piezoelectric actuators. Composites: Part B 72 (2015) 21–29.

[11] A. Venkatacharia, S. Natarajanb, M. Ganapathia, M. Haboussic. Mechanical buckling of curvilinear fibre composite laminate with material discontinuities and environmental effects. Composite

Structures. Article in presse.
[12] A. Kumar, S. Panda, S. Kumar, D. Chakraborty. A design of laminated composite plates using graded orthotropic fiber-reinforced composite plies. Composites Part B 79 (2015) 476-493.
[13] Timoshenko SP, Gere JM. Theory of elastic stability. McGraw-Hill; 1961.
[14] Leissa AW. Conditions for laminated plates to remain flat under inplane loading. Compos Struct 1986; 6:261–70.
[15] Qatu MS, Leissa AW. Buckling or transverse deflections of unsymmetrically laminated plates subjected to in-plane loads. AIAA J 1993; 31(1):189–94.
[16] E. Reissner, The effect of transverse shear deformation on the bending of elastic plates, J. Appl. Mech. 12 (2) (1945) 69–72.
[17] R.D. Mindlin, Influence of rotatory inertia and shear on flexural motions of isotropic, elastic plates, J. Appl. Mech. 18 (1) (1951) 31–38.
[18] Reddy JN. A simple higher-order theory for laminated composite plates. J Appl Mech 1984; 51:745–52.
[19] Touratier M. An efficient standard plate theory. Int J Eng Sci 1991; 29(8):901–16.
[20] Soldatos KP. A transverse shear deformation theory for homogeneous monoclinic plates. Acta Mech 1992; 94:195–200.
[21] Aydogdu M. A new shear deformation theory for laminated composite plates. Compos Struct 2009; 89:94–101.
[22] Senthilnathan NR, Lim SP, Lee KH. Buckling of shear-deformable plates. AIAA J 1987; 25: 1268–71.
[23] Shimpi RP. Refined plate theory and its variants. AIAA J 2002; 40:137–46.
[24] Shimpi, R. P. and Patel, H. G. A two-variable refined plate theory for orthotropic plate analysis. International Journal of Solids and Structures, 43(22), 6783–6799 (2006)
[25] Shimpi, R. P. and Patel, H. G. Free vibrations of plate using two-variable refined plate theory. Journal of Sound and Vibration, 296(4-5), 979–999 (2006)
[26] Reddy JN. Mechanics of laminated composite plates: theory and analysis. Boca Raton: CRC Press; 1997.
[27] Jones RM. Mechanics of composite materials. Hemisphere Publishing Corporation; 1975.
[28] Dawe, D. J. and Roufaeil, O. L., Buckling of rectangular Mindlin plates, Computers and Structures, 15 (1982) 461-71.
[29] Whitney JM. Curvature Effects in the Buckling of Symmetrically-Laminated Rectangular Plates with Transverse Shear Deformation. Composite Structures 8 (1987) 85-103.
[30] Whitney, J. M. and Pagano, N. J., Shear deformation in heterogeneous

anisotropic plates, Trans. ASME, J. App. Mech., 37 (1970) 1031-6.
[31] K. M. Liew, Y. Xiang and S. Kitipornchai. Navier's solution for laminated plate buckling with prebuckling in-plane deformation. International Journal of Solids and Structures Vol. 33, No. 13, pp. 1921-1937, 1996.
[32] Leissa A W, Ayoub E F. Vibration and buckling of simply supported rectangular plate subjected to a pair of in-plane concentrated forces. J Sound Vibr 1988; 127(1):155–71.
[33] Eisenberger M, Alexandrov A. Buckling loads for variable cross section members with variable axial forces. Int J Solids Struct 1991; 27:135–43.
[34] J.N. Reddy, N.D. Phan, Stability and vibration of isotropic, orthotropic and laminated plates according to a higher-order shear deformation theory, Journal of Sound and Vibration 98 (1985) 157–170.
[35] A.K. Nayak, S.S.J. Moy, R.A. Shenoi. A higher order finite element theory for buckling and vibration analysis of initially stressed composite sandwich plates. Journal of Sound and Vibration 286 (2005) 763–780.

Earth Observation Micro-satellite Design Optimization Using Satellite Simulator

Robertus Heru Triharjanto
Ridanto Eko Poetro
Hari Muhammad
Faculty of Mechanical and Aerospace Engineering
Institut Teknologi Bandung
hari@ae.itb.ac.id

Soewarto Hardhienata
National Institute for Aeronautics and Space (LAPAN)

ABSTRACT

With the more demanding performances and more limited resources available, obtaining an optimized engineering design is the necesity for design engineers. Therefore, the objective of the research is to develop method for optimizing satellite design. The satellite design phase concerned in the research is in detail design, which mean that the choices for basic configurations of the satellite has been determined. The design case is Earth observation microsatellite, with objective of the optimization is the minimum power consumption from the attitude control subsystem. Doing so, the payload duty cycle, and therefore, the image coverage can be increased. In order to perform the optimization that involve attitude control subsystem, a high-fidelity modeling tool, which in this context means the attitude dynamics module of the satellite simulator used. The module calculate the satellite orientation at any time, and the torque required to perform the camera pointing operation, which is the base for power consumption calculation. The result shows that the simulator can support the selection of the satellite optimal configuration by providing evidence of minimum power consumption. It is also find that due to full acces level, the self-made simulator as used in the research has good potential to be used in the optimization case with search algorithm.

Keywords: *Design Optimization, Earth Observation Micro-satellite, Satellite Simulator*

ISSN 1823- 5514

Received for review: 2016-01-21
Accepted for publication: 2016-10-27
Published: 2016-12-19

Introduction

Previous Satellite Design Optimizations

Satellite design optimization using low fidelity design model has been performed, among others, by Hassan [1], Tan [2], Jafarsalehi [3], and Wang [4]. Hassan [1] performed optimization for telecommunication satellite weight by varying the types satellite components, using Genetic Algorithm. The design constraint is the launcher's weight and dimension envelope. The best configuration found in this satellite design is a telecommunication satellite that use Si solar panel, NiH_2 bateries, pasive thermal system, plasma propulsion, and wave tube amplifiers for all of transponders. Tan [2] performed design optimisation for small (1000 kg) class Earth observation satellite with objectives highest resolution and maximum coverage. The design constraint is the payload's size, weight, and power consumption, as well as the satellite's weight and size, based on the launcher's envelope. The variables are the ratio of propellant, structure, power subsystem, attitude control components, and orbit height, and collaborative optimization method is used to find the best configuration.

Jafarsalehi [3] performed optimisation for small (1000 kg) class Earth observation satellite design with objective of highest resolution, and design constrains of launch envelope and groundstation visibility. The variables include orbit height, propulsion, structure, and solar panels, and the optimum search is done by Genetic Algorithm. Wang [4] also optimized Earth observation satellite design with objectives of highest resolution and maximum coverage, with constrain of launch envelope. The design models is aranged web-like structure connected by their coupled variables, called all-at-once (AAO) model, and solved with collaborative method. The variables include orbit height, propulsion, structure, and power subsystem.

Satellite design optimization using high fidelity design model has also been done in subsystem level by Boudjemai [5], Zhang [6], and Kim [7]. In satellite system level design, such work has been done by Wu [8] and Hwang [9]. Boudjemai [5] used finite element analysis software and Genetic Algorithm to optimize the structure of the satellite automatically. Zhang [6] used solid modeling software and Genetic Algorithm to automatically design the satellite components placement, for the required satellite's center of gravity and inertia. Kim [7] used own-built satellite attitude control simulator and Genetic Algorithm to optimize the attitude control system of KITSAT-3 micro-satellite. The resulted design is the KITSAT-3 attitude control with minimum response time.

Wu [8] used comercially available concurrent engineering software iSIGHT, that integrate finite element for the high fidelity model of satellite structure, and Matlab for designing the satellite attitude control, power suply, and thermal subsystems. The optimum solution is solved using collaborative optimization method, and the aim of the design was to optimize the satellite performance at system level, i.e. image resolution and swath/ coverage.

Hwang [9] developed satellite design models in AAO method, with one of the node asa high-fidelity model, i.e. the satellite orbit and attitude propagator. The propagator also calculates the sun angle with respect to the satellite solar panel, so that the electrical power supplied to the satellite can be calculated. Determining the ground station location, the propagator can calculate the satellite downlink datarate, which is a function of the angle between groundstation line of sight with the satellite antenna. The optimization is done using gradient method, to get the best satellite solar panel and antenna angles for maximum amount of data downlinked in 1 month operation.

Research Objectives and Methods

System level optimization involving high-fidelity design model may become the future in satellite design. However, the approach using comercially available sofwares is considered expensive for micro-satellite developer. Meanwhile, the AAO approach requires high ability in mathematics and programing. Therefore, the research proposed the method of optimizing satellite design in two steps, i.e. at system level, using low fidelity design model to get the satellite basic configurations, and then continued using high fidelity model to further optimize the design.

In this research, the system design for the intended micro-satellite has been done [10], as well as the system level multi-objectives optimization [11]. The optimization yield 5 possible design options (pareto), in which, further selection may be performed to get the best design. Several high-fidelity models can be selected, such as finite element model for the design of structure subsystem as in [8], to minimize weight, or orbit propagator with Sun model for the design of power subsystem as in [9], to maximize operation duration.

Attitude control system is crucial in Earth observation satellite, since it needs stable and accurate pointing to produce good quality images. In microsatellite, the limited power supply capacity causes the operation of attitude control system limited only during imaging operation. The system design requirement defined that the imaging operation has to bedone at minimum 30% of the orbit time [10]. Therefore, during the rest of the time, the satellite can be set at hibernation mode, in which the attitude control system can be switched-off.

A satellite orbit and attitude dynamics simulator might calculate, in high-fidelity, the power consumption for satellite attitude control. In this research, the variables is satellite moment of inertia, which is different for each configuration, and the satellite control operation modes. The objective of the optimization is to find satellite configuration with potential of highest satellite imaging operation duration due to its power availability.

The Earth Observation Satellite Configuration

The satellite mission is to obtained images of Earth surface with the highest quality possible (in object recoqnition), as much as possible. These means a satellite that could accomodate imaging system with highest resolution and widest swath.

The typical micro-satellite design constraints are the maximum dimension of 60x60x80 cm, and maximum weight of 100 kg. The satellite configuration chosen is a box-shaped satellite for maximizing base area utilization, with middle plate to allocate te satellite components. The sattelite imaging payload are placed on the base, so that the length of the lens could be utilized the full height of the satelite. The satellite has body-mounted solar panels occupying the intire four lateral sides. Another design constraint is the maximum downlink datarate that the satellite could perform is 200 Mbps, and the satellite could only perform direct downlink operation mode.

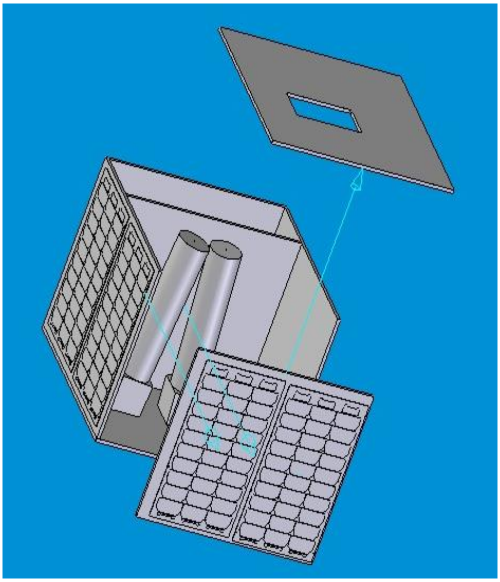

Figure 1: The micro-satellite structure showing its solar panels and 2 camera imagers

The pareto result for optimizing the satellie configuration with respect to highestresolution and maximum image swath is the 5 configurations in table 1 [11].

To accomodate the satellite pointing requirement, it is equiped with 3 reaction wheels and 3 asociated gyros, placed in its 3-axis. It is also equiped with star sensor for absolute pointing knowledge. The satellite's power budget anaylsis from the low fidelity model, i.e. statistics of LAPAN's satellite, shows that the attitude control system (ACS) consumed 29% of the total power consumption [10]. Such consumption is the 2nd highest after the consumption of the satellite's data transmision system. Therefore, the impact from optimizing the ACS power consumption will be significant for the satellite total performance.

Tabel 1 : Optimal satellite configuration recomended by MOPSO

No	Resolution (m)	Swath (km)	Power production (Whr)	Dimension (cm)	Weight (kg)
1	6	50	144,1	60 x 60 x 58,6	80,5
2	7	75	137,6	60 x 60 x 55,9	76,4
3	11	150	155,4	60 x 60 x 63,2	85,5
4	12	175	144,5	60 x 60 x 58,8	80,4
5	13	200	135,3	60 x 60 x 55,0	76,0

Attitude Control Power Optimization

The Satellite Dynamic Simulator

LAPAN-ITB satellite dynamic simulator consist of 4 modules, as illustrated in Figure 2. The first module of the simulator is an orbit propagator. Given the orbit parameters and initial position, the module will calculate the satellite position at any time point. Since no propulsion system installed in the satellite, orbit manuver is not accomodated in the module.

The second module is a space environment model. Since the simulation is mainly concern in attitude control, the environment to be developed means magnetic flux that the satellite may experience at any position given by the orbit propagator module.

The third module is a satellite model, which simulate the operation status of its 3 reaction wheels and 3 magnetic torquers, based on attitude control mode selected. The known attitude and angular rate knowledge simulated star sensor and gyros in the satellite, The module also calculates the power consumption of the attitude control subsystem.

The fourth module is attitude dynamics, which calculate the new attitude (angles) based on the attitude control components operation. The input of the module includes satellite moment of inertia. For operation that does not involved external torque (magnetic torque), the new attitude is fedback to the satellite module, or else it feedback to the environment module, before brought to satellite module.

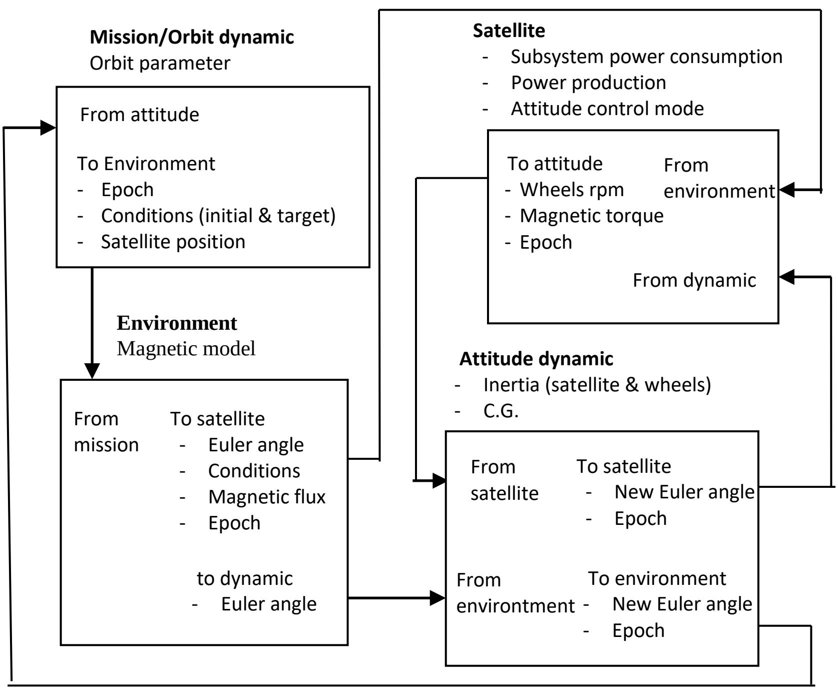

Figure 2: The satellite dynamic simulator schematics

For the case performed in this research, i.e. no external torque, the governing equation of the attitude dynamics for satellite with 3 orthogonal reaction wheels is :

$$\begin{bmatrix} I_{xx} & J_{xy} & J_{xz} \\ J_{xy} & I_{yy} & J_{yz} \\ J_{xz} & J_{yz} & I_{zz} \end{bmatrix}_S \begin{bmatrix} \dot{\omega}_x^s(t) \\ \dot{\omega}_y^s(t) \\ \dot{\omega}_z^s(t) \end{bmatrix} = \begin{bmatrix} \omega_x^s(t) \\ \omega_y^s(t) \\ \omega_z^s(t) \end{bmatrix} \times \left(\begin{bmatrix} I_{xx} & J_{xy} & J_{xz} \\ J_{xy} & I_{yy} & J_{yz} \\ J_{xz} & J_{yz} & J_{zz} \end{bmatrix} \begin{bmatrix} \omega_x^s(t) \\ \omega_y^s(t) \\ \omega_z^s(t) \end{bmatrix} + \begin{bmatrix} I_{rw} & 0 & 0 \\ 0 & I_{rw} & 0 \\ 0 & 0 & I_{rw} \end{bmatrix} \begin{bmatrix} \omega_x^{rw}(t) \\ \omega_y^{rw}(t) \\ \omega_z^{rw}(t) \end{bmatrix} \right)_S \quad (1)$$

Superscipts in the angular rate (ω) denote the rotating bodies; 's' for satellite and 'rw' for reaction wheel.

The implementation of the simulator is done in Matlab-Simulink. The validation test of the attitude dynamics part of the simulator was done on [12]. The validation, among others, involved varying the inertia of the satellite starting from no cross product inertia (cylindrical type) to significantly high percentage of cross product inertia, and running 1 reaction wheel in open loop mode. The tests show phenomena as govern by Equation (1), which no nutation occurs in cylindrical type inertia and grow as percentage of cross product inertia increase.

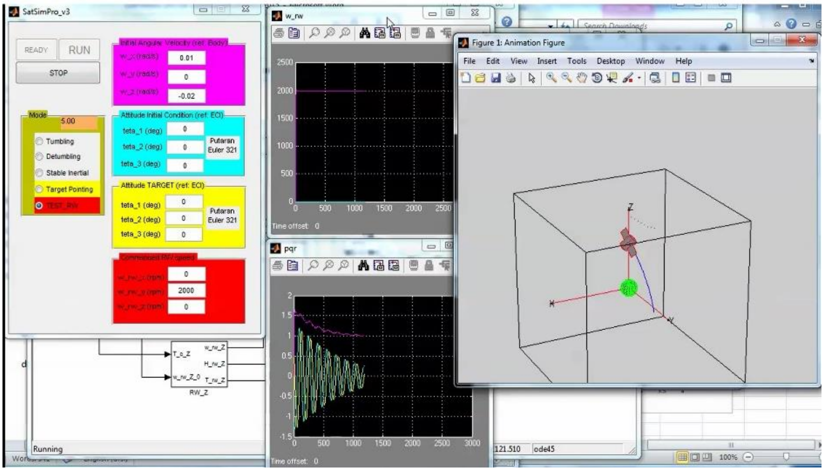

Figure 3: The satellite simulator showing case of angular momentum absorption

The Simulated Cases

The input variables in the attitude dynamic simulation, among other, is the satellite inertia. Based on the satellite mass and dimension in Table 1, the moment of inertia of the satellite is calculated, as listed in Table 2. The cross product inertia is set for 2% of the major axis inertia as the typical configuration in LAPAN's micro-satellite [13]. Other input is the inertia of the satellite reaction wheels, which is selected to be 0,0049 kg.m^2.

Table 2: Moments of inertia of the satellite preliminary design optimal configuration (kg.m^2)

Configuration	Ixx	Iyy	Izz	Jxy/Jxz/Jyz
1	4,72	4,72	4,83	0,14
2	4,28	4,28	4,58	0,13
3	5,41	5,41	5,13	0,16
4	4,73	4,73	4,82	0,14
5	4,20	4,20	4,56	0,13

The reaction wheel's power consumptions is modeled by semi-empiric formulation:

$$W_i = \int_0^{t_a} \left[\frac{30}{0.02} I_{rw} \dot{\omega}_i^{rw}(t) + \frac{6}{6000} \omega_i^{rw}(t)\right] dt \qquad (2)$$

The power consumption depends on the torque given to accelerate, and to maintain the wheel's rotation. The wheel's control electronics modeled with simple PID controler. The constants in Equation (2) use the typical value of microsatellite reaction wheels, which at maximum power consumpton of 30 W, may give 0.02 Nm torque to the wheel [13]. The power required to overcome the friction in the wheel, or to maintain the wheel's speed, is modeled to be propotional to the speed. The typical microsatellite reaction wheel has maximum speed of 6000 rpm, which the power needed to overcome the wheel's friction at such speed is assumed to be 6 W.

Since the satellite switched-off its attitude control system during hibernation mode, the attitude manuver required to conduct imaging operation started with detumbling mode. As shown in Figure 4, during hibernation mode, the satellite may arbitrarily rotate in its 3 axis (tumbling). The mode is activating the satellite's 3 reaction wheels (closed-loop with with the gyros) to stop the rotation in all axis.

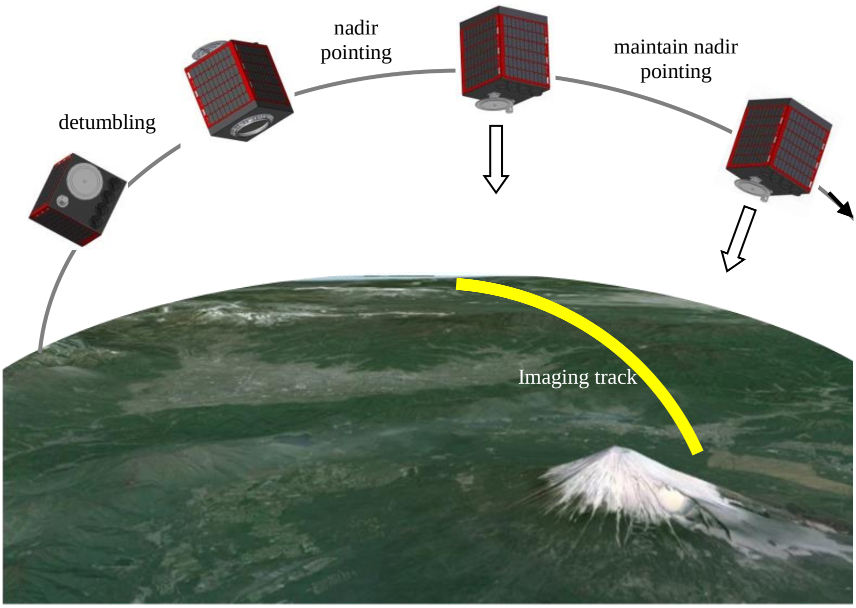

Figure 4: Attitude manuver for imaging operation

At the end of detumbling manuver, the satellite camera might point to any arbitrary direction as illustrated in Figure 3. Therefeore, the next manuver is to make the satellite's camera points to nadir. Here, the simulation assumed the satellite has to performed large angles rotation, i.e. 120^o in X (roll) axis and then 80^o in Z (yaw) axis.

The last manuver in the imaging operation is maintaining nadir pointing, so that the camera can make highest resolution images. The manuver is to rotate the satellite of 0.06 deg/s in Y axis.

Results and Discussions

Detumbling Manuver

The initial angular velocity of the satellite in the detumbling manuver is assumed to be 1.1 deg/s at X axis, 1.7 deg/s at Y axis, and 2.8 deg/s at Z axis. In real satellite operation, such number is considered high for the operation mode selected (need angular momentum dumping). However, the purpose of this exercise is to show significant differences in the reaction wheels responses. The results from detumbling simulation, i.e. satellite angular rate and reaction wheels rpm, history are ploted in Figure 4 and Figure 5.

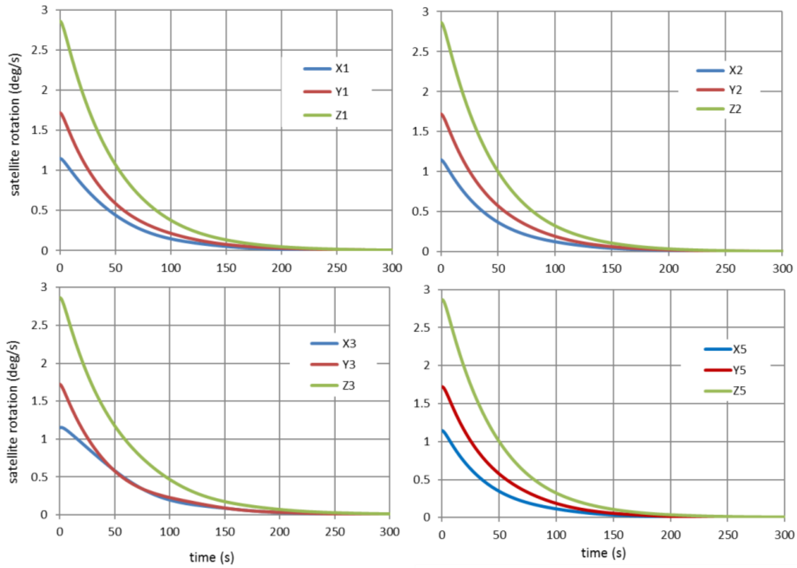

Figure 4: Satellite angular rate on detumbling manuver for configuration 1, 2, 3, and 5

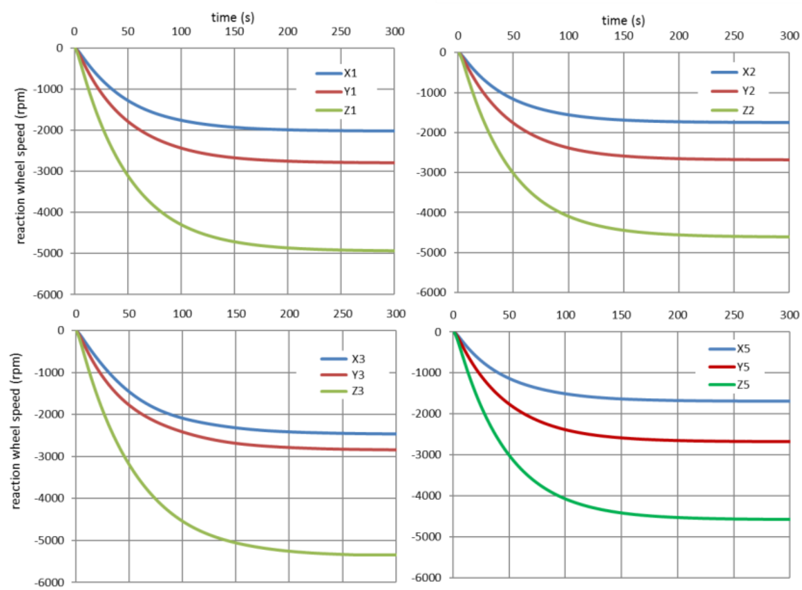

Figure 5: Reaction wheel speed in detumbling manuver for configuration 1, 2, 3, and 5

From the detumbling simulation, it is shown that all satellite configuration can complete the manuver in less than 250 s (configuration 5 not shown for display efficiency). Figure 4 show that the satellites angular rate history in Y axis is exactly the same for all configurations. Meanwhile in X and Z axis, the rate for satellite configuration 2 and 5 decay the faster, and satellite configuration 3 decay the slowest.

Figure 5 show that satellite configuration 5, which has the smallest inertia out of the four confguration displayed, is shown to require the smallest reaction wheel rpm to stop the satellite rotation. Meanwhile, configuration 3, which has the largest inertia out of the four, is shown to require the highest reaction wheel rpm to stop the satellite rotations.

The simulated attitude control power consumption (Figure 6) shows that the power consumption for configuration 2 and 5 is almost similar and the lowest. The highest power consumption is in configuration 3. This trend confirms the inertia comparison of each satellite configuration (Table 2).

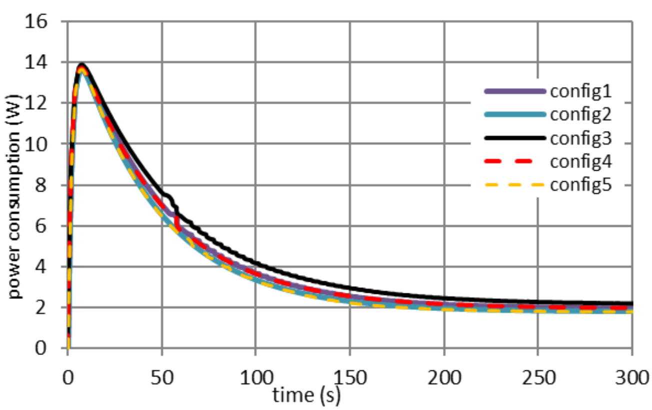

Figure 6: Attitude control power consumption in detumbling manuver

Nadir Pointing Manuver

The results from nadir pointing attitude manuver simulation are shown in Figure 7 to 9. The rotation history shows that all configurations can finish manuver at 200 seconds (the initial angles is the last pointing given by last manuver). The rotation in Y axis is not commanded but perfomed by the system due to transfer of angular momentum by the satellite cross product inertia. Figure 7 shows that satellite configuration 2 took less undershoot angle in X and Y axis at time 150 seconds. Other than that, the angle profiles are very similar.

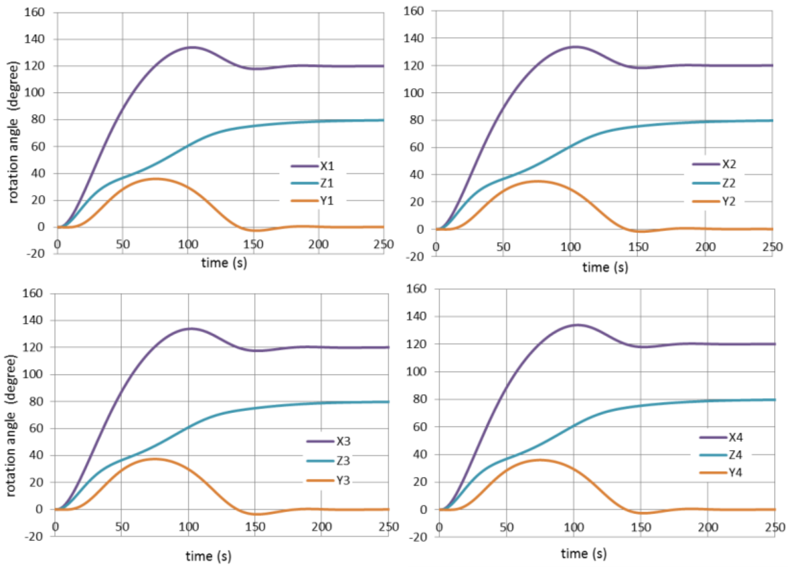

Figure 7: Satellite angle on nadir pointing manuver for configuration 1, 2, 3 and 4

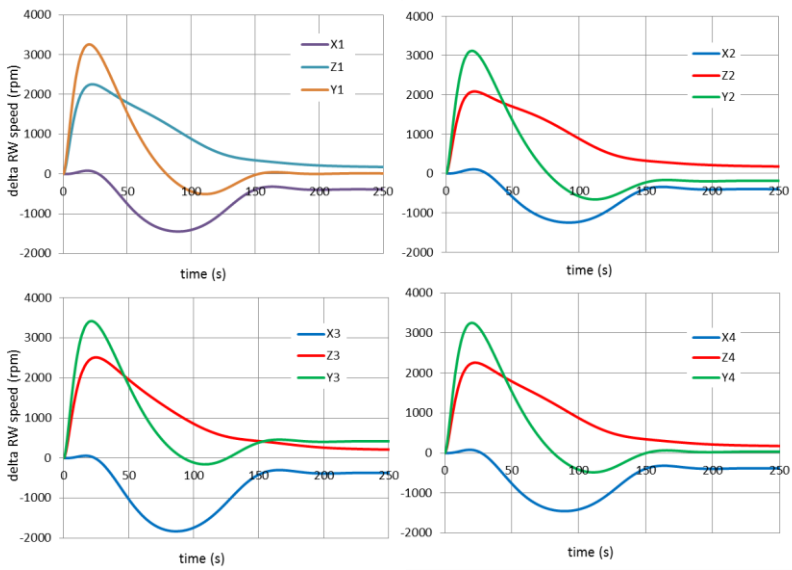

Figure 8: Reaction wheel speed in nadir pointing manuver for configuration 1, 2, 3, and 4

Even though the satellites angle history look very similar, the reaction wheels performed quite different for each configuration. Figure 8 shows the reaction wheels speed that needs to be added from the wheels'speed at the end of detumbling manuver. Even though configuration 2 need the least Y wheel rpm during the 1st 75 seconds of attitude maneuver, configuration 1 and 4 need the least rpm afterwards (almost zero after 150 second). The figure also shows satellite configuration 2 need the least X wheel rpm to perform the compensation rotational. Satellite configuration 3 need the most wheel rpm to perform the maneuver. The configuration also needs positive rpm in Y axis reaction wheel starting at 120 second until steady state.

Figure 9 shows the additional power consumption (from the last manuver state) needed by the attitude control subsystem to perform the nadir pointing rotations. The sudden high power consumption in the 1st 20 seconds of the manuver is to built-up necesary torque to rotate the reaction wheels at the begining of the manuver. The consumption, however, still below the power limit defined for the attitude control system, and therefore, confirm the attitude control system design is feasible. The plot shows that configuration 3 need the most power for the manuver.

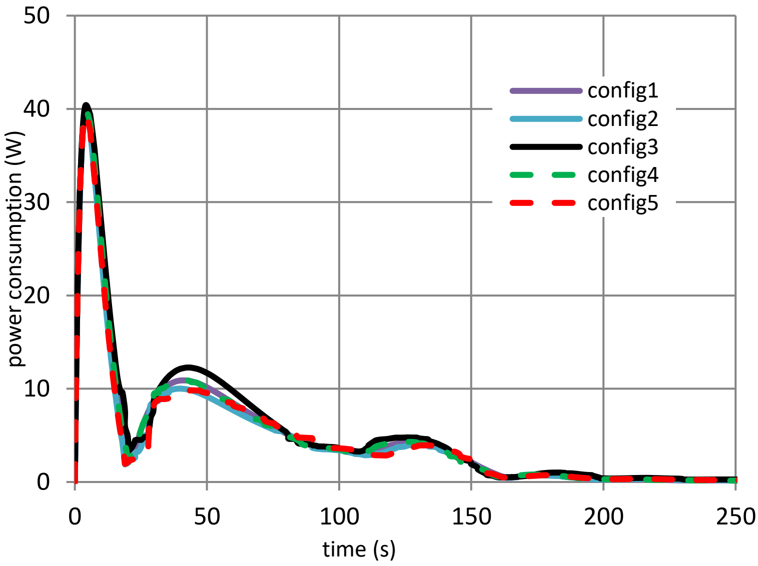

Figure 9: Attitude control power consumption in nadir pointing manuver

Nadir Keeping Manuver

In order to keep nadir pointing during imaging operation, the satellite only neeeds to increase (assuming a polar orbiting satellite flying from North to

South) the rotation rate of Y axis reaction wheel's by about 10 rpm. Therefore, power consumption differences are not significant for each configuration, and can be regarded as the power needed to maintain the satellite wheels's rpm from the previous manuver (detumbling). The imaging operation is assumed to be done for 10 minutes.

Table 3: Power consumption of the satellite attitude manuver (Wh)

Mode	Config 1	Config 2	Config 3	Config 4	Config 5
Detumbling	0,292	0,296	0,343	0,315	0,292
Nadir pointing	0,449	0,415	0,489	0,446	0,417
Nadir keeping	0,338	0,311	0,378	0,338	0,305
Total	1,079	1,022	1,21	1,099	1,014

Table 3 shows the power consumption (in Watt-hour) from each attitude manuver mode of the for satellite imaging. The table show that the lowest power consumption is by satellite configuration 5, i.e. satellite with image resolution of 13 m and swath of 200 km.

From Table 1, it is known that configuration 5 also has the lowest power production capacity. Therefore, using configuration 5 as the baseline, the increase in the power consumption and production are measured, as tabulated in table 4. The table show that in configuration 4 and 5, the percentage increase in the power consumption in less than the increase in power production, due to the larger area available for solar panel. Configuration 2, however, show different trend where the increase in power consumption is less than those of production. Therefore, 2nd best in power consideration is satellite configuration number 2, which means should higher resolution is desired for some reason, the choice is the satellite with image resolution of 7 m and swath of 75 km.

Table 4: Power production and consumption comparison

% higher	Config 1	Config 2	Config 3	Config 4	Config 5
Consumption	6,4	0,8	19,3	8,4	0,0
Production	6,5	1,7	14,9	6,8	0,0

The simulations show that the total time needed to prepare imaging operation (achieve nadir pointing) is 450 seconds or 7.5 minutes. The power consumption plots (Figure 6 and 9) show that the system can be further optimizedto have shorter transient time, simply by increasing the gain in the PID. Such changes will not change the total enegry consumption but will increase wattage consumption profile. With the large margin currently exist in the wheel's power consumption (maxmium 30 W per wheel), the trasient time is potentially be reduced in half.

In the case when attitude control system design feasibility is in corncern, for example exceeding power limit to get the desired transient time etc., the attitude control hardware parameter in the simulator can be easily modified. Therefore, if needed, the design variables can be extended into choices of attitude control hardware parameter.

Since the simulator is built in Matlab environment in academic institutions, it can be easily adapted for the implementation of optimizing algorithm in the design process (not restricted by commercial propietary).

Conclusions and Further Work

LAPAN-ITB's satellite simulator, in this case its attitude dynamics module, has been shown to be an effective tools in design optimization. It is able to provide support for the best configuration decision making out of 5 configurations obtained from multi-objectives pareto. The effectiveness of the simulator as optimizing tools is even higher in the case where large input parameter variations, in this case is moment inertia, exist. For example the case chosing between of deployable or body mounted solar panel or between solid plate and iso grid structure, where the soution may not be intuitive.

The satellite simulator has been shown to be potentially useful for sizing the attitude control components and deciding on control parameters/ algorithm. Therefore, using the simulator, such parameter may be included for the future research in satellite design optimization.

Since the simulator can be easily adapted, future research may involve the implementing optimization algorithm in the simulator's code. Potential collaborators are welcomed.

Acknowledgement

The authors wish to thank Mr. Satriya Utama of National Institute for Aeronautics & Space (LAPAN) on the discussion in the modification of the satellite simulator. The authors also wish to thanks Faculty of Mechanical and Aerospace Engineering, ITB for funding this research.

References

[1] Hassan, R. A., Crossley, W. A.; "Multi-Objective Optimization of Communication Satellites with Two-Branch Tournament Genetic Algorithm", Journal of Spacecraft and Rockets 40(2), 266-272 (2003)

[2] Tan, C.L., Pang, B.J., Zhang, L.Y., Huang, H.; "Multi-disciplinary

Optimization in Earth Observation Satellite Main Parameters"; Journal of Beijing University of Aeronautics and Astronautics 34; (2008)

[3] Jafarsalehi, A., Zadeh, P. M., Mirshams, M.; "Collaborative Optimization of Remote Sensing Small Satellite Mission Using Genetic Algorithms"; IJST, Transactions of Mechanical Engineering 36 (M2), 117-128(2012)

[4] Wang, X. H., Li, R. J., Xia, R. W.; "Comparison of MDO Methods for an Earth Observation Satellite"; Proceeding 7th Asian-Pacific Conference on Aerospace Technology and Science (2013)

[5] Boudjemai, A.; Bouanane, M.H.; Merad, L.; Mohammed, A.M.; "Small Satellite Structural Optimization using Genetic Algorithm Approach"; Proceeding 3rd International Conference on Recent Advances in Space Technologies, 398-406 (2007)

[6] Zhang, B., Teng,H., Shi, Y.; "Layout Optimization of Satellite Module Using Soft Computing Techniques"; Applied Soft Computing 8, 507–521 (2008)

[7] Kim, B.J.,Lee, H., Choi, S.D.; "Three-axis Reaction Wheel Attitude Control System for KITSAT-3 Microsatellite"; Space Technology 16(5-6), 291-296(1996)

[8] Wu, W., Huang, H., Chen, S., Wu, B.; "Satellite Multidisciplinary Design Optimization with a High-Fidelity Model"; Journal of Spacecraft and Rockets 50 (2), (2013)

[9] Hwang, J. T., Lee, D. Y., Cutler, J. W., Martins, J. R.; "Large-Scale Multidisciplinary Optimization of a Small Satellites Design and Operation"; Journal of Spacecraft and Rockets, (2014)

[10] R.H. Triharjanto, R.E. Poetro, H. Muhammad, "Sensitivity Analysis on Preliminary Design ofEarth Observation Microsatellite (AnalisaSensitivitas pada Desain Awal Satelit Mikro Pengamat Bumi)"; Jurnal Teknologi Dirgantara 11 (1), 13-21(2013)

[11] R.H. Triharjanto; R.E. Poetro; S. Hardhientana,"Multi-objectives Optimization of Earth Observation Micro-Satellite Design Using Particle Swarm", Proceedings of IEEE International Conference Aerospace Remote Sensing, Jogjakarta, Indonesia (2014)

[12] R.H. Triharjanto; M.S, Nur Ubay; S. Utama; R.E. Poetro,"Evaluation of Attitude Dynamic Module on LAPAN-ITB Micro-Satellite Simulator", submitted for IEEE International Conference Aerospace Remote Sensing, Bali, Indonesia (2015)

[13] R.H.,Triharjanto, M. Mukhayadi, W. Hasbi; "LAPAN-TUBSAT System Budget"; Chapter 4 of "LAPAN-TUBSAT : First Indonesian Microsatellite", LAPAN (2007)

Journal of Mechanical Engineering *Vol 13(2), 77-97, 2016*

The Influence of Piston Bowl Geometries on In-Cylinder Air Flow in a Direct-Injection (DI) Diesel Engine for Biodiesel Operation

S. Jaichandar
Department of Automobile Engineering,
VelTech Dr RR & Dr SR Technical University,
Chennai, India
Email: jaisriram18@yahoo.com

E. James Gunasekaran
Department of Mechanical Engineering, Annamalai University,
Chidambaram, Tamil Nadu, India
Email: jamesgunasekaran@gmail.com

A. Gunabalan
Turbo Energy Private Limited, Chennai, India
Email:gunmit@gmail.com

ABSTRACT

Thermal efficiency improvement, fuel consumption and pollutant emissions reduction from biodiesel fueled engines are critical requirements in engine research. In order to achieve these, a rapid and better air-fuel mixing condition is desired. The mixing quality of biodiesel with air can be improved by selecting the best engine design particularly combustion chamber design and injection system parameters. The present work investigates the effect of varying the piston bowl geometry on the air flow characteristics such as swirl velocity, Swirl Ratio (SR), and Turbulent Kinetic Energy (TKE) inside the engine cylinder. The piston's bowl geometry was modified into several configurations that include Shallow depth combustion chamber (SCC), Toroidal combustion chamber (TCC), Shallow depth reentrant combustion chamber (SRCC) and Toroidal re-entrant combustion chamber (TRCC) from the standard Hemispherical combustion chamber (HCC), without altering the compression ratio of the engine. A commercially available CFD code STAR-CD was used to analyze the in-cylinder flow at different conditions.

ISSN 1823- 5514

Received for review: 2016-01-27
Accepted for publication: 2016-06-10
Published: 2016-12-19

Flow conditions inside the cylinder were predicted by solving momentum, continuity and energy equations. The results confirmed that the piston bowl geometry had little influence on the in-cylinder flow during the intake stroke and the first part of compression stroke i.e. up to 300°after suction TDC. However, the piston bowl geometry plays a significant role in the latter stage of the compression stroke i.e. beyond 300°after suction TDC to compression TDC. The intensity of maximum swirl velocity at the end of compression stroke for TRCC was observed higher as 18.95 m/s and a strong recirculation was observed due to the geometry. Compared to baseline HCC the TRCC had higher, maximum swirl ratio and turbulent kinetic energy by about 28% and 2.14 times respectively. From the analysis of results, it was found that TRCC configuration gives better in-cylinder flows.

Keywords: *Diesel Engine, Combustion Chamber, Swirl Velocity, Swirl Ratio, Turbulent Kinetic Energy.*

Introduction

The main purpose of an internal combustion engine is to exhibit good performance while meeting the stringent emission standards. In order to meet those requirements, the outcomes of the combustion process are very important in internal combustion engines [1]. In-cylinder fluid dynamics in DI diesel engines plays a vital role for efficient combustion process [2]-[4]. It has been widely known that the engine performance and emissions of a compression ignition engine are dependent on the fuel vapour distribution in the cylinder. The efficiency of a DI diesel engine depends on the mixture preparation and its distribution inside the combustion chamber [5]. This phenomenon is based on the interaction of the in-cylinder air motion such as swirl, squish, tumble and turbulence and the spray characteristics from the high pressure injector. Hence, the shape of the combustion chamber geometry, the location of the injector, type of injector, air motion and fuel delivery characteristics become important factors for study [6].

The piston bowl geometry, location of injector, cylinder geometry and injection characteristics are important criteria in the design of DI diesel engines [2, 7]. The fuel evaporation and mixing processes are strongly influenced by the turbulent nature of the in-cylinder flows. In order to have better mixing, swirl is generated during the compression stroke as a result of combustion chamber geometry [8]. In-cylinder flow characteristics at the time of fuel injection and subsequent interactions with fuel sprays and combustion are the fundamental considerations for the engine performance and exhaust emissions of a diesel engine. Computational fluid dynamics (CFD) is a powerful tool for the computation of fluid flow in complex geometries. The calculation of the flow field in the complex combustion chamber geometry is a great challenge. With the help of CFD, results can be used for the optimization of the combustion chamber geometry regarding the improvement of efficiency and the reduction of emissions in existing engine and can be used for new developments.

The aim of this work is to study the effect of combustion geometry on air flow and thereby to improve the performance of a four stroke, single cylinder 5.2 kW engine running at 1500 rpm for biodiesel operation. Hence, virtual prototypes of the piston with five different combustion chamber geometries were created and analyzed using CFD software package.

Motivation

The high fuel efficiency of diesel engines has led to their use in many fields including transportation, electrical power generation and agricultural machinery [9, 10]. However, the rapid depletion of fossil fuel with increased environmental concern has increased interest and efforts to produce an alternative to diesel [11]-[14]. Use of biodiesel as an alternative fuel can contribute significantly towards the twin problem of fuel crises and environmental pollution. Researchers [15, 16] have shown that biodiesel fuel exhibits physico-chemical properties which are similar or some even better than to those of diesel and hence can be used in diesel engines. However, certain properties of biodiesel such as viscosity, calorific value, density and volatility differ from diesel.

The high viscosity of biodiesel affects injection characteristics. Although transesterification reduces viscosity of biodiesel [17, 18], the viscosity of biodiesel was found to be 50 to 80% higher than diesel [19]. The poor atomization, insufficient in-cylinder air motion and low volatility of biodiesel lead to difficulty in the air-fuel mixing. Inadequate air-biodiesel mixing and sluggish evaporation process significantly affect the combustion process [20] leading to poor performance of biodiesel fueled diesel engine [21]-[32]. The inferior performance of biodiesel operated diesel engine in comparison with conventional diesel fueled diesel engine is mainly due to change in fuel properties, engine design and operating parameters. In addition in DI diesel engine, the combustion chamber has been optimized for combustion of diesel, including improvement of mixing between injected fuel and in-cylinder air, and not for biodiesel. Apart from injection parameters, the shape of the combustion chamber can also help to form better mixtures. The shape of the combustion chamber and the fluid dynamics inside the chamber are of great importance in biodiesel combustion. As the piston moves upward, the gas is pushed into the piston bowl. The geometry of the piston bowl can be designed to produce a squish and swirling action which can improve the fuel/air mixture before ignition takes place. Therefore to achieve improved performance and further reductions in emissions, rapid and better air-biodiesel mixing is the most important requirement. Researchers [33] have carried out simulation studies to investigate the effect of piston bowl geometry on both engine performance and combustion efficiency in a direct injection (DI), turbocharged diesel engine for heavy-duty applications using STAR-CD. The simulation results show that, toroidal bowl with lip enhance the turbulence and hence results in better air-fuel mixing. As a result, the indicated specific fuel consumption and soot emission reduced, although the NO_x emission is increased owing to better mixing and a faster combustion process. Prasad et al [34] studied the effect of swirl induced by piston bowl geometries on pollutant emissions from a single cylinder diesel engine using CFD. Pollutant emission measurements indicated a reduction in emissions for toroidal, with slightly re-entrant type combustion chamber due to improved air swirl.

As the combustion chamber geometry affects the air–fuel mixing and the subsequent combustion and pollutant formation processes in a DI diesel engine an attempt has been made here to investigate the effect of combustion chamber design on air motion and thereby air-biodiesel mixing. In this investigation, numerical simulation was carried out using five types of combustion chamber geometries to analyze the air motion.

Geometric Modelling

The engine studied in this work was a stationary, single-cylinder, DI diesel engine with five different piston bowl shapes. These shapes are representative of the geometries usually employed for the optimum combustion process in real engines. The piston named HCC had a Hemispherical Combustion Chamber and used as a baseline model. Two pistons having open combustion geometries namely Shallow depth Combustion Chamber and Toroidal Combustion Chamber (named SCC and TCC respectively) and two other pistons having re-entrant combustion chamber geometries namely Shallow depth Re-entrant Combustion Chamber and Toroidal Re-entrant Combustion Chamber (named SRCC and TRCC respectively) were used. In order to maintain the compression ratio of the engine under consideration, while modeling, the bowl volumes for all the combustion chamber configurations were kept constant. Figure 1 shows the shapes and dimensions of five combustion chamber geometries used. The inlet valve axis is offset from the cylinder axis by 18.5 mm in the x direction and 2.0 mm in the y direction. The standard specification of the base engine selected for the simulation is given in Table 1.

Table 1: Standard engine specifications

Make	**Kirloskar TV1**
Type	Vertical diesel engine, 4stroke, water cooled, single cylinder
Displacement	661 cc
Bore & Stroke	87.5 mm & 110 mm
Compression ratio	17.5:1
Fuel	Diesel
Rated brake power	5.2 kW @ 1500 rpm
Ignition system	Compression ignition
Combustion chamber	Hemispherical combustion chamber

Modelling Methodology

The modeling and analysis of the combustion chamber configurations have been carried out using software packages. The software packages GAMBIT and STAR-CD were used. The pre-processor GAMBIT was used to create the computational domain of the engine and computational fluid dynamics code STAR-CD was used for solution of governing equations and post processing the results [35, 36]. A hexahedral block structured mesh was employed for the entire computational domain of the engine. Figure 2 shows the computational meshes employed for the simulation of different combustion chamber geometries.

Flow conditions inside the cylinder were predicted by solving momentum, continuity and energy equations [37, 38]. The simulation was carried out for a constant engine speed at non-reacting condition. Constant pressure boundary conditions were assigned for both intake and exhaust ports, so the dynamic effects were neglected. The initial values for pressure and temperature were 1.02 bar and 303 K respectively, with both variables considered as homogeneous in the whole domain. As the residual swirl of the flow in the cylinder at the end of the exhaust stroke was not taken into account, the flow was supposed to be quiescent initially. The initial turbulence intensity was set at 5% of the mean flow, and the integral length scale was estimated with the mixing length model of Prandtl [39]. The walls of the intake ports, the lateral walls of the valves and the cylinder head, the cylinder wall and the piston crown that form the walls of the combustion chamber were considered adiabatic.

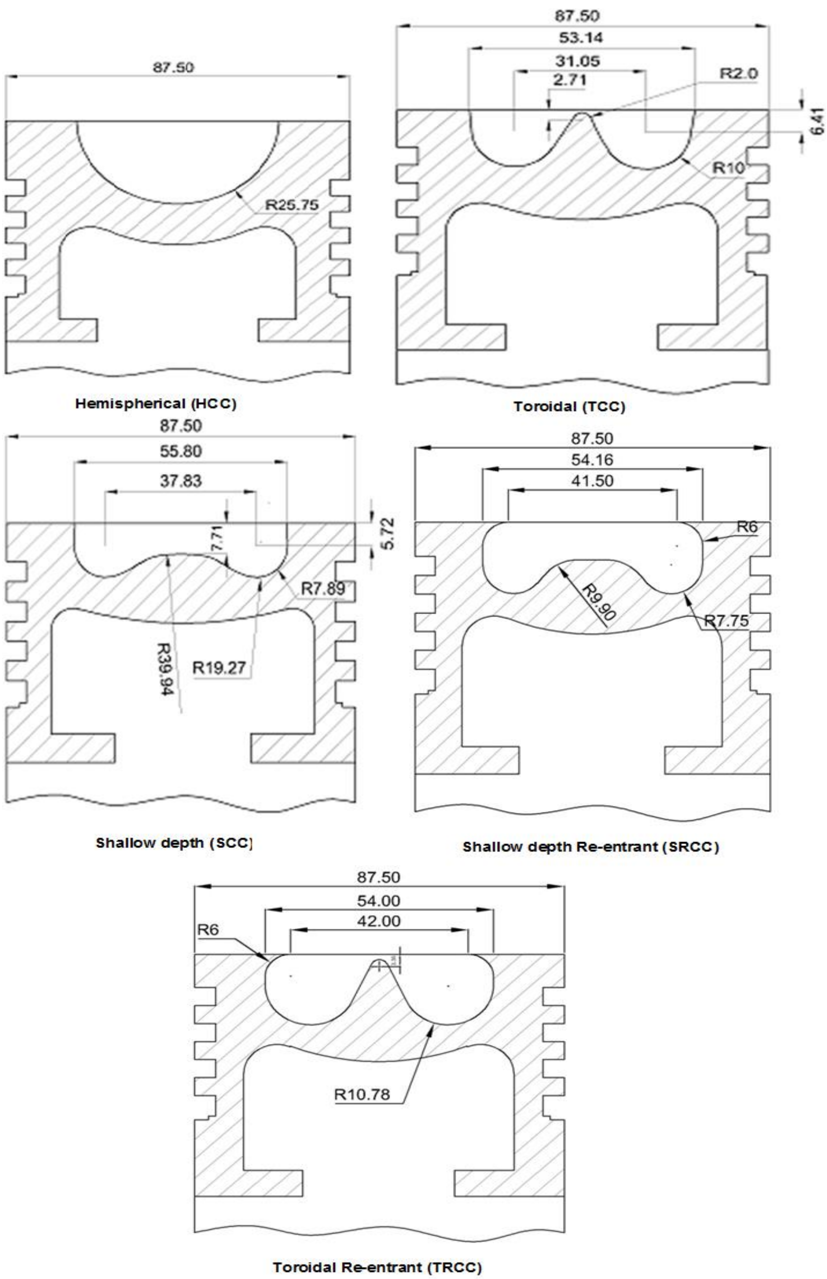

Figure 1: Schematic diagram of combustion chambers employed

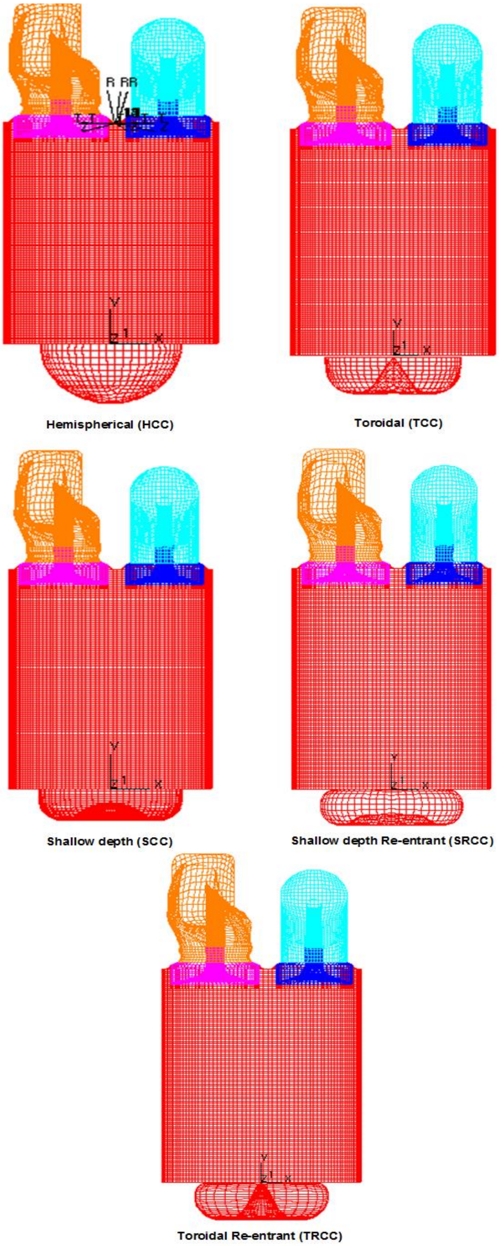

Figure 2: Computational domains of different combustion chamber geometries

The calculations began at TDC of the intake stroke and completed at 30 degrees after TDC (aTDC) of compression. In order to study the fluid flow behaviour in the analysis, quantities such as swirl velocity, Turbulent Kinetic Energy (TKE) and Swirl-Ratio (SR) were computed for the in-cylinder flow field about the cylinder axis. The quantity known as Swirl ratio is expressed as [3, 40],

$$SR = \frac{60H_z}{2\pi M_z \Omega_{cs}}$$

Where, H_z represents the total angular momentum of the in-cylinder fluid about the cylinder axis, M_z is the total moment of inertia of the fluid about the cylinder axis, Ω_{cs} is the angular speed of the crankshaft in rpm.

Results and Discussion

A numerical simulation study was carried out to investigate the effect of combustion chamber configuration on air motion inside the cylinder of a DI diesel engine motored at 1500 rpm. Five combustion chamber configurations namely HCC, SCC, TCC, SRCC and TRCC were modeled for the flow analysis in the first stage. This section describes the results from a comprehensive CFD study on the flow characteristics inside the cylinder of the engine. The flow in the cylinder during the intake and compression stroke was analyzed, and presented in the following section.

Swirl velocity

Figure 3 to 7 show the swirl velocity for the different combustion chamber geometries at compression TDC. The predicted swirl velocity was low for the open bowl configurations compared to the re-entrant bowl configurations. TRCC showed higher swirl mean velocity component than other combustion chamber geometries in all the locations. It was due to the induced tangential component of TRCC, which was able to sustain until the end of compression. The intensity of maximum swirl velocity at the end of compression stroke for TRCC (Max: 18.95 m/s) was observed maximum and a strong recirculation was observed due to the combustion chamber geometry. This will help in better fuel air interaction, which will lead to better combustion and performance. In the case of SCC swirl velocity was very low (Max: 7.743 m/s) and for HCC (Max: 10.56 m/s) and TCC (Max: 12.28 m/s) swirl velocity was higher than SCC. The maximum swirl velocity of SRCC (Max: 14.02 m/s) lie in between TCC and TRCC.

It was observed that for all the combustion chamber geometries, the radial distribution of swirl velocity component increased as the observation location was moved towards the bowl from the cylinder wall. When the observation location moved towards the bowl the frictional effect was less than the location of the cylinder wall [41, 42]. This led to the increase of mean swirl velocity near the bowl. Same trend was observed for all other combustion chamber configurations. It can also be seen from the Figures 3, 5, 6 and 7 that the swirl velocity was not so uniform throughout the cylinder and maximum occurred near the outer periphery of the bowl. However for SCC (Figure 4), the flow structure was so uniform and the maximum velocity magnitude was considerably less compared to TRCC. The TRCC created a strong swirl velocity at all locations due to its configuration. At compression TDC the max swirl velocity for HCC, SCC, TCC and SRCC were lower by 44%, 59%, 35.2% and 26% respectively compared to TRCC. The calculated velocities were generally in good agreement with the experimental results of Chen et al [43].

Swirl ratio

Figure 8 shows the details of swirl ratio (SR) during suction and compression for all the combustion chamber geometry configurations viz., HCC, SCC, TCC, SRCC and TRCC. As could be seen from the Figure 8 that, during compression the SCC produced very low swirl with peak swirl ratio value of 2.17, whereas, the TRCC produced the maximum swirl with peak swirl ratio value around 3.26, which was 1.5 times higher than SCC. The SRCC had swirl ratio in between TRCC and TCC with peak swirl ratio value around 3.04. It was also seen that increase of swirl ratio was more or less same for all the combustion chambers during the early stage of suction process.

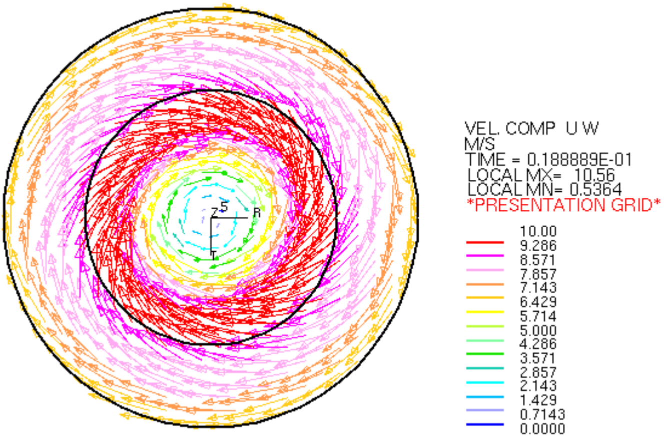

Figure 3: Swirl velocity vector at 360° CA aTDC for HCC

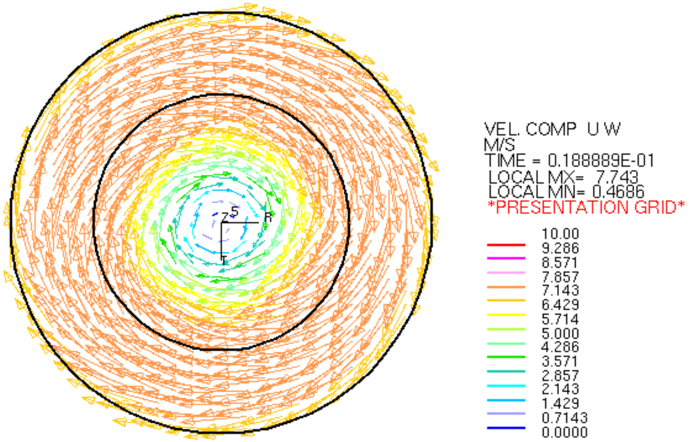

Figure 4: Swirl velocity vector at 360º CA aTDC for SCC

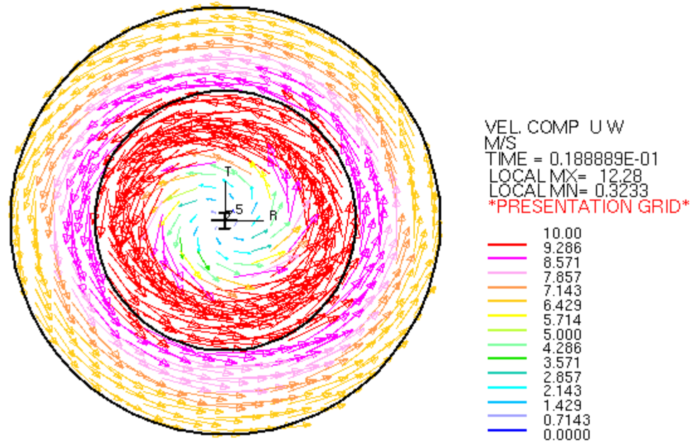

Figure 5: Swirl velocity vector at 360º CA aTDC for TCC

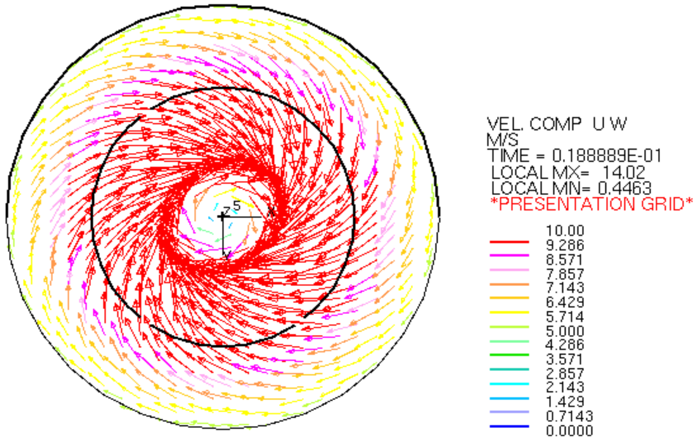

Figure 6: Swirl velocity vector at 360^o CA aTDC for SRCC

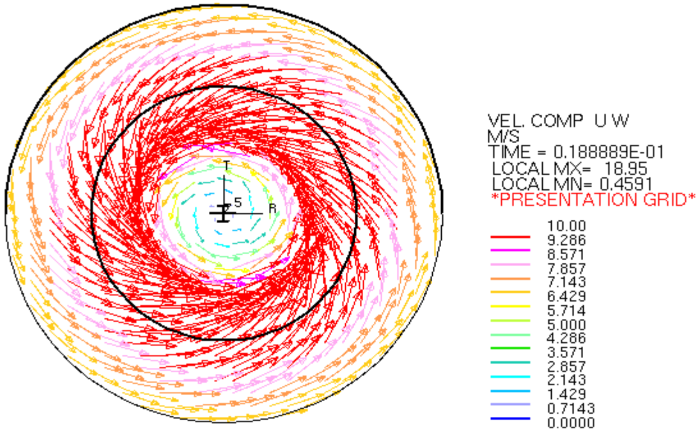

Figure 7: Swirl velocity vector at 360^o CA aTDC for TRCC

This shows that combustion chamber plays a less significant role on swirl during suction process. During the early stage of suction process, the increase in swirl between 0^o and 110° aTDC was quite considerable [44]. Further, it may be noted that the first peak occurring around 110° aTDC from the start of suction. This was attributable to the piston acceleration and reduction of pressure inside the cylinder. After reaching the peak around 110° aTDC, swirl ratio started reducing due to the increase in volume of cylinder and closing of the intake valve. This was also caused by the reduction of mass flow rate of incoming air and the friction between the wall and air inside the cylinder.

This decreasing trend continued in the first part of the compression stroke due to friction at the wall. However, beyond 300° aTDC swirl ratio started increasing. This was due to the axial upward flow induced a gradual increase of the swirl velocity in the top part of the piston [45]. It was also noted that the increase in swirl was quite small for SCC and the maximum swirl ratio was obtained for TRCC. Figure 8 shows the high intensity of swirl ratio for the TRCC, due to the combustion chamber configuration. Thus, it was well established that TRCC configuration was the best for sustaining swirl near the compression TDC. This result was in good agreement with the findings of Gunabalan and Ramaprabhu [41]. The different combustion chamber configurations i.e. HCC, SCC, TCC and SRCC had lower maximum swirl ratio by 22%, 33%, 14% and 6.7% respectively at 360° CA aTDC compared to that of TRCC. The maximum swirl ratio obtained for five combustion chamber geometries are tabulated in Table 2. The predicted swirl ratio values were largely in good conformity with the calculated swirl ratio results of Payri et al [46].

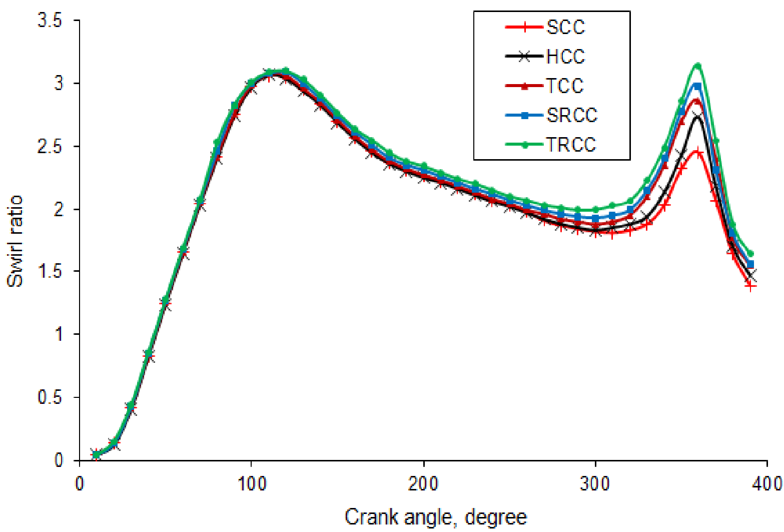

Figure 8 Comparison of swirl ratio for different combustion chambers

From Table 2 it was observed that, TRCC showed higher swirl ratio of 28% than baseline bowl HCC. These predictions were similar to the findings of

Payri et al [46], Gunabalan and Ramaprabhu [41] and B. Paul and V. Ganesan [44].The projection at the center of the TRCC and the lip provided reduced the effective diameter of the chamber, there by increased the angular momentum which results in higher swirl ratio. After compression TDC, during the expansion stroke, reverse squish as the flow exits from the piston bowl and wall friction contribute to the sudden fall of the swirl velocity.

Table 2: Mass average swirl ratio for five different combustion chamber geometries

Combustion chamber geometry	**Max swirl during suction stroke**	**Max swirl during compression stroke**
HCC	3.07	2.52
SCC	3.06	2.17
TCC	3.08	2.79
SRCC	3.12	3.04
TRCC	3.16	3.26

Turbulent kinetic energy

Figure 9 to Figure 13 show the Turbulent Kinetic Energy (TKE) for different configurations of combustion chambers at compression TDC. It was observed that the configuration of the combustion chamber of the engine directly affects the turbulence of the fluid inside the cylinder particularly during the end of the compression stroke. During the compression process the highest value of TKE was observed for TRCC at TDC [34]. At the beginning of suction stroke the air flows smoothly into the cylinder and the TKE gradually increased from 0° CA to maximum valve lift (at 110˚ crank angle) and then decreased with respect to the piston movement [47]. This was due to the mass flow reduction caused by the closing of the valve. It was also observed that high values of turbulent kinetic energy were found at the inlet valve exit, for all configurations. Turbulent kinetic energy started to decrease when the valve lift reached higher level and declined during the second half of induction [44]. Further, similar type of variation in TKE was reported by B. Murali Krishna and J.M. Mallikarjuna [48].

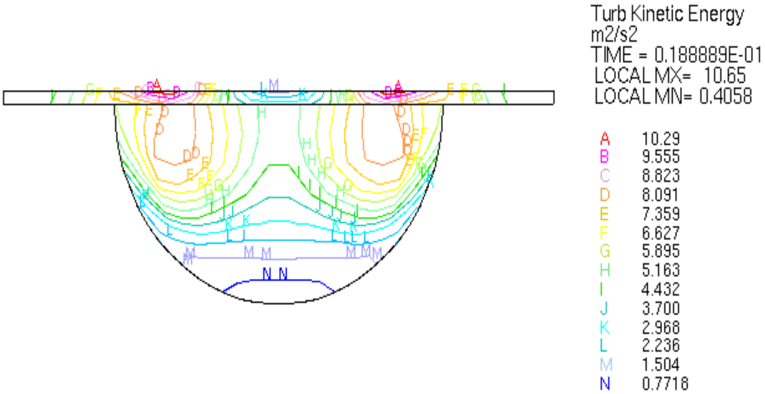

Figure 9: TKE contour plot for HCC at 360° CA aTDC

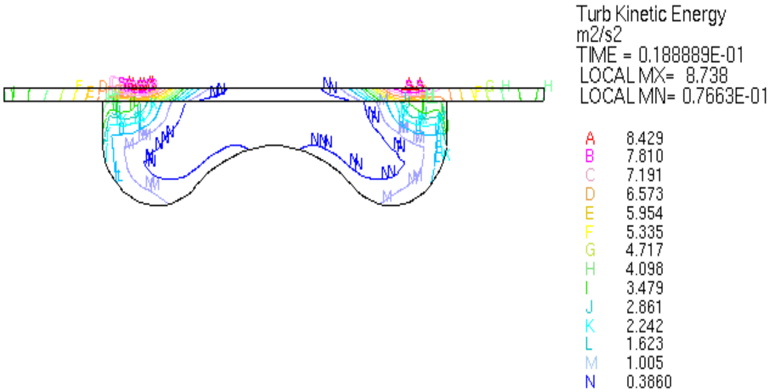

Figure 10: TKE contour plot for SCC at 360° CA aTDC

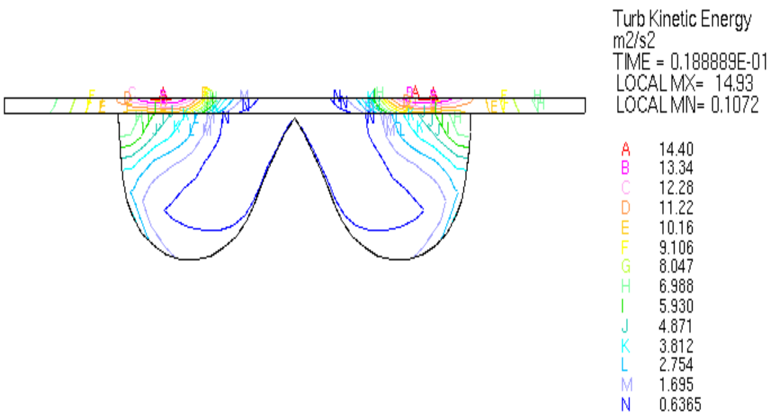

Figure 11: TKE contour plot for TCC at 360° CA aTDC

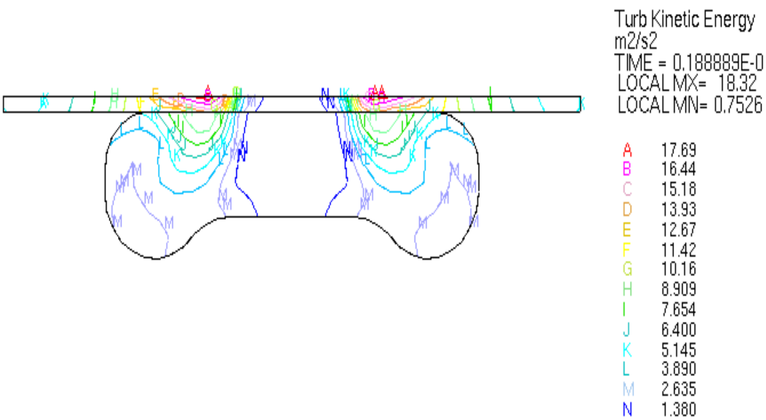

Figure 12: TKE contour plot for SRCC at 360° CA aTDC

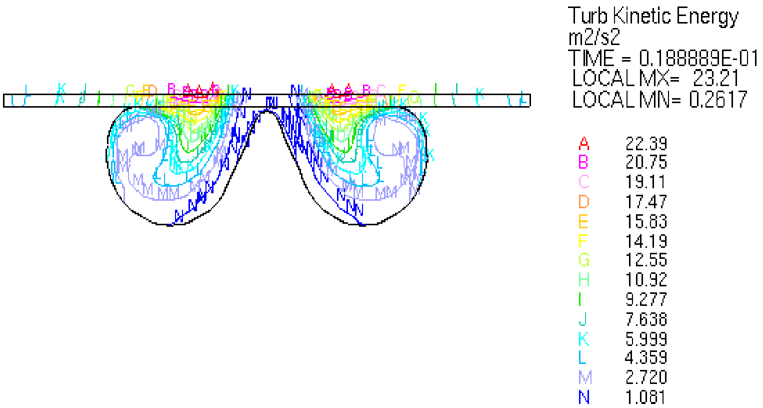

Figure 13: TKE contour plot for TRCC at 360° CA aTDC

For all the five combustion chamber geometries the same trend was observed during induction process and the variation of TKE for all five combustion chambers were identical; this means that the combustion chamber geometry does not play any major role in the turbulence generation during induction [46]. However, it was observed that during compression, the combustion chamber plays an important role in generating the turbulence inside the cylinder.

As could be seen from the Figure 14 that, at the end of compression, the TRCC produced very high turbulence with peak TKE value of around 23.21 m^2/s^2 whereas the baseline HCC produced the peak TKE value of around 10.65 m^2/s^2, which was 2.18 times lower than TRCC. The SRCC had peak TKE value of around 18.32 m^2/s^2 which, lie in between TRCC and TCC. It was also noted that the peak TKE value, was quite small for SCC (8.74 m^2/s^2) compared to other combustion chamber configurations. The peak TKE values for SRCC, TCC, SCC and HCC in comparison with that of TRCC decreased by 21%, 35.7%, 54% and 62% respectively at 360° CA aTDC. From the Figure 14 it can also be seen that lower values of TKE were observed for open bowl than re-entrant chambers, since the squish effect in these combustion chambers was smaller. The turbulent kinetic energy for the TRCC was found higher at compression TDC and early stage of expansion stroke. This was attributable to the shape of the combustion chamber i.e. the projection at the center of the TRCC and the lip provided reduced the effective diameter of the chamber, which results in higher TKE [45]. Thus TRCC seem to conserve better their turbulent energy.

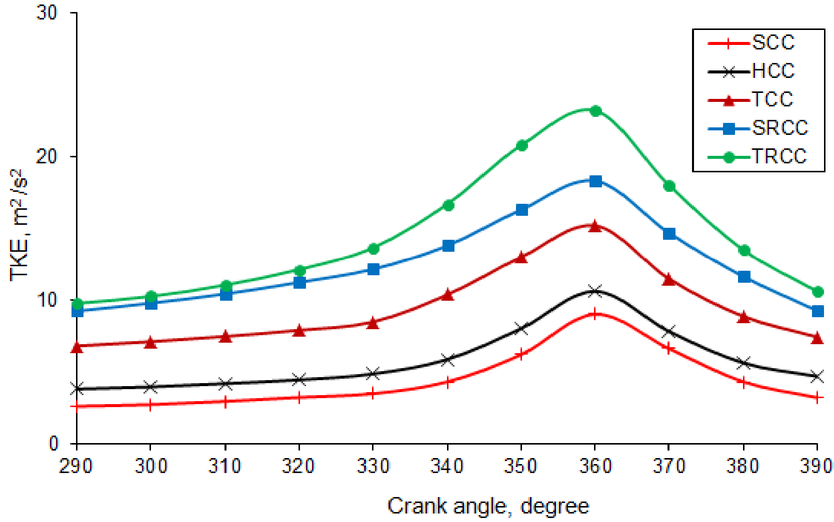

Figure 14: In-cylinder peak TKE at the end of compression for different combustion chambers

Conclusion

Based on the simulation of non-firing, in-cylinder flow analysis for the five combustion chamber configurations of DI diesel engine, the following observations and results can be highlighted;

1. Swirl generation of TRCC configuration was better than other piston bowl configurations. The effect of bowl geometry was quite prominent during the compression than the induction process. The predicted swirl velocity was low for the open bowl configurations compared to other two re-entrant bowl configurations.
2. It was found that piston bowl plays a less significant role on swirl generation during suction process. During compression the TRCC produced the maximum swirl with peak swirl ratio value of around 3.26, which was 1.29 times higher than the baseline HCC. Compared to TRCC, the other piston bowl configurations i.e. HCC, SCC, TCC and SRCC had lower, maximum swirl ratio by 22%, 33%, 14% and 6.7% respectively at 360^o CA aTDC.
3. TRCC configuration was found to have higher in-cylinder turbulence compared to the other piston bowl configurations. The peak TKE values for SRCC, TCC, SCC and HCC in comparison with that of TRCC were

lower by 21%, 35.7%, 54% and 62% respectively at 360º CA aTDC. Comparison of TKE shows that, the configuration of the combustion chamber directly affects the turbulence of the fluid inside the cylinder, particularly at the end of the compression stroke.

The results of these investigations show that during compression of DI diesel engine, the combustion chamber configuration plays a significant role in deciding the swirl and turbulence levels inside the cylinder. TRCC provides better air motion in the cylinder than other combustion chamber geometries.

References

[1] B. Challen and R. Barnescu, Diesel Engine Reference Book, Society of Automotive Engineers, (Bath Press, England, 1999).

[2] V. Ganesan, Internal Combustion Engines, 2nd Edn. (Tata McGraw Hill Publishers, New Delhi, 1998), pp. 295–355.

[3] J. B. Heywood, Internal Combustion Engine fundamentals, (McGraw Hill Publications, New York, 1988), pp.682–692.

[4] F. Brandl, Reverencic, W. Cartellieri and J.C. Dent, “Turbulent air flow in the combustion bowl of a DI diesel engine and its effect on engine performance,” SAE Paper 790040 (1979).

[5] A.D. Risi, T. Donateo, D. Laforgia,"Optimization of the Combustion Chamber of Direct Injection Diesel Engines" SAE 2003-01-1064 (2003).

[6] D.A. Kouremenos, D.T. Hountalas, A.D. Kouremenos. “Experimental investigation of the effect of fuel composition on the formation of pollutants in direct injection diesel engines,” SAE paper 1999-01-0189 (1999).

[7] H. Schapertons, F. Thiele, "Three dimensional computations for flow fields in DI piston bowls". SAE 860463, (1986).

[8] F.E. Corcione, A. Fusca and G. Valentino, "Numerical and Experimental Analysis of Diesel Air Fuel Mixing" SAE 931948 (1993).

[9] M.N. Nabi, M. S. Akhter and M.M.Z. Shahadat, “Improvement of engine emissions with conventional diesel fuel and diesel–biodiesel blends,” Bioresource Technology 97, 372–378 (2006).

[10] Chotwichien, A. Luengnaruemitchai and S. Jai-In, “Utilization of palm oil alkyl esters as an additive in ethanol–diesel and butanol–diesel blends,” Fuel 88(9), 1618-1624 (2009).

[11] M.M. Hasan, M.M. Rahman, and K. Kadirgama, “A revıew on homogeneous charge compressıon ıgnıtıon engıne performance usıng bıodıesel–dıesel blend as a fuel”, International Journal of Automotive and Mechanical Engineering 11, 2199-2211 (2015).

[12] A.S. Ramadhas, S. Jayaraj and C. Muraleedharan, "Use of vegetable oils as I.C. engine fuel- a review". Renewable Energy, 29(5), 727-742 (2004).
[13] S.C. Bhupendra, K. Naveen and M.C. Haeng, "A study on the performance and emission of a diesel engine fueled with jatropha biodiesel oil and its blends", Energy, 37, 616–622 (2012).
[14] S. Kumar, A. Chaube and S.K. Jain, "Experimental investigation of C.I. engine performance using diesel blended with jatropha biodiesel", International Journal of Energy and Environment, 3(3):471-484 (2012).
[15] P.K. Sahoo and L.M. Das, "Combustion analysis of jatropha, karanja and polanga based biodiesel as fuel in a diesel engine", Fuel, 88(6), 994–999 (2009).
[16] C.E. Goering, A.W. Schwab, M.J. Daugherty, E.H. Pryde and A.J Heakin, "Fuel properties of eleven vegetable oils", Transactions of ASAE, 25(6), 1472-1477 (1982).
[17] B. Baiju, M.K. Naik and L.M. Das, "A comparative evaluation of compression ignition engine characteristics using methyl and ethyl esters of Karanja oil," Renewable Energy 34(6), 1616-1621 (2009).
[18] P.K Devan and N.V. Mahalakshmi, "Study of the performance, emission and combustion characteristics of a diesel engine using poon oil-based fuels," Fuel Processing Technology 90(4), 513-519 (2009).
[19] M. Lapuerta, O Armas and J.R. Fernandez, "Effect of biodiesel fuels on diesel engine emissions," Progress in Energy and Combustion Science 34, 198–223 (2008).
[20] J.M. Desantes, J. Arregle, S. Ruiz and A. Delage, "Characterization of the injection combustion process in a di diesel engine running with rape oil methyl ester", SAE paper 1999-01-1497 (1999).
[21] K.K. Radha, S.N. Sarada, K. Rajagopal and E.L. Nagesh, "Performance and emission characteristics of CI engine operated on vegetable oils as alternate fuels", International Journal of Automotive and Mechanical Engineering, 4, 414-427 (2011).
[22] P.K. Sahoo, S.N. Naik and L.M. Das, "Studies on biodiesel production technology from jatropha curcas and its performance in a CI engine", J. Agri. Eng. Indian. Soc. Agri. Eng. (ISAE), 42(2), 18–24 (2005).
[23] B. Gokalp, E. Buyukkaya and H.S. Soyhan, "Performance and emissions of a diesel tractor engine fueled with marine diesel and soybean methyl ester", Biomass and Bioenergy, 35(8), 3575-3583 (2011).
[24] Z. Lei, C.S. Cheung, W.G. Zhang and H. Zhen, "Combustion, performance and emission characteristics of a DI diesel engine fueled with ethanol–biodiesel blends", Fuel, 90(5), 1743-1750 (2011).
[25] D.R. Constantine, M.D. Athanasios, G.G. Evangelos and C.R. Dimitrios, "Investigating the emissions during acceleration of a

turbocharged diesel engine operating with bio-diesel or n-butanol diesel fuel blends", Energy, 35(12), 5173-5184 (2010).
[26] S. Puhan, N. Vedaraman, G. Sankaranarayanan and B.V.B. Ram, "Performance and emission study of mahua oil (madhuca indica oil) ethyl ester in a 4-stroke natural aspirated direct injection diesel engine", Renewable Energy, 30, 1269–1278 (2005).
[27] T. Pi-qiang, H. Zhi-yuan, L. Di-ming and L. Zhi-jun, "Exhaust emissions from a light-duty diesel engine with jatropha biodiesel fuel", Energy, 39(1) 356-362 (2012).
[28] B. Vicente, M.L. Jose, P. Benjamin and G.L. Waldemar, "Comparative study of regulated and unregulated gaseous emissions during NEDC in a light-duty diesel engine fuelled with Fischer (2011).
[29] S. Saravanan , G. Nagarajan , R.G. Lakshmi Narayana and S. Sampath, "Combustion characteristics of a stationary diesel engine fuelled with a blend of crude rice bran oil methyl ester and diesel", Energy, 35(1), 94-100 (2010).
[30] Ekrem Buyukkaya, "Effects of biodiesel on a DI diesel engine performance, emission and combustion characteristics" Fuel, 89(10), 3099-3105 (2010).
[31] H. Song, B.T. Tompkins, J.A. Bittle and T.J. Jacobs, "Comparisons of NO emissions and soot concentrations from biodiesel-fuelled diesel engine", Fuel, 96, 446-453 (2012).
[32] A.K. Agarwal, "Biofuels (alcohols and biodiesel) applications as fuels for internal combustion engines" Prog. Energy Combust. Sci, 33, 233-271 (2007).
[33] S. P. Venkateswaran and G. Nagarajan, "Effects of the re-entrant bowl geometry on a DI turbocharged diesel engine performance and emissions - a CFD approach", J Eng Gas Turb Power, 132(12), 122803-13 (2010).
[34] B.V.V.S.U. Prasad, C.S. Sharma, T.N.C. Anand and R.V. Ravikrishna, "High swirl-inducing piston bowls in small diesel engines for emission reduction", Applied Energy, 88(7), 2355–2367 (2011).
[35] M. Auriemma, F.E. Corcione, R. Macchioni and G. Valentino, "Interpretation of air motion in reentrant bowl in-piston engine by estimating Reynolds stresses", SAE Paper No. 980482 (1998).
[36] T. Okazaki, H. Miyazaki, M. Sugimoto, S. Yamada and M. Aketa, "CFD approach for optimum design of DI combustion system in small versatile diesel engine", SAE Paper No. 1999-01-3261 (1999).
[37] Z.U.A. Warsi, "Conservation form of the Navier-Stokes equations in general nonsteady coordinates", AIAA Journal, 19(2), 240-242 (1981).
[38] S.C. Kong, Z. Han, and R.D. Reitz, "The development and application of a diesel ignition and combustion model for multidimensional engine simulation", SAE Paper No. 950278 (1995).

[39] B.E. Launder and D.B. Spalding, Lectures in mathematical models of turbulence, (Academic Press Inc, London, 1972).
[40] Y. Shi, H.W. Ge and R.D. Reitz, Computational optimization of internal combustion engines, (Springer, London, 2011), pp.151–152.
[41] Gunabalan and R. Ramaprabhu, "Effect of piston bowl geometry on flow, combustion and emission in DI diesel engine--a CFD approach", International Journal of Applied Engineering Research, 4(11), 2181-2188 (2009).
[42] Jayashankara and V. Ganesan, "Effect of fuel injection timing and intake pressure on the performance of a DI diesel engine-A parametric study using CFD", Energy Conversion and Management, 51(10), 1835-1848 (2010).
[43] Chen, A. Veshagh and S. Wallace, "Intake flow predictions of a transparent DI diesel engine", SAE Paper No. 981020 (1998).
[44] Paul and V. Ganesan, "Flow field development in a direct injection diesel engine with different manifolds", International Journal of Engineering, Science and Technology, 2(1), 80-91 (2010).
[45] P. Vijayakumaran, R.Elayaraja, A. Muthuvel, Dr. M.Subramanian and R. Murukesan, " Numerical simulation of combustion chamber geometry on a H.S.D.I. diesel engine – a CFD approach", IOSR Journal of Mechanical and Civil Engineering, 4, 66-73 (2014).
[46] F. Payri, J. Benajes, X. Margot and A. Gil, "CFD modeling of the in-cylinder flow in direct-injection diesel engines", Computers & Fluids, 33, 995–1021 (2004).
[47] B.M. Krishna and J.M. Mallikarjuna, "Characterization of flow through the intake valve of a single cylinder engine using particle image velocimetry", Journal of Applied Fluid Mechanics, 3(2), 23-32 (2010).
[48] B.M. Krishna and J.M. Mallikarjuna, "Effect of engine speed on in-cylinder tumble flows in a motored internal combustion engine - an experimental investigation using particle image velocimetry", Journal of Applied Fluid Mechanics, 4(1), 1-14 (2011).

Journal of Mechanical Engineering *Vol 13(2), 99-111, 2016*

Physical Properties Analysis of UV-Crosslinked Sulfonated Poly Ether Ether Ketone and Methyl Cellulose

Nordiana Nabilla Ramly, Ab Malik Marwan Ali,
Nursyahida Sahli, Nazli Ahmad Aini
Faculty of Applied Sciences, Universiti Teknologi MARA,
40450 Shah Alam, Selangor, Malaysia
Institute of Science, Universiti Teknologi MARA, 40450
Shah Alam, Selangor, Malaysia

Muhd Zu Azhan Yahya
Faculty of Science and Defense Technology, Universiti
Pertahanan Nasional Malaysia, 57000 Kuala Lumpur,
Malaysia
Institute of Science, Universiti Teknologi MARA, 40450
Shah Alam, Selangor, Malaysia

Siti Fatimah Aminuddin
Centre of Foundation Studies, Universiti Teknologi
MARA, 42300 Puncak Alam, Selangor, Malaysia

Nur Adyanie Mohamad
Department of Electronic and Mechanical Engineering,
Dundalk Institute of Technology
Country Louth, Ireland

ABSTRACT

Proton exchange membrane materials based on sulfonated Poly Ether Ether Ketone with Methyl Cellulose are developed in this study. The hybrid membrane is exposed to UV radiation with photoinitiator to improve the membrane dimensional stability up to 50%. The hybrid membranes characterized by FTIR shows the crosslinking occurs by formation of C-C bond from BEE instead of the consumption of SO_3H *group. This new crosslinked hybrid membrane shows good prospect for the use as proton exchange membrane in fuel cell.*

ISSN 1823- 5514

Received for review: 2016-04-19
Accepted for publication: 2016-10-27
Published: 2016-12-19

Keywords: *Proton Exchange Membrane, UV Crosslink, Sulfonated Poly Ether Ether Ketone, Benzoin Ethyl Ether*

Introduction

At present, the most widely commercialized proton exchange membranes, PEMs are Nafion-based perfluorinated ionomer polymers. Despite of having outstanding performance such as good conductivity, excellent mechanical and chemical stability, the membrane suffers from high fuel crossover and is difficult to synthesize. This shortcomings lead to research on alternative new PEM materials that have adequate electrochemical properties but more economic such as Sulfonated Poly Benzimidazoles (SPBI), Sulfonated Poly Ether Ether Ketone (SPEEK) and Sulfonated Polyimides (SPI) [1]. Among these potential candidates, SPEEK is most promising because it has high thermal stability, good mechanical strength and high conductivity [2]–[5]. However, SPEEK is too dependable on its degree of sulfonation (DS), too high DS can cause excessive membrane swelling leading to membrane dissolution while too low DS can lead to insufficient conductivity hence becomes impractical for PEMFC application [6].

Much effort has been made to rectify these problems. According to H. Hou et al. one of the solutions that have gained attention is UV-crosslinking [7]. This simple but powerful method is able to improve the dimensional stability of PEM. The down side of UV-crosslink technique is the consumption of $–SO_3H$ groups that leads to lower proton conductivity compared with the non-crosslinked PEMs. To overcome this issue photoinitiator Benzoin Ethyl Ether (BEE) is introduced in the polymer to initiate crosslink by the formation of a C-C bond instead of consuming $–SO_3H$ group.

Previous studies show UV-crosslinking SPEEK polymer with biodegradable polymer modifies the hybrid membrane by restricting the mobility of polymer chains hence forming more compact network [8]–[10]. Chitosan and cellulose acetate are one of the biodegradable polymers that have been made into crosslinked hybrid membrane. In this study Methyl Cellulose (MC) is chosen as it is abundant in nature and for its ability to retain water and form membrane easily. It is a modified type of cellulose with a tendency to form crosslinked three-dimensional network hydrogels that tend to swell in water or biological fluids [11]. To evaluate the physical properties of Sulfonated Poly Ether Ether Ketone-Methyl Cellulose (SPEEK-MC), several characterizations has to be taken into consideration i.e. the hybrid membrane water uptake, the solubility test, the Fourier Transform Infra Red Spectroscopy (FTIR) and Proton Nuclear Magnetic Resonance (^{1}HNMR) spectra.

Experimental

Sample preparation

The synthesis of hybrid membrane involves two stages. The first stage is the synthesis of SPEEK membrane and the second stage incorporates SPEEK with MC by UV-crosslinking [2,10]. For synthesis SPEEK membrane, the Poly Ether Ether Ketone (PEEK) underwent a sulfonation process by dissolving it in concentrated H_2SO_4 (95% - 98%) with continuous vigorous and constant stirring at room temperature for 84 hours. The ratio of the polymer with the acid is 10g:25mL. Then the polymer was washed with distilled water and filtered. The washing and filtering steps were repeated until the acidic polymer's pH turned neutral (Ph 7). After that the polymer was dried in an oven at 50°C for 8 to 10 hours. The DS of the resulted membrane was determined with 1HNMR [10]. The second stage is the synthesis of Sulfonated Poly Ether Ether Ketone–Methyl Cellulose (SPEEK-MC) hybrid membrane. Each of SPEEK and MC was dissolved in DMSO separately to become solutions before mixing them together. For this study the desired composition for a membrane was 1.7g with thickness ranges from 1.3 to 1.7mm and the composition ratio used was $SPEEK_{(1-X)}MC_{(X)}$ (X=2,4,6,8,10). The homogeny solution was crosslinked with UV-irradiation technique for desired period (15 and 30 minutes) with 5wt%, 10wt% and 15wt% Benzoin Ethyl Ether (BEE) as photoinitiator and was let dry in an oven at 50°C for 48 hours [12,13].

Characterization

The ^{1}HNMR spectra were used to measure the DS. The concentration of the polymer was 30mg ml^{-1} and deuterated dimethyl sulfoxide (DMSO-6) was used as solvent. The ratio between the peak area of Hs and the integrated peak area of all the proton signals (Hx; x = a, b, c, d, a', b', c', d') was expressed as Equation (1).

$$\frac{peak\ area\ (Hs)}{\Sigma\ peak\ area\ (Hx)} = \frac{y}{12(1-y)+10y} = \frac{y}{(12-2\mathrm{y})} \qquad (1)$$

$$total\ DS\ = y \times 100$$

Solubility for SPEEK membranes with varied DS is tested to analyze the membrane behavior in certain type of solvent. The obtained SPEEK membranes are immersed in selected solvent i.e. DMSO, DMF, methanol and hot water.

To check the membrane dimensional stability, water uptake test was essential. The pre-weighed membranes were immersed in distilled water for

24 hours and weighed after mopping with plotting paper. The percent water absorption capacity was determined with Equation (2) [3]:

$$\frac{\mathrm{Wwet} - \mathrm{Wdry}}{\mathrm{Wdry}} \times 100 \qquad (2)$$

Where W_{wet} is the weight of the wet membrane sample and W_{dry} is the weight of the same membrane sample placed in an oven at 100 °C for 24 hours.

The FTIR spectra of the membranes for MC, SPEEK, SPEEK-MC and SPEEK-MC-BEE PEM are analysed with Perkin Elmer 283B FTIR spectrometer in the wavenumber range of 500–4000cm^{-1} with resolution of 2cm^{-1} [6].

Result and Discussion

Degree of Sulfonation

Degree of sulfonation is determined by 1HNMR. The hydroquinone segment of the PEEK is introduced with sulfonic groups ($–SO_3H$). Figure 1 shows the structure of PEEK polymer prior and after sulfonation process. Non 1HNMR spectra for pristine PEEK is recorded as it is only soluble in strong acid. Table 1 shows 60 hours of sulfonation in room temperature produce DS of 68%. The sulfonation causes a total of 0.20ppm down field shift between the hydrogen of H_S and $H_{C'}H_{D'}$ in the hydroquinone ring. The $H_{B'}$ and $H_{C'}$ signals that are associated with hydroquinone ring show doublets at 7.8ppm and 8.0ppm respectively. While 72 hours of sulfonation produces DS of 88% and 84 hours produces DS of 95%. The H_C and H_B’ intensities increase proportionally with DS. Sulfonation time, temperature and the amount of H_2SO_4 used affect the resulted DS. Sulfonation proceeds in slow rate at room temperature and needs more than 48 hours just to reach above 50% DS [14]. Thus 60 hours of sulfonation of PEEK at room temperature produces SPEEK with the total DS of 68% indicating the SPEEK polymer is suitable for further test [10,15].

Table 1**:** Sulphonation time and degree of sulfonation

Sulphonation time (hours)	**Degree of sulphonation, DS (%)**
60	68
72	88
84	95

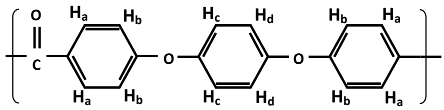

Unsubstituted repeat unit

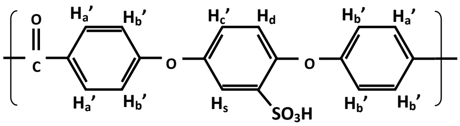

-SO_3H substituted repeat unit

Figure 1: Nomenclature of PEEK and SPEEK

Solubility Test

PEEK can withstand a broad range of chemical reagents. The sturdy intercrystalline forces cause the polymer to only dissolve in strong acids. Sulfonating the polymer PEEK makes the polymer soluble in many other solvents such. The dissolution properties of SPEEK are dependent with its degree of sulphonation, DS. The solubility test is carried out in search of the most suitable solvent to cast SPEEK membranes. Table 2 summarizes SPEEK solubility with varied sulphonation period. For SPEEK with DS below 30% at non-extreme temperature the samples are insoluble in most solvents except in strong acid. Those with DS higher than 30% are soluble in hot DMF, DMAc and DMSO while for DS above 40% SPEEK become soluble in DMF, DMAc and DMSO at room temperature. At 80% of DS, the SPEEK became soluble in methanol and at 100% of DS it is soluble in hot water and these results are in agreement with L. Li et al. [16]. In conclusion that the most suitable solvent to cast SPEEK membrane are DMF and DMSO because SPEEK polymer retains good solubility in them. As for crosslinked sulphonated membranes, they are insoluble in DMF and DMSO however became soluble in water and methanol.

Table 2: Solubility test of SPEEK polymer with various DS and solvent

Sulphonation period (hours)	**DS ± 5 (%)**	**Solvent**
40	30	DMSO, DMF
45	40	DMSO, DMF
50	50	DMSO, DMF
55	60	DMSO, DMF
60	70	Methanol
65	80	Methanol
70++	90	Hot water

FTIR results

Figure 2 shows the FTIR spectra for PEEK and SPEEK membrane. The sulphonation process of PEEK leads to significant differences in the IR spectrum between sulfonated PEEK (SPEEK) and pristine PEEK. The presence of SO_3H groups is observed with the absorption bands at 3400, 1248, 1078, 1022, and 706cm^{-1}. The broad band at 3500–3300cm^{-1} can be assigned as the O–H vibration of the sulfonic acid group and is in agreement with S. M. J. Zaidi et al. [5] and J. Xi et al [17]. The other bands are assigned as various sulfur-oxygen vibrations; asymmetric O=S=O stretch (1248cm^{-1}), symmetric O=S=O stretch (1078cm^{-1}), S=O stretch (1022cm^{-1}), and S–O stretch (706cm^{-1}).

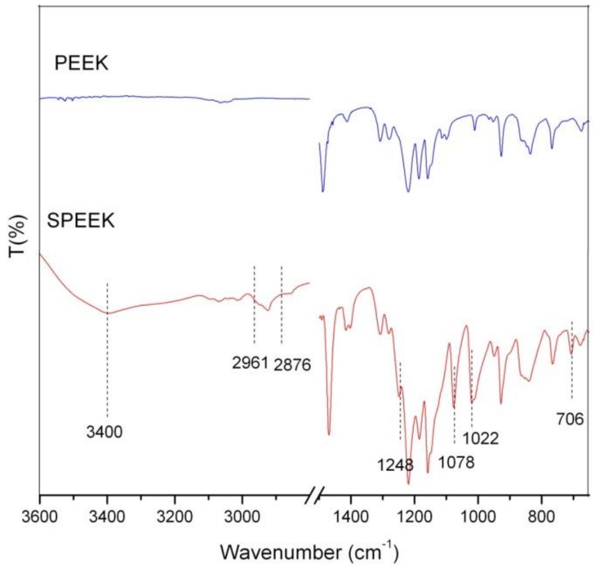

Figure 2: FTIR spectra of PEEK and SPEEK membranes

For MC, FTIR technique is used to study the hydrogen (H_2) bonds and hydroxyl (OH) stretching. Cellulose is the main constituent in natural fibers. Its strong crystalline structure is made of extensive hydrogen bonding within the cellulose chain. In the original data set i.e. Figure 3, the OH sub peaks are not visible individually. Thus they need mathematical method i.e. deconvolution to find the exact peak for hydrogen bonding and is shown in Figure 4. The regions of hydroxyl stretching are between 3800cm^{-1} and 3000cm^{-1} and the stretching was observed at 3445cm^{-1}. After deconvulated, the sub peaks positions are found at 3547cm^{-1}, 3414 cm^{-1}, 3289cm^{-1} and 3162cm^{-1}. These bands are associated with the valence vibration of hydrogen bonded OH groups. The first band at 3547cm^{-1} is related with the intra molecular hydrogen bond of O_2H---O, second band at 3414cm^{-1} is related with the intra molecular hydrogen bond of O_3H---O, third band at 3289cm^{-1} is related with intermolecular hydrogen bond of O_6H---O and last band at 3162cm^{-1} is related with the O-H stretching. The composition of MC does not have any effect at this peak position [18].

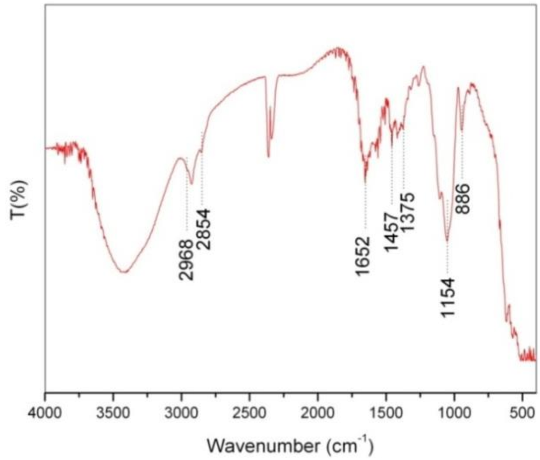

Figure 3: FTIR spectra of Methyl Cellulose

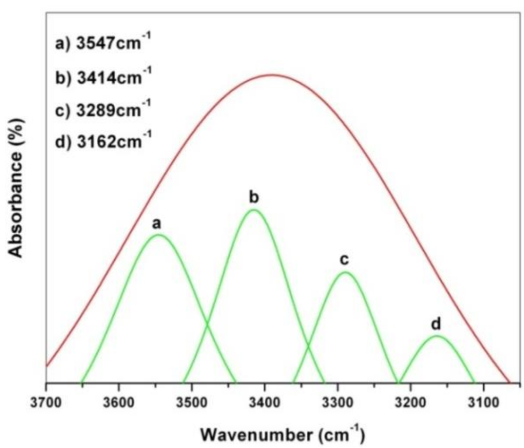

Figure 4: FTIR deconvolution spectra of MC polymer

Figure 5 depicts the spectra of SPEEK PEM after MC is incorporated for enhancing the binding capacity of the water. Hydrocarbons containing methyl groups showed at two distinct bands at 2961cm^{-1} and 2876cm^{-1}. At 2961cm^{-1}, the peak corresponds to asymmetrical (as) stretching mode i.e. v_{as} CH_3 which the two C-H bonds of the methyl groups are extending and the third C-H bond is contracting. At 2876cm^{-1}, the peak arises from symmetrical (s) stretching i.e. ($vsCH_3$) in which all three of the C-H bonds contract and extend in phase. The presence of methyl groups should result in strong absorption at positions discussed, however only small amount of MC i.e. 0.04g to 0.2g are added thus resulting in tentative absorption.

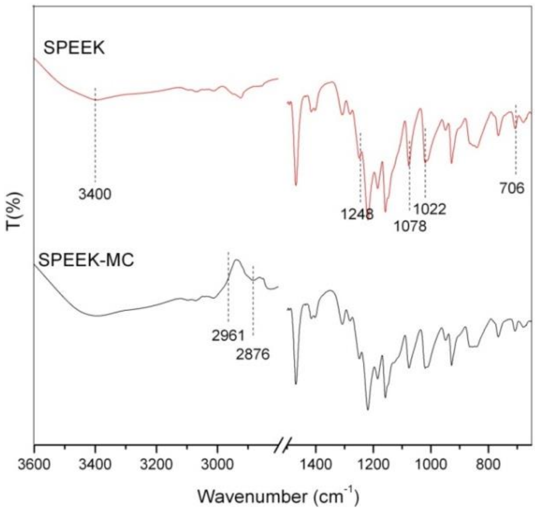

Figure 5: FTIR spectra of SPEEK-MC and SPEEK-MC-BEE

Both SPEEK and MC polymer are not photo responsive types thus they need photoinitiator to crosslink with each other. In this study, Benzoin Ethyl Ether used as photoinitiator decomposes into active radical. While exposed to UV light, the energy is transported to other molecules thus producing crosslinking reaction[19,20]. Figure 6 shows the addition of BEE and UV-crosslink technique could alter the functional group and the structure of the SPEEK-MC membrane. The difference period time for UV irradiation and amount of BEE effects on the membrane structure are shown in Figure 7 and Figure 8. The C=C double bonds peak at became less apparent with increasing UV irradiation period due to carbons are mainly used in crosslinking process. It can be concluded that very few chemical structure was formed as PEEK has high resistance to irradiation even after increasing doses of photoinitiator and longer exposure of membrane to UV-light.

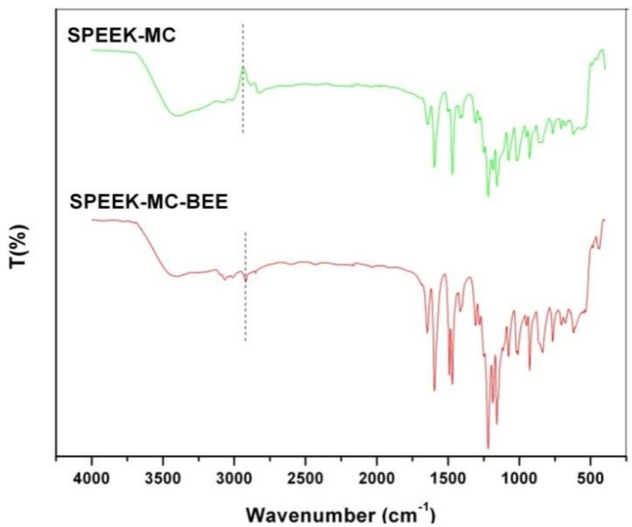

Figure 6: FTIR spectra of SPEEK-MC and SPEEK-MC-BEE

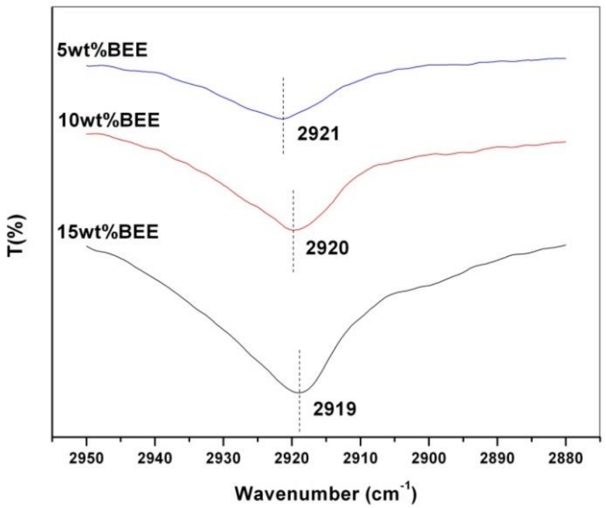

Figure 7: FTIR Spectra of 15 Minutes UV-Crosslinked SPEEK-MC-BEE

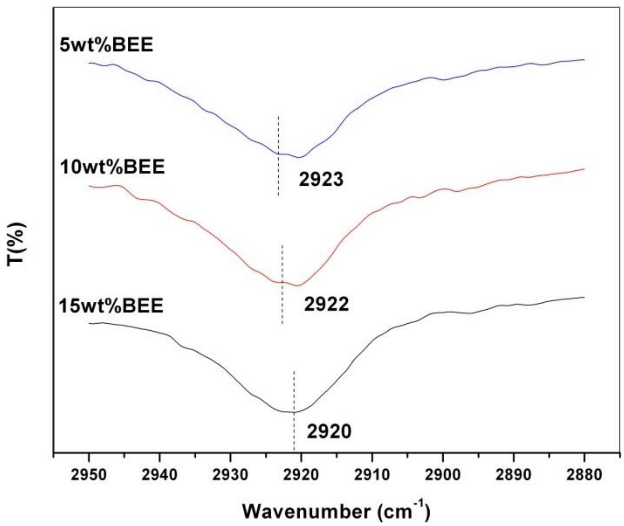

Figure 8: FTIR Spectra of 30 minutes UV-Crosslinked SPEEK-MC-BEE

Water Uptake

The sulfonation of PEEK introduces hydrophilicity properties in polymer electrolyte. Table 3 summarizes the water uptake for both crosslinked and non-crosslinked membranes. The water uptake for pure SPEEK is 27%. After the incorporation of MC into the membrane, the water uptake continues to increase with increasing amount of MC. Thus, leads to membrane dissolution in water. Contrary to non-crosslinked membrane, the water uptake for crosslinked membrane is acceptable. The water uptake for (98%)SPEEK(2%)MC, (96%)SPEEK(4%)MC, (94%)SPEEK(6%)MC and (92%)SPEEK(8%)MC are 25%, 27%, 32% and 39% respectively thus indicating they are suitable for further use. The water solubility of MC is primarily due to the reduced number of inter-chain hydrogen bonds. Water molecules are prone to form a cage like structure around the hydrophobic substituent on MC thus can attract more water. High water uptake leads to high conductivity but can lead to low dimensional stability and solubility in water if exceeded. Adaptation of crosslinking method results in denser structure and smaller free volume membrane [21]. Therefore decreases the membrane ability to absorb water. In hydrous condition the water molecule can help to dissociate sulfonic acid group and facilitate proton mobility which is an advantageous to the PEM.

Table 3: water uptake at room for SPEEK and SPEEK-MC membranes with and without UV-crosslink

Membrane	**Water uptake (%)**	
	Non-crosslinked	**Crosslinked**
(98%)SPEEK(2%)MC	51	25
(96%)SPEEK(4%)MC	55	27
(94%)SPEEK(6%)MC	61	32
(92%)SPEEK(8%)MC	78	39
(90%)SPEEK(10%)MC	>100	67
Pure SPEEK	27	-

Conclusion

Proton exchange membrane composed of SPEEK and MC are synthesized then are modified by UV-crosslinking. The effect of UV-irradiation period and photoinitiator BEE composition on the proton exchange membrane is examined. The outcome indicated that both stirring and drying period play crucial role in determining the sulfonation degree of a PEM. 60 hours of sulfonation produces degree of sulfonation 68%. FTIR result proves the occurrence of sulfonation when new peaks of $–SO_3$ groups appear and proves crosslink reaction is initiated by C-C bonds instead of $–SO_3$ groups consumption when using BEE as photoinitiator. Methyl Cellulose when crosslinked to SPEEK membrane enhances its binding capacity of water and improves its conductivity but at the same time maintains the membrane dimensional stability.

Acknowledgment

The authors are gratefully thanks to Ministry of Education (MOE) for supporting this research under the RAGS grant (600-RMI/RAGS 5/3(12/2012)) and Universiti Teknologi MARA (UiTM) for the facilities provided in succeeding this research.

References

[1] C. Fiori, a. Dell'Era, F. Zuccari, a. Santiangeli, a. D'Orazio, and F. Orecchini, "Critical review of fuel cell's membranes and identification of alternative types for automotive applications," Int. J. Hydrogen Energy (2015).

[2] V. R. Hande, S. K. Rath, S. Rao, and M. Patri, "Cross-linked sulfonated poly (ether ether ketone) (SPEEK)/reactive organoclay nanocomposite proton exchange membranes (PEM)," J. Memb. Sci., vol. 372, no. 1–2, pp. 40–48 (Apr. 2011).

[3] H. Maab and S. P. Nunes, "Modified SPEEK membranes for direct ethanol fuel cell," J. Power Sources, vol. 195, no. 13, pp. 4036–4042 (Jul. 2010).

[4] M. Rikukawa and K. Sanui, "Proton-conducting polymer electrolyte membranes based on hydrocarbon polymers," Prog. Polym. Sci., vol. 25, pp. 1463–1502 (2000).

[5] S. M. J. Zaidi, "Polymer Sulfonation - A Versatile Route To Prepare Proton-Conducting Membrane Material For Advanced Technologies," Arab. J. Sci. Eng., vol. 28, no. 2, pp. 183–194 (2003).

[6] S. Kaliaguine, S. . Mikhailenko, K. . Wang, P. Xing, G. Robertson, and M. Guiver, "Properties of SPEEK based PEMs for fuel cell application," Catal. Today, vol. 82, no. 1–4, pp. 213–222 (Jul. 2003).

[7] H. Hou, M. Luisa, D. Vona, and P. Knauth, "Building bridges : Crosslinking of sulfonated aromatic polymers — A review," J. Memb. Sci., vol. 423–424, pp. 113–127 (2012).

[8] S. Wang, C. Zhao, W. Ma, G. Zhang, Z. Liu, J. Ni, M. Li, N. Zhang, and H. Na, "Preparation and properties of epoxy-cross-linked porous polybenzimidazole for high temperature proton exchange membrane fuel cells," J. Memb. Sci., vol. 411–412, pp. 54–63 (Sep. 2012).

[9] S. Zhong, C. Liu, and H. Na, "Preparation and properties of UV irradiation-induced crosslinked sulfonated poly(ether ether ketone) proton exchange membranes," J. Memb. Sci., vol. 326, no. 2, pp. 400–407 (Jan. 2009).

[10] N. Aini, M. Yahya, and A. Lepit, "Preparation and Characterization of UV Irradiated SPEEK/Chitosan Membranes," Int. J. Electrochem. Sci., vol. 7, pp. 8226–8235 (2012).

[11] S. Rimdusit, K. Somsaeng, P. Kewsuwan, C. Jubsilp, and S. Tiptipakorn, "Comparison of Gamma Radiation Crosslinking and Chemical Crosslinking on Properties of Methylcellulose Hydrogel," Eng. J., vol. 16, no. 4, pp. 15–28 (Jul. 2012).

[12] S. Swier, Y. S. Chun, J. Gasa, M. T. Shaw, and R. A. Weiss, "Sulfonated Poly (ether ketone ketone) Ionomers as Proton Exchange Membranes," Polym. Eng. Sci. (2005).

[13] J. Roeder, H. Silva, S. Nunes, and a Pires, “Mixed conductive blends of SPEEK/PANI,” Solid State Ionics, vol. 176, no. 15–16, pp. 1411–1417 (May 2005).
[14] H. Erdener, R. G. Akay, H. Yücel, N. Baç, and İ. Eroğlu, “Effects of sulfonated polyether-etherketone (SPEEK) and composite membranes on the proton exchange membrane fuel cell (PEMFC) performance,” Int. J. Hydrogen Energy, vol. 34, no. 10, pp. 4645–4652 May 2009).
[15] R. Yee, K. Zhang, and B. Ladewig, “The Effects of Sulfonated Poly(ether ether ketone) Ion Exchange Preparation Conditions on Membrane Properties,” Membranes (Basel)., vol. 3, no. 3, pp. 182–195 (Aug. 2013).
[16] L. Li, “Sulfonated poly(ether ether ketone) membranes for direct methanol fuel cell,” J. Memb. Sci., vol. 226, no. 1–2, pp. 159–167 (Dec. 2003).
[17] J. Xi, Z. Li, L. Yu, B. Yin, L. Wang, L. Liu, X. Qiu, and L. Chen, “Effect of degree of sulfonation and casting solvent on sulfonated poly(ether ether ketone) membrane for vanadium redox flow battery,” J. Power Sources, vol. 285, pp. 195–204 (Jul. 2015).
[18] K. Turhan, E. Sahbaz, and A. Goner, “A spectrophotometric study of hydrogen bonding in Methylcellulose-based edible film plasticized by Polyethylene Glycol,” J. Food Sci., vol. 66, no. 1, pp. 59–62 (2001).
[19] S. Sarmad, Polysaccharide Based Graft Copolymers. Berlin, Heidelberg: Springer Berlin Heidelberg (2013).
[20] V. K. Thakur, Cellulose-Based Graft Copolymers: Structure and Chemistry. (1981).
[21] H. Luo, G. Vaivars, and M. Mathe, “Double cross-linked polyetheretherketone proton exchange membrane for fuel cell,” Int. J. Hydrogen Energy, vol. 37, no. 7, pp. 6148–6152 (2012).

Performance Comparison of Bolt Withdrawal Capacity for Mengkulang Glulam

Nor Jihan Abd Malek
Rohana Hassan
Siti Nur Surayya Mohd Kamari
Mohd Nizam Shakimon
Faculty of Civil Engineering
Universiti Teknologi MARA

Chua Yaw Long
Mechanical Engineering Department
College of Engineering
UNITEN
Malaysia

ABSTRACT

In this study, a glulam as an engineered wood product (EWP) was produced using Mengkulang. The withdrawal capacity tests were conducted on the Mengkulang Glulam using bolts of 12 mm and 16 mm in diameter for parallel and perpendicular grain directions. The results indicated that the withdrawal capacity of 12mm diameter bolt is lower than 16 mm bolt diameter by 80.16% when the bolts are inserted parallel to the grain direction. Meanwhile, the bolt withdrawal capacity for 12 mm is also lower than 16 mm by 64.82% when the bolts are inserted perpendicular to the grain direction. Twelve (12) mm bolt diameter inserted perpendicular to the grain provided higher withdrawal capacity than those inserted parallel by about 62.82%. On the other hand, the withdrawal capacity of 16 mm diameter bolt was observed to be higher in perpendicular to grain direction when compared to parallel insertion which differs by 33.82%. Hence, it can be concluded that the higher bolt diameter provides the better withdrawal capacity. The bolt performs better when it is inserted perpendicular to the grain rather than parallel to the grain directions.

Keywords: *Timber, Glulam, EYM, Withdrawal Capacity, Grain Direction.*

ISSN 1823- 5514

Received for review: 2016-04-19
Accepted for publication: 2016-08-11
Published: 2016-12-19

Introduction

Timber is one of the oldest structure material used worldwide for construction purposes. It has gone through various improvements with the passage of time. Their main advantage, high strength to weight ratio, has provided great performance and potential for improvement. Current construction aesthetic demand has results in many new engineered wood products (EWP) introduced. Recent innovation had gave birth to numerous engineered wood products such as plywood, particle board, Oriented Strand Board (OSB), glued laminated timber (Glulam), solid structural timber, laminated beams and homogenized wood products [1].

The most critical part of a structure is the connection part. Load carrying capacity and modes of failure of the connection part can be predicted by referring to the European Yield Model (EYM). The EYM model are created based on the bending resistance of the fastener, the crushing strength of wood or member material, joint geometry, and assumed mechanical relationships. It shows a set of possible yield modes for single and double shear plane for timber-to-timber and steel-to-timber based connection. For each modes of failure, the characteristic strength is predicted from a static analysis, with assumptions that members and fasteners behave as ideal rigid-plastic materials [2].

Joint behaviour may also be affected by variable such as member thickness, width, fastener type and number of units used, spacing between fastener units, end and edge distance, moisture content of wood, preservative or fire-retardant treatment. Hence, the effect of these variables on joint strength must be known in order to compile accurate design criteria for established fastener and connector types as well as for those under development to evaluate the influence of mentioned factors [3].

The term of withdrawal resistance is to measure resistance to withdrawal load in a plane normal to the face. It was influenced by the density and internal bonding of the panel [4]. The study of withdrawal resistance of threaded fastener will be higher when the smooth shank portion or a part of it was inserted into wood. Hence forth, for conservatism purpose, this study has only inserted the threaded portion instead of including the smooth shank [5].

The aim of this study is to identify the unknowns namely withdrawal capacity, embedment strength, and yield moment which are required to calculate load-carrying capacity of Mengkulang Glulam using designed equations stated in the Eurocode 5, Section 8.2.2. Bolts with diameter of 12 mm and 16 mm are inserted parallel and perpendicular to the grain direction. The bolt withdrawal resistances were also compared with respect to their variability of bolt diameter and load to grain direction of Mengkulang Glulam.

Material and Methodology

In order to find the performance difference of withdrawal capacity across the grain and along the grain, the timber blocks were cut. The timber block specimen design was based on the associated formula with 12 mm and 16 mm bolt diameter for parallel and perpendicular as shown in Table 1. Table 2 shows minimum values of spacing, end and edge distance for bolts from Table 8.4, Clause 8.5: Bolted Connection. These sizes were calculated in accordance to EC 5:2008 specification of minimum end and edge distance as shown in Figure 1

All 40 timber specimens were marked at their centres and drilled with a drilling machine. The drill diameters were 2 mm less than the bolts' respective diameter. Drill lengths are according to the bolts' thread length, 3.9 cm for the 12 mm diameter and 4.5 cm for the 16 mm diameter. The threading was done on each sample by manually inserting the bolt into the hole without using any machine to ensure that the thread would not be damaged.

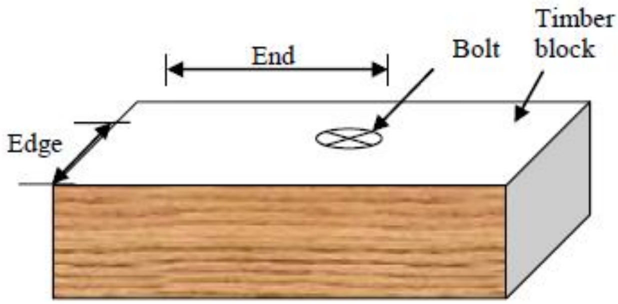

Figure 1: End and edge distance

Table 1: Timber block specimen design

	Specimen			
Grain Direction	**Parallel**		**Pependicular**	
Bolt diameter (mm)	12	16	12	16
Number of tests	10	10	10	10
Length of bolt (mm)	130	130	130	130
Timber block area (mm^2)	72 x 168	96 x 224	96 x 168	128 x 224
Timber block thickness (mm)	90	90	90	90

Table 2: Minimum values of spacing and edge and end distances for bolt EC 5:2008

Spacing and end/edge distances	Angle	Minimum spacing or distance
a_1 (parallel to grain)	$0^\circ \leq \alpha \leq 360^\circ$	$(4 + \lvert\cos \alpha\rvert)d$
a_2 (perpendicular to grain)	$0^\circ \leq \alpha \leq 360^\circ$	4d
$a_{3,l}$ (loaded end)	$-90^\circ \leq \alpha \leq 90^\circ$	max (7d; 80 mm)
$a_{3,c}$ (unloaded end)	$90^\circ \leq \alpha \leq 150^\circ$	max [(1 + 6 sin α)d; 4d]
	$150^\circ \leq \alpha \leq 210^\circ$	4d
	$210^\circ \leq \alpha \leq 270^\circ$	max [(1 + 6 sin α)d; 4d]
$a_{4,l}$ (loaded edge)	$0^\circ \leq \alpha \leq 180^\circ$	max [(2 + 2 sin α)d; 3d]
$a_{4,c}$ (unloaded edge)	$180^\circ \leq \alpha \leq 360^\circ$	3d

Table 3: Minimum distance of timber block specimens

Distance	Bolt diameters (mm)	
End and Edge x 2 sides	12 mm	16 mm
End distance, $a_{3,t}$	168 < 200	224 > 240
Edge distance, $a_{4,t}$	96 < 100	128 > 140

The materials of the experiment setup are prepared in accordance to standards related to withdrawal resistance which are EC 5:2008 [6] and ASTM D1761-12 (2012) [3]. The withdrawal resistances data were obtained from the experiment conducted in heavy structure laboratory at Faculty of Civil Engineering, Shah Alam using withdrawal resistance test setup.

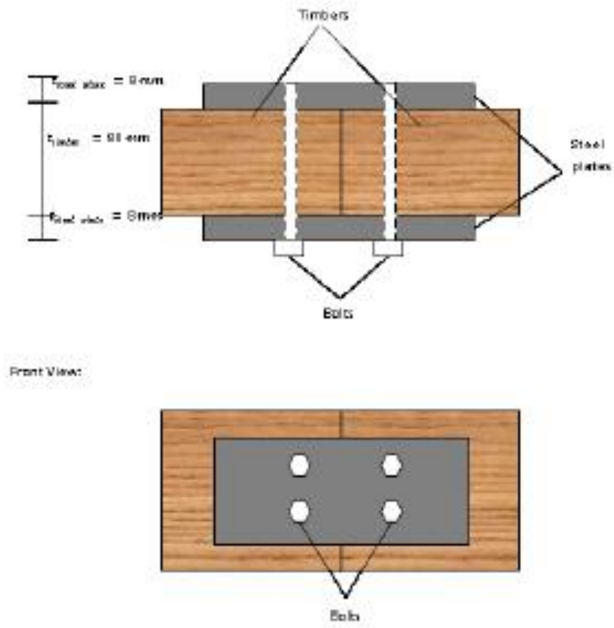

Figure 2: Timber-steel connection design

Half-threaded mild steel bolts with galvanized steel were used in this study. Bolt diameter sizes that were tested are 12 mm and 16 mm respectively. There were also two washers used in the withdrawal test, which were located under the bolt head and under the nut. According to EC 5, 10.4.3 (2), it is required that the thickness of washer used must be more than 0.3d where d is the diameter of the bolt.

Figure 2 illustrates the required design for the application of withdrawal capacity experiment sample setup. Figure 3 illustrates the final set up of the withdrawal capacity experiment. Threading length were the same with the drilling length, along the bolts thread length as shown in Figure 3.

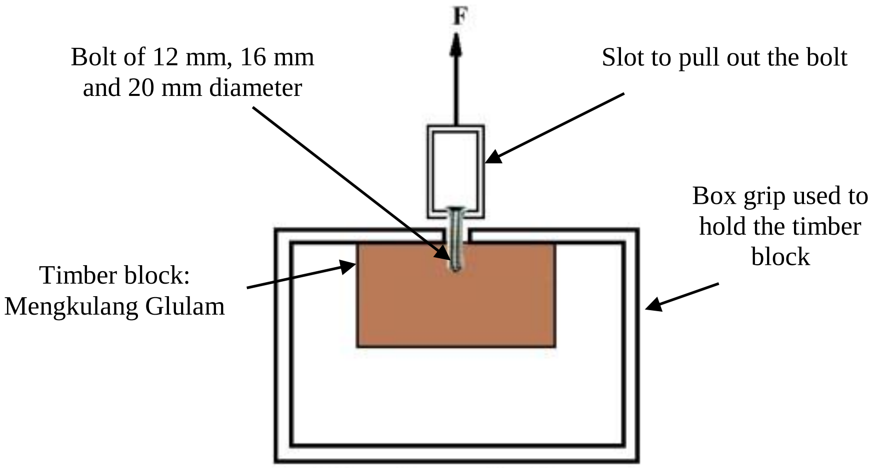

Figure 3: Withdrawal test setup

Results and Discussions

Withdrawal capacities for all the 40 samples were obtained from dividing the peak or maximum load that can be applied to every sample to withdraw the bolt from the timber block samples, with the deformation formed on the timber block samples at the exact time the peak load occurred. The pattern of how the withdrawal capacity increases with deformations was studied and analyzed.

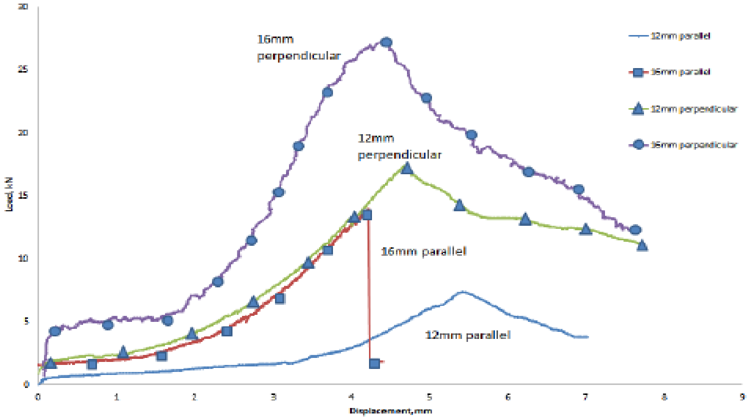

Figure 4: Relationship of bolt size diameter inserted parallel and perpendicular to the grain

Figure 4 illustrates the results obtained for all the withdrawal capacity tests parallel and perpendicular to the grain. Initial results for the 12 mm bolts with parallel insertion show that there is slight increment on every deformation formed. This is probably because of the threading done on the timber block samples hole, the grip which contributed from rope effect of the bolt threading prevented the bolt to be pulled out easily.

As the deformations of the timber block sample progresses, more loads can be applied until it reached the maximum load. For example, the maximum load recorded is 13.5 kN specifically for 16mm diameter parallel to the grain. The length of bolt thread gripped into the bolt hole became lesser, making it easier to withdraw the bolt from the timber block sample. Consequently, after the maximum load was reached, the load drop at the same rate as the way it started to rise enthusiastically before.

When the bolt is inserted perpendicular to the grain direction higher withdrawal capacity was recorded. The maximum load recorded is 7.9225 kN. This is because when the load is pulled against the grain direction, the force is acting against the surface instead of along the surface.

The changes in bolt diameter obviously changed the withdrawal capacity to a whole new level.

For parallel insertion, the withdrawal strength increases steadily across the deformations until it reaches the maximum value at 5.2431 kN for 16 mm diameter. In a short amount of time, the deformations on the timber block sample cannot resist the pulled out withdrawal load It was failed suddenly and the timber specimen broke into half with 16 mm parallel with the grain.

This indicates that bolt with higher diameter is not suitable for connection parallel to the grain as it will fail easily. This is because the bigger bolt diameter contributes to higher load and the timber cannot withstand the load and will deform steadily like the patterns observed with the smaller diameter, 12 mm bolt diameter.

This proved that the best way of fastening the bolt into timber is by penetrating perpendicular to the timber surface instead of parallel along the bolt and grain direction. Higher withdrawal capacity provides better grip of the bolt on the Mengkulang Glulam. Hence, the study proven that the best connection type should include the suitability of big size diameter bolt fastened to the timber with perpendicular to the grain direction.

Figure 5: Timber specimen with 16 mm bolt diameter broken into half

Figure 6: Sample failure observed for 16 mm perpendicular to the grain

Table 4 shows the mean withdrawal capacity results obtained for each bolt diameter with respect to different grain directions which were calculated from the maximum withdrawal capacity of each test samples conducted.

Table 4: Mean withdrawal capacity for parallel and perpendicular to grain directions.

Grain direction	**Parallel**	**Perpendicular**
Diameter of bolt (mm)	**Mean withdrawal capacity (kN/mm)**	
12	1.04	2.7868
16	5.2431	7.9225

The results were analysed with 0.05 confidence level providing the mean withdrawal capacity values as shown in the table above. The mean was calculated from withdrawal capacity values of the 10 samples of each of the bolt diameter with respective grain direction.

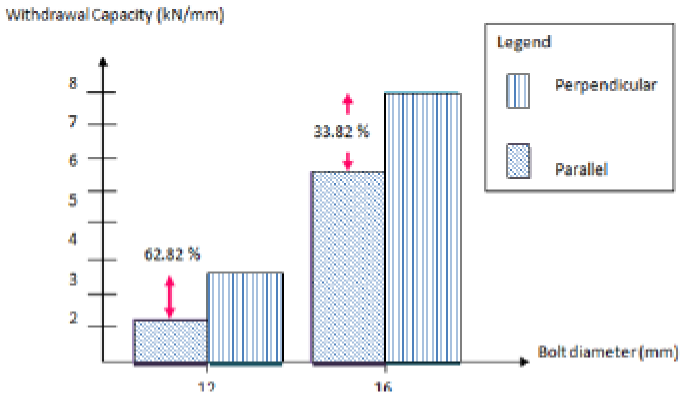

Figure 7: Percentage differences between parallel and perpendicular grain directions for 12 mm and 16 mm bolt diameter

Percentage of difference between parallel and perpendicular to the grain with the same diameter sizes are 62.82% for the 12 mm diameter bolt and 33.82% for the 16 mm diameter bolt. From the difference observed from Figure 7 the bolt withdrawal capacity differences between parallel and perpendicular to bolt has decreased as the bolt diameter increased.

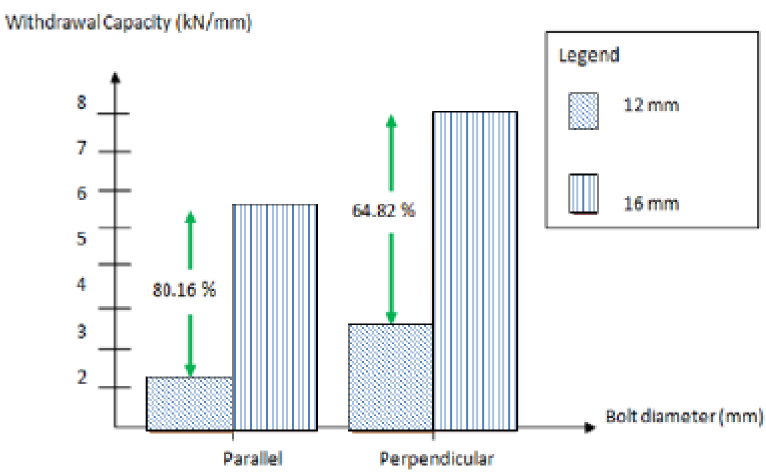

Figure 8: Percentage differences between 12 mm and 16 mm bolt diameter for parallel and perpendicular grain directions.

On the other hand, percentage of difference between two different diameters which are 12 mm and 16 mm is 80.16% for the parallel and 64.82% percentage difference when it was inserted perpendicular to the grain as shown in Figure 8. Hence, it can be observed that the percentage difference for the withdrawal capacity when the bolt is inserted perpendicular to grain direction having different bolt diameter noticeably lower than the bolt inserted parallel to the grain direction with different bolt diameters which were 12 mm and 16 mm bolt diameters.

By comparing the performance of bolt due to withdrawal capacity of the bolt, the higher the diameter of the bolt, the higher the withdrawal resistance experienced by the bolt and timber block connections. This result is in agreement with the study of Haftkhani et al. [7], who indicated that the withdrawal resistance increased significantly with increase in screw diameter for face and edge direction by 50% and 10% respectively. Factor of the size contributions has been well known to providing higher strength since ages, and this experiment has proven the fact with deep reason. The contact area of the bolt with the timber block sample increases when the diameter of bolt increases.

Thus, it provided higher withdrawal strength to pull the bolt from the timber block. In a pair wise comparison, the grain direction has proven to provide an effect on the withdrawal capacity. This is because the variation of the tissue and structure of the Mengkulang Glulam has provided variation of withdrawal capacity values. The samples with bolt inserted perpendicular to the timber block grain direction triumphed over the samples with bolt inserted parallel to the timber block grain direction, provided that the comparison was between the same bolt diameter.

However, the size contribution affects more on the withdrawal capacity than the grain direction because values obtained from 12 mm bolt diameter penetrated perpendicular to the grain was still less by 46.85% compared to 16 mm bolt diameter penetrated parallel to the grain. From the results obtained, it was intriguing fact that the ranges of the withdrawal capacity were noticeably wider when the withdrawal resistance was stronger. For an instance, ranges difference for a weakest withdrawal resistance 12 mm bolt diameter with parallel to grain was only 0.35 kN/mm meanwhile the ranges difference for a strongest withdrawal resistance 16 mm bolt diameter with perpendicular to grain was 6.47 kN/mm. This may become useful when client wants to choose the variance of withdrawal capacity ranges later.

Conclusion

The bolt withdrawal resistances of 12 mm bolt diameter inserted parallel to the grain is 1.04 kN/mm lesser than bolt diameter inserted perpendicular to the grain which is 2.7868 kN/mm. Nevertheless, the bolt withdrawal resistances of 16 mm bolt diameter inserted parallel to the grain is 5.2431 kN/mm lesser than bolt diameter inserted perpendicular to the grain is 7.9225 kN /mm. The withdrawal capacity of 16 mm bolt diameter is 80.16% bigger than 12 mm bolt diameter inserted into the timber block with parallel to grain direction. Concurrently, the withdrawal capacity of 16 mm bolt diameter is 64.82% bigger than 12 mm bolt diameter inserted into the timber block with perpendicular to the grain direction. The bolt withdrawal resistances found that for 12 mm bolt diameter inserted with parallel to grain direction is 62.82% difference with perpendicular to the grain direction. Meanwhile, the bolt withdrawal resistance for 16 mm bolt diameter inserted with parallel to grain direction is 33.82% difference with perpendicular to the grain direction.

In conclusion, the withdrawal capacity observed from the experiment conducted showing variance in terms of the manipulated factors which were bolt diameters and the grain direction of timber block samples corresponds to the direction the bolt was inserted into the timber block sample as shown in Figure 12. The biggest contribution to the higher withdrawal capacity is the size of the bolt diameter instead of the grain direction. However, bigger diameter cannot be used on the parallel grain diameter as it will cause the Mengkulang Glulam to fail abruptly, and that is exactly what should be avoided at all cost by the civil engineer designer. Thus, it is highly recommended that they do testing on the connections combinations the desired to use.

Acknowledgements

The authors would like to thank Universiti Teknologi MARA for funding the research through 600-RMI/DANA 5/3/PSI (226/2013) from Research Management Institute (RMI), UiTM.

References

[1] P. D. Marutzky, (2002). Glue-laminated timber: a high-grade, ecologically sound material with favorable disposal properties. Fraunhofer-Institut for Wood Research,Wilhelm-Klauditz-Institute, Braunschweig , 1.

[2] T. E. McLain, L. A. Soltis, D. G. Jr., & T. L. Wilkinson (2005). LRFD for Engineered Wood Structures-Connection Behavioral Equations. J. Struct. Eng. 1993.119:3024-3038 , 3024-3038.

[3] ASTM D1761-12. (2012). Standard Test Methods for Mechanical Fasteners in Wood. Washington. D. C.

[4] A. Hamid, A. Halil, A. Shakri, I. Kamal, N. Azrieda, & S. Zalifah (2012). Screw Withdrawal Resistance of Moulded Laminated Veneer Oil Palm (MLVOP) Bonded with Formaldehyde Resins. Modern Applied Science , 112-119.

[5] H.S. Baek, H. Morita, A. Shiiba, Y. Iimura, & F. Imai (2012). Influence of shape factors of wood screw on withdrawal performance. WCTE 2012 Proceedings.

[6] Eurocode 5. (2008). Design of Timber Structures (BS EN 1995-1-1-2004+A1:2008).

[7] A. R. Haftkhani, G. Ebrahimi, M. Tajvidi, & M. Layeghi (2011) "Investigation on withdrawal resistance of various screws in face and edge of wood – plastic composite panel," Mater. Des., vol. 32, no. 7, pp. 4100–4106.